Master Thesis

Measurement and Characterization of a Reconfigurable Intelligent Surface with an Automated Measurement Environment

carried out for the purpose of obtaining the degree of
Diplom-Ingenieur (Dipl.-Ing.)
submitted at TU Wien
Faculty of Electrical Engineering
by

Florian Alexander KISS
Mat.No.: 11771269

under the supervision of

Univ.Prof. Dipl.-Ing. Dr.techn. Markus Rupp
Senior Scientist Dipl.-Ing. Dr.techn. Robert Langwieser
Institute of Telecommunications

Abstract

A reconfigurable intelligent surface (RIS) is an important novel technology of the sixth generation of mobile communications (6G). It promises to extend the coverage area of a base station to previously shadowed areas through anomalous reflections. It comprises an array of RIS elements, which can adjust their reflection coefficients. This thesis uses a square RIS with 6×6 elements based on varactor diode technology. Reflecting an incident wave towards a specific direction is accomplished with a clever arrangement of its reflection coefficients, referred to as beam-focusing or beam-forming. To achieve this, knowledge of the reflection coefficients of the individual RIS elements is necessary. This thesis aims to determine these reflection coefficients based on a series of measurements performed using an automated measurement environment. The results of these measurements enable the evaluation of the performance of the RIS in terms of its magnitude and range of available phase shifts. These results are then compared to prominent RIS channel models, highlighting their differences. The data that has been acquired can be used for further research into RIS channel models and beam-focusing algorithms.

Contents

1 Introduction

The fifth generation of mobile communication (5G) [1], [2] addresses issues along three different branches: enhanced Mobile BroadBand (eMBB), massive Machine-Type Communication (mMTC) and Ultra Reliable Low Latency Communications (URLLC). These branches aim to increase data rates available to users, enable communication between smart devices without a base station in between and low latency communications with high reliability requirements for, e.g., security and medical applications, respectively. With this new technology also comes a push towards higher frequencies from sub-6 GHz bands to millimeter wavelengths enabling higher bandwidths and therefore higher data-rates. However, as with previous mobile communications generations, with the adoption of this technology, an increase in energy consumption is expected [3], [4]. An expansion of processing capabilities is required as well as a larger number of base stations due to the higher attenuation at millimeter wave frequency bands. This trend of steadily increasing energy consumption from the telecommunications sector is expected to continue for the sixth generation (6G) as well [5], [6]. Proposals and projects already exist in the frame of 5G to reduce the energy consumption of basestations [7] by, e.g., shutting them off when they are underutilized. With 6G however, cell-free massive multiple-input multiple-output communications [8], [9] is a prominent aspect, again increasing the number of base stations. However, this technology aims to bring the base stations closer to the user and therefore, decrease the path loss between user and base station. Ultimately, this allows base stations to use lower transmit powers, and with the path loss increasing with the squared distance, large reductions in energy consumption are expected [10]. But this is not the only technology aimed at counteracting the steady increase in power consumption, another technology and the focus of this work is the Reconfigurable Intelligent Surface (RIS) [11]–[17]. Many different implementations and designs of RIS already exist, including, but not limited to, passive or active designs based on MosFETs [12], PIN-Diodes [13], Varactor Diodes [14], [15], liquid crystals [16]. One greatly discussed use case of this device is the extension of the coverage areas of base stations, by placing these surfaces in locations, where their anomalous reflection characteristics may be used to improve the wireless channel. Specifically, the Signal to Noise Ratio (SNR) of the user that is located in a shadowed region (area that is somehow blocked, by hills or buildings, and experiences greater path loss), may be improved by the addition of a RIS capable of focusing the incident wave from the basestation towards the user's location.

Additionally, a RIS allows the operator of the cell to shape parts of the wireless channel by reconfiguring the phase shifts at the individual array elements [18], [19]. The configurable phase shifts of the RIS elements can also be used to manipulate a poorly conditioned channel matrix, improving the multipath diversity [20].

However, to achieve these improvements, the phase shifts the RIS is capable of, must first be known. In many cases, this is done via simulation. The computed phase shifts are then, for example, used in beam-focusing measurements, improving the SNR and data-rate of a user. Nevertheless, this method still requires some knowledge of the behavior of the RIS itself. The algorithms used for such schemes typically make some model assumptions [21], [22] that, while reasonable from a simulation perspective, may ignore some other previously unknown or unfavorable parasitic effects of the RIS.

The goal of this thesis is therefore to measure a RIS and characterize its behavior. Specifically, the determination of the phase shifts and magnitudes of the reflections from the RIS in relation to the controlling parameters available for the RIS used in this re-

search. The information acquired in this manner can subsequently be used to improve our understanding of the performance of a RIS. An additional point of interest is its influence on measurements taken in the nearfield. Especially at millimeter wavelengths, the farfield distances [23, Chapter 14.1] can become prohibitively large, making measurements in the farfield difficult, due to the measurement environments necessarily also having to increase in size. The question that will be investigated, is whether it makes a difference if the RIS is characterized with nearfield and farfield distances or with only farfield distances.

This work is split into three chapters. First, in Section 2 the measurement environment is discussed. Its construction as well as the control algorithms are explained. Some important design parameters that were considered for this measurement environment are presented as well. In the next chapter, Section 3, the measurements acquired using this environment are investigated. The channel model employed for the processing of the data is explained in detail along with the measurements. Later in this chapter, the case of nearfield and farfield measurements is highlighted and analyzed. These results are compared against the case of farfield measurements. Towards the end of this chapter, using the information acquired up to this point, parameters are featured, capable of describing the performance of the RIS used in this research. These parameters are also used to compare the performance of the RIS with some prominent channel models in use with RISs.

Finally, this master thesis is concluded with a summary and discussion of the results in Section 4, obtained from the prior analysis.

2 RIS Measurement Environment

In this chapter the architecture of the measurement environment will be discussed. First, the mechanical setup will be presented. The components included in the measurement environment as well as its coordinate system will be shown. Then we will analyze the parameters defining this measurement environment and highlight two important questions:

- At what distance should we measure?
- What is the maximum power we can expect at the minimum measurement distance?

Finally, the controlling interface of the measurement environment is discussed, focusing on its functionality, the control of the RIS and the format used for data storage.

2.1 Construction

The measurement environment shown in Fig. 1 uses two linear and two rotational axes. The antennas are mounted on the rotating platforms, which are in turn mounted on a 3 m long linear axis (x-axis). This linear axis is a special design enabling the independent movement of the two antennas as long as they do not intersect. The RIS [14] is mounted on a scaffold on the second linear axis (y-axis). The left antenna mount will be referred to as "carriage 1" and the antenna mount on the right as "carriage 2". The antennas are connected to a vector network analyzer (VNA) using coaxial cables. To prevent the phase of the coaxial cables to change and influence the results of a measurement campaign, a special coaxial cable, whose phase remains stable during movements, is used in conjunction with a more common version. The regular coaxial cable is mounted in a manner that prevents movement and its contribution to the measured waves therefore remains fixed. This construction is used for both probe antennas.

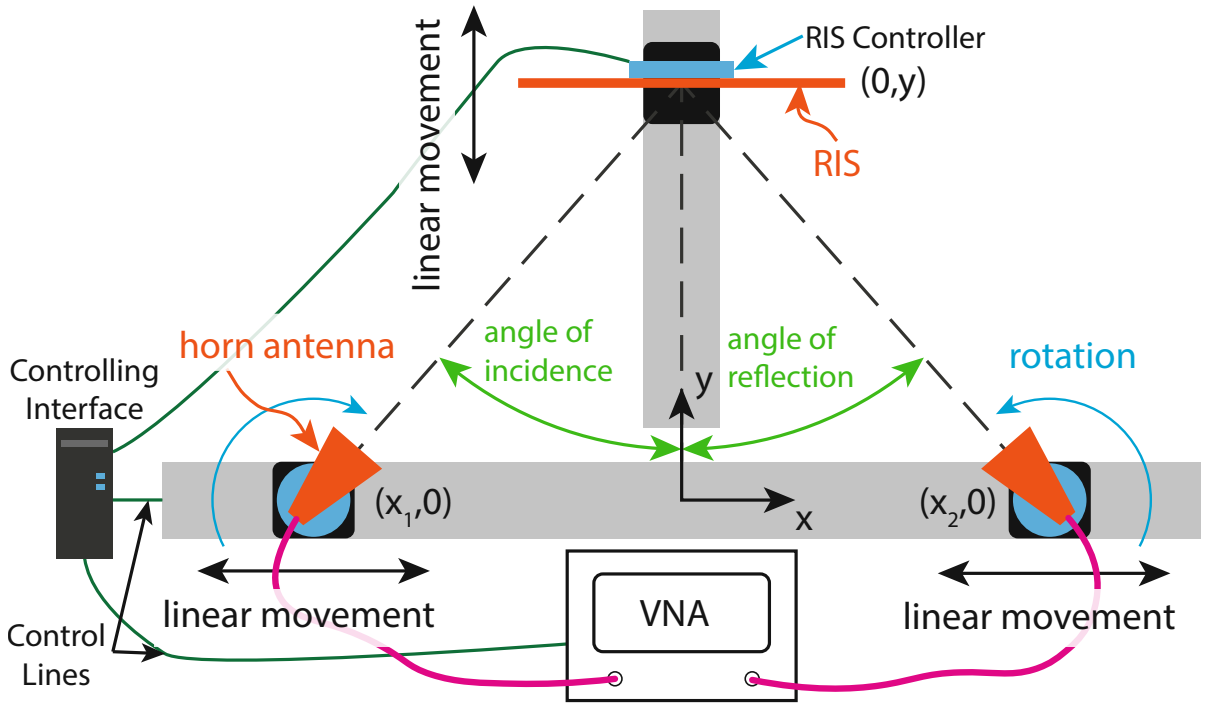

Figure 1: Schematic of the measurement environment.

Figure 2: VT70HA18+SK horn antenna mount. Assembly view and contruction.

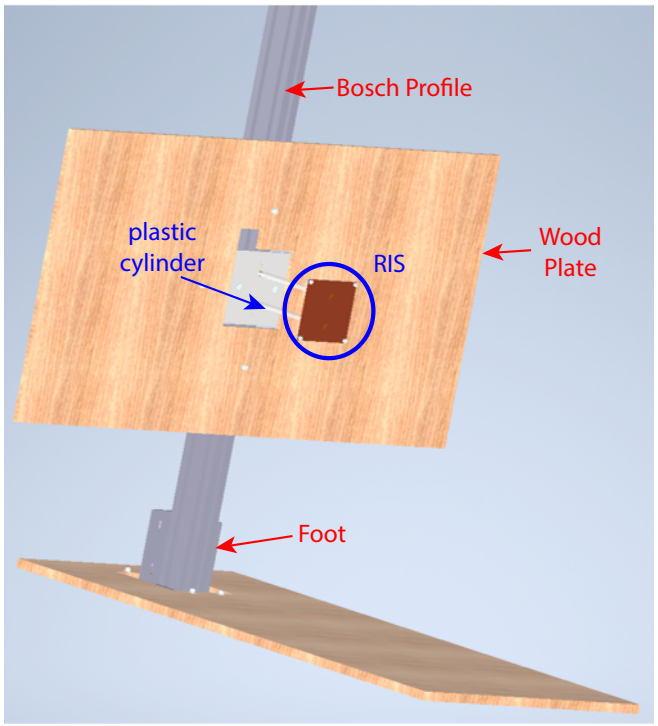

Figure 3: Assembly of the RIS mounting structure.

The antenna mounts are shown in Fig. 2. The left image displays the schematic of the antenna mount, showing a base plate connecting to the rotation axis, an angle connecting the base plate to the antenna and the antenna itself. The right image shows the final construction of this assembly. This antenna has a gain of 18 dBi with a half-power beamwidth of 20°. These parameters make measurements at larger distances possible and reduces the contribution to the received signal from the scattering environment.

The mounting structure for the RIS shown in Fig. 3 and Fig. 4 was constructed with aluminium Bosch [24] profiles, wooden plates to support the radio-frequency (RF) pyramid absorbers and a compatible foot mounted to an adapter plate, connecting to the y-axis. The RIS, attached to a plastic plate, is suspended in front of this structure by two plastic cylinders. The plate is of the same size as the RIS (125 mm × 135 mm) and therefore unlikely to affect the reflection of the RIS. The construction is modular and can support different RIS designs and sizes by replacing or adapting the plastic plate. Fig. 4 pictures the constructed RIS mounting structure, including the pyramid RF absorbing

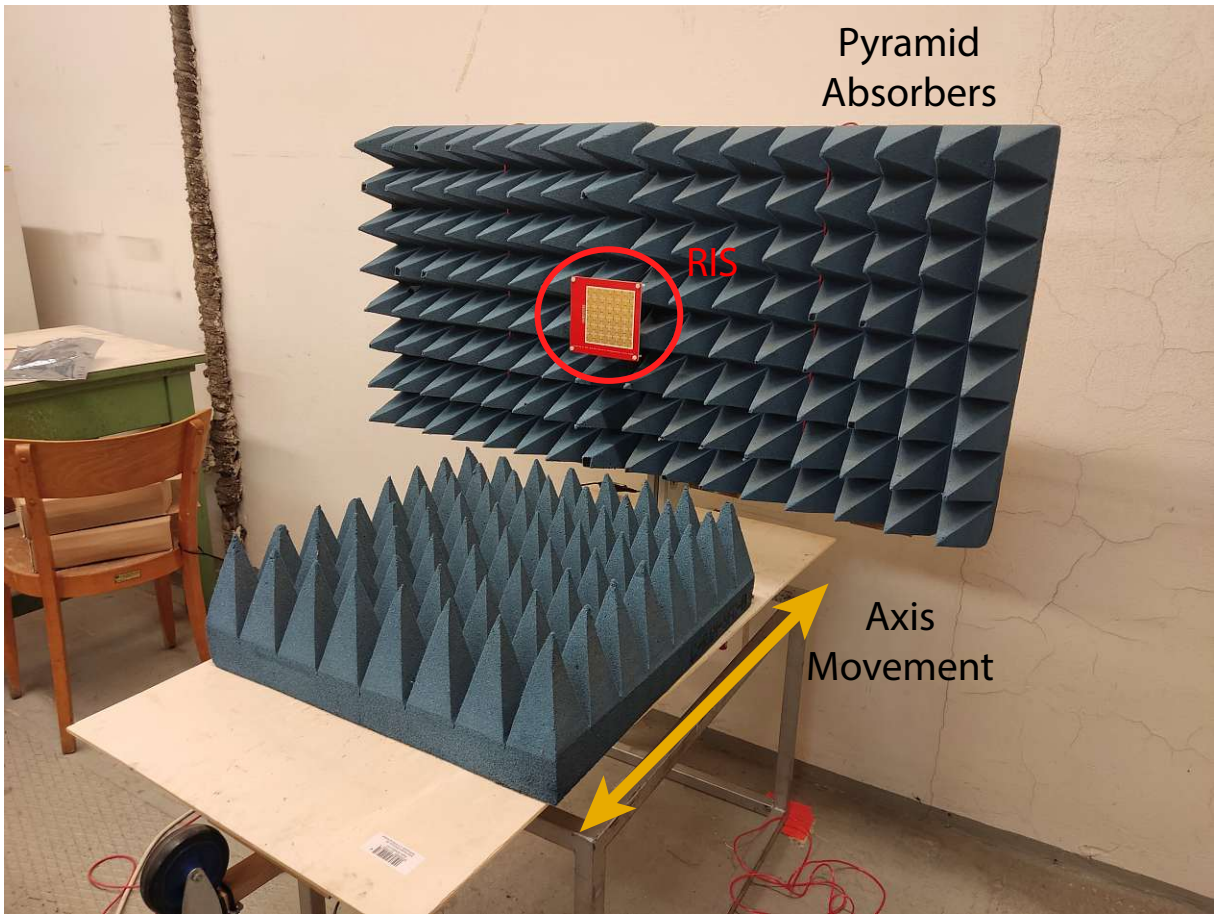

Figure 4: RIS mounting structure with pyramid RF absorbing elements, mounted on a linear axis.

elements and the RIS. The yellow arrows indicate the movement direction of the RIS. In Fig. 5 the RIS controller is shown. It is mounted to the back of the mounting structure shown in Fig. 4, behind the RIS. It consists of a 16-bit digital-to-analog converter (DAC) (*DAC81416EVM*) connected to a micro-controller (*MSP-EXP430FR5969*) and the RIS. The micro-controller in turn is connected to the controlling interface. The specific details of the communication with the controlling interface and functionality of the RIS controller will be discussed in Section 2.3.3.

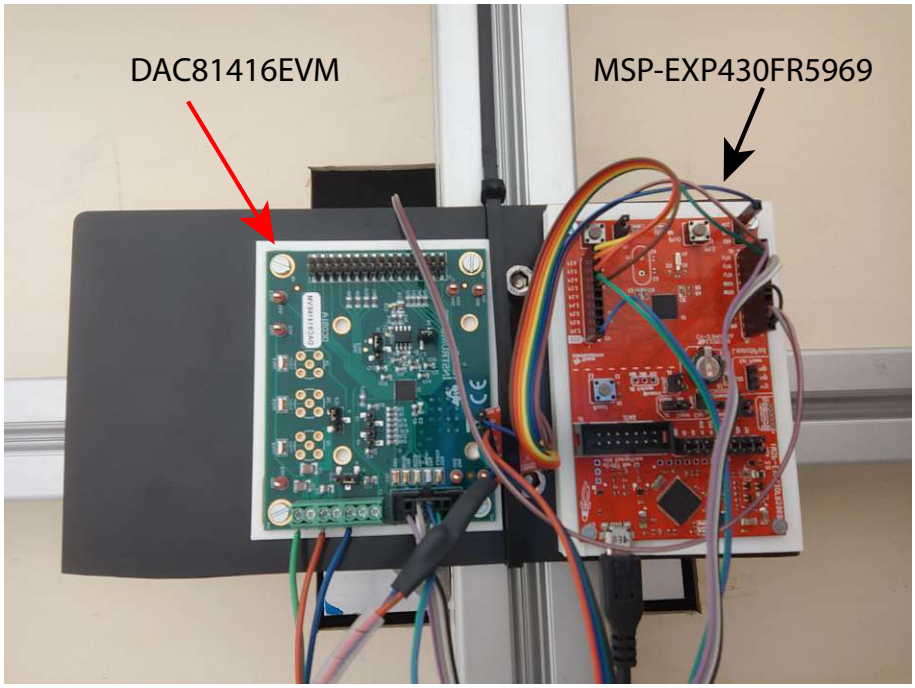

Figure 5: RIS controller mounted on the back of the mounting structure.

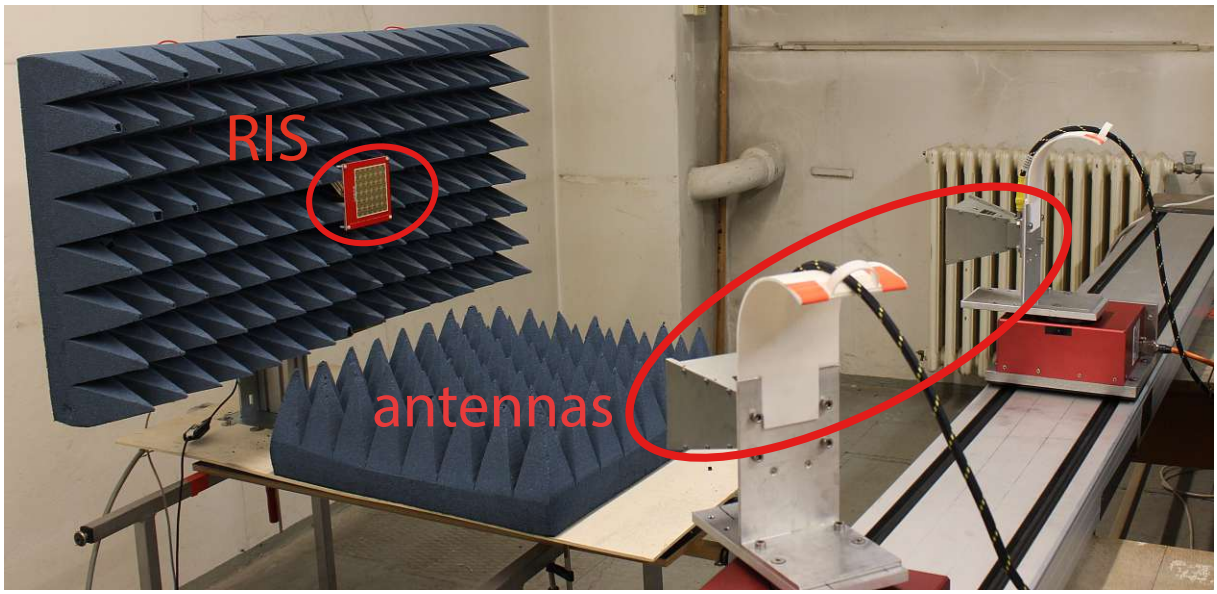

Figure 6: Picture of the mechanical part of measurement environment.

Fig. 6 pictures the mechanical portion of the measurement environment. This includes the horizontal and vertical linear axes and the rotation axes of the antennas. The vertical axis is covered by the mounting structure of the RIS, previously shown in Fig. 4. The rotation axes (in red) are located underneath the antennas and are in turn mounted to the horizontal axis. The two horn antennas can move independently from each other along the horizontal axis, but not past each other. The horn antennas pictured in Fig. 6 are also supported by this measurement environment but were not used for the following measurement and are of no further importance.

In Fig. 7 the coordinate system used in the control software is shown. The coordinate x_1 refers to the position of the rotation axis of carriage 1 on the horizontal axis in relation to the center point (origin) and should always be less than zero, x_2 is analogous to x_1 and should always be greater than zero. The coordinate y refers to the position of the RIS on the y-axis relative to the origin. The rotations of the two antennas are determined from the angles of incidence and reflection denoted as AOI and AOR respectively. These five coordinates are necessary to perform any movement operation.

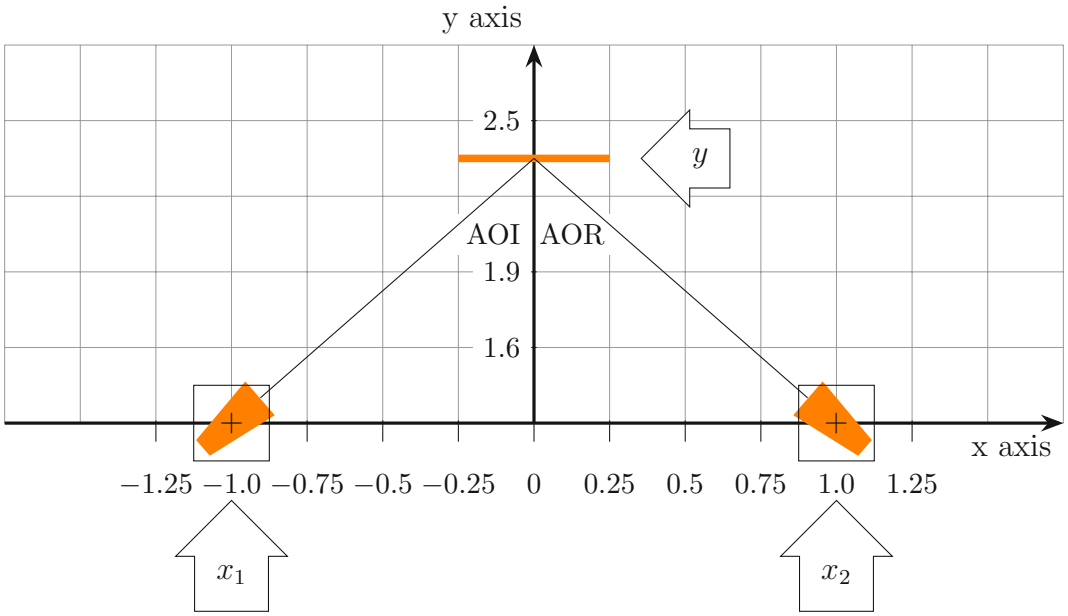

Figure 7: RIS measurement environment coordinate system.

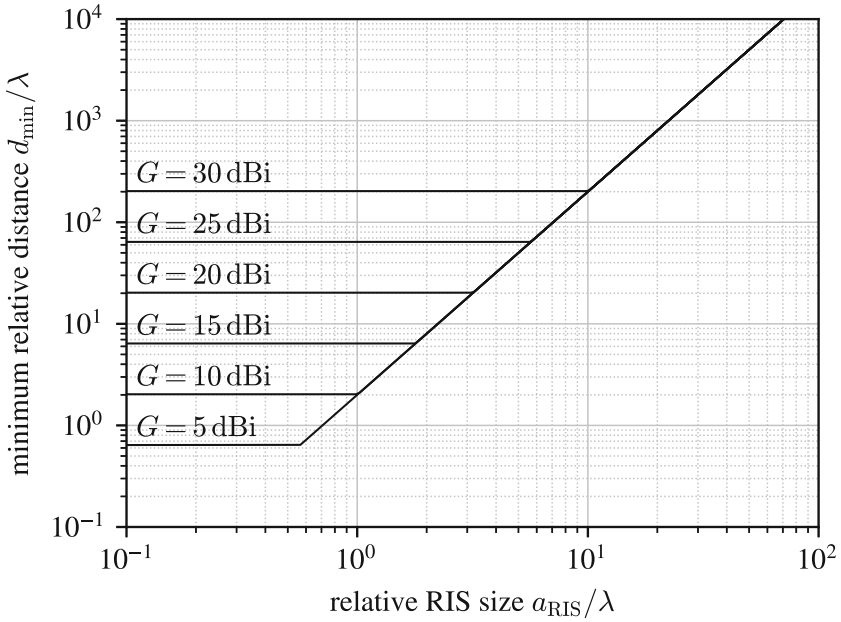

Figure 8: Minimum required distance d_{min} for the RIS and a circular aperture probe antenna for both to be in the farfield of each other. This figure was originally plotted in Fig. 1 of [25].

2.2 Design Parameters

The full characterization of the RIS requires measurements of the radiation pattern of the RIS. This radiation pattern however, depends on the angle of the incident wave, the bias voltages applied to the RIS elements (or some equivalent RIS setting parameter) and the frequency. Due to this large number of measurement parameters, it is advantageous to instead consider only a subset of measurements and compare the results with RIS models.

Two questions in particular were considered during the design phase of this measurement setup. At which distance should the RIS should be measured? This question mainly revolves around the decision of whether to measure in the nearfield or the farfield. And what is the maximum fractional received power for this measurement distance? These questions have been studied in [25] and the conclusions will be repeated here.

Firstly, regarding the question of the measurement distance, a nearfield-farfield transformation of measurement results acquired in the nearfield would only be valid for one incident angle and RIS setting. Additionally, a large amount of positions of the receive antenna would be required. Measurements should therefore be done in the farfield.

The minimum measurement (or farfield) distance d_{min} was determined in [25] as

$$d_{min} = \max\left\{d_{Ant}, d_{RIS}\right\}, \tag{1}$$

where d_{Ant} is the farfield distance of the probe antenna (only a symmetric setup is considered, i.e., transmit antenna is the same as the receive antenna) and d_{RIS} is the farfield distance of the RIS. The relative minimum distance d_{min}/λ, with λ being the wavelength, is plotted in Fig. 8 in relation to the relative RIS size a_{RIS}/λ for the simple case of a circular RIS and horn antennas with a circular aperture.

The horizontal black lines in Fig. 8 represent different horn antenna sizes indicated by their antenna gains G. The linear slope in this double logarithmic plot depicts the

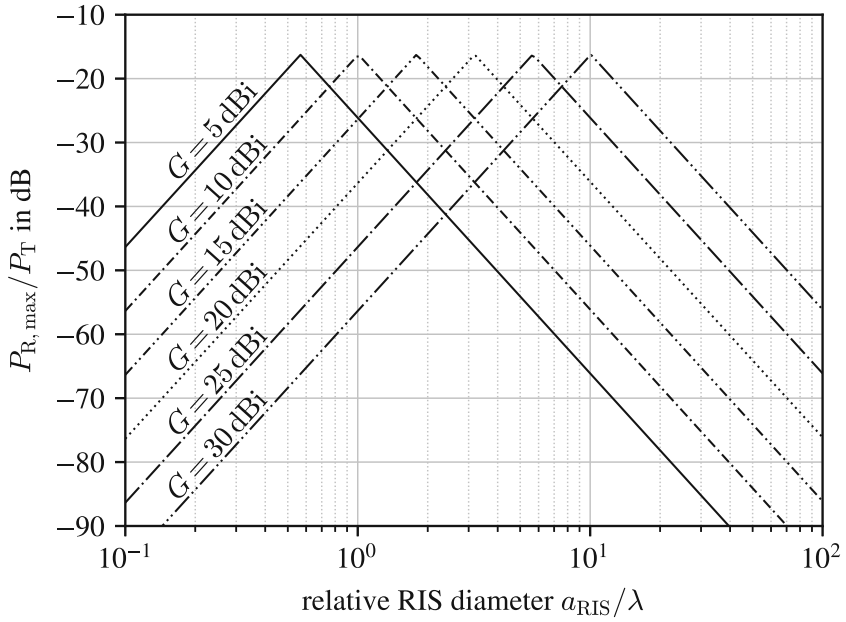

Figure 9: Maximum fraction of received power and transmitted power over a channel with a single RIS-assisted reflection. This figure was originally plotted in Fig. 2 of [25].

minimum distance due to the size of the RIS. The farfield boundary and minimum distance is indicated by the solid black lines. We can now separate Fig. 8 into two regions, one above the black lines and one below. Any point below the black lines indicates that the measurement is taking place in the nearfield of at least one of the two components (RIS, probe antenna). Any point above the black lines describes a measurement position in the farfield.

Next, we consider the second question of how much fractional receive power we can expect. Using the minimum distance d_{min}, the maximum fractional receive power $P_{R,max}/P_T$ was determined in [25] under ideal RIS reflection assumptions and is shown again in Fig. 9. In this figure we see again a series of lines corresponding to different circular horn antennas, denoted by their antenna gains. The lines rising with increasing a_{RIS}/λ are a result of the minimum distance remaining constant but a_{RIS}/λ increasing. The antenna aperture determines the minimum distance on this side. On the right side of the peak, we see the fractional receive power falling with increasing a_{RIS}/λ. The RIS diameter now determines the received power. Of special note here is the peak, it's at approximately the same value of the fractional receive power and occurs when the minimum distances of the antenna and RIS are equal. While this is an important parameter for designing a measurement setup like this, we must keep the mutual coupling between antennas in mind. For a RIS with fixed size, it makes sense to use antennas with larger gain, with larger farfield distances, that avoid introducing a direct path between transmit and receive antenna due to their respective beamwidths. With higher antenna gain, we can generally expect a tighter main beam of the radiation pattern of the antenna. If there are no sidelobes, secondary beams with lower gain, aimed at each other, we can also expect good isolation of the probe antennas.

2.3 Controlling Interface

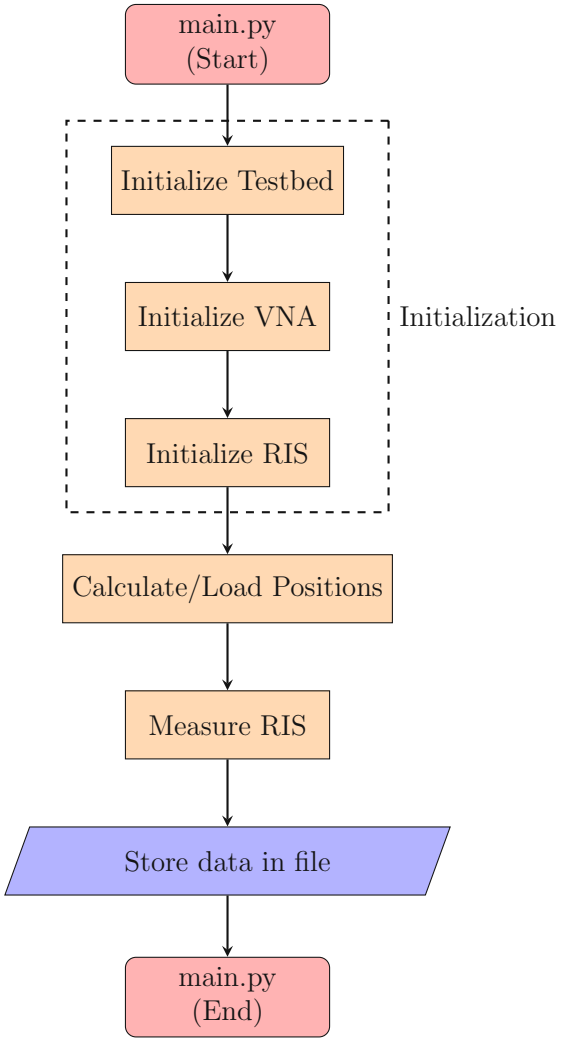

Figure 10: Flowchart of the testbed setup control algorithm.

The controlling interface is a python program executed on a computer located near the measurement environment. It controls the measurement device (vector network analyzer), the mechanical part (linear and rotation axes) and communicates with the RIS controller. The RIS controller translates the parameters received from the controlling interface into the appropriate bias voltages to be applied to the individual elements of the RIS. Details on its functionality will be explained in Section 2.3.3. Fig. 10 shows an overview of the functionality of the control algorithm. It is separated into an initialization phase, the preparation of the moving axes, the measurement itself and finally the storage of the acquired data. The initialization will be discussed in Section 2.3.1, the measurement procedure as well as some examples for possible movement patterns will be considered in Section 2.3.2 and finally the data storage and its format will be presented in Section 2.3.4.

2.3.1 Initialization

In Fig. 10 a flowchart of the measurement routine is shown. The initialization can be separated into three steps, the testbed, VNA and RIS. The testbed initialization occurs first, with either the default parameters representing the construction described above or custom parameters may be chosen, should some components have been replaced or disabled for the planned measurement campaign. These parameters are necessary to transform the coordinate system described in Fig. 7 in such a way, that the controlling interface can direct the moving components to their intended locations and orientations. The movements of each axis, during a measurement campaign, can also be disabled separately. This feature supports the debugging and error detection of hardware faults, or testing of measurement equipment. During the initialization of the VNA an ethernet connection is established and the parameters defining the center frequency, bandwidth, frequency step size, etc. are transmitted. The initialization of the RIS is equally straightforward, a serial connection is established and a status check of the RIS controller is performed. The phase shifts chosen for the measurement will be transmitted and applied later, shortly before a measurement is taken.

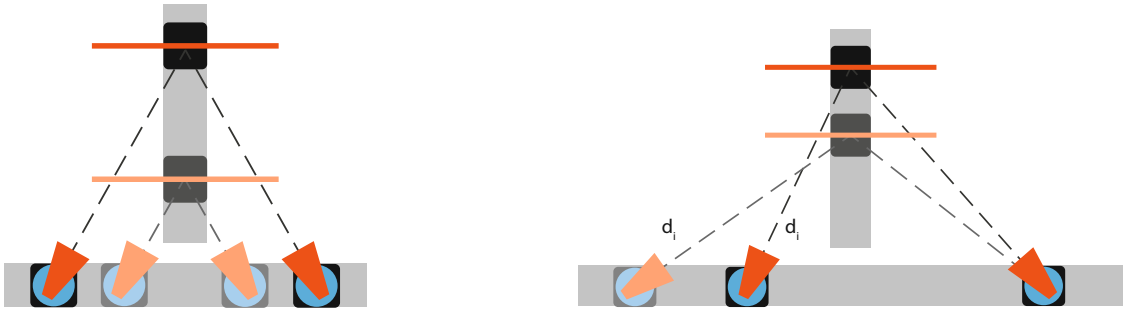

(a) Movement pattern of constant angles with AOI = AOR.

(b) Movement Pattern of Constant Incidence Distance d_i.

Figure 11: Example movement patterns of the RIS testbed.

2.3.2 Measurement Process

After the initialization is completed, the positions and angles of all axes are determined according to the chosen movement pattern. Some examples are the pattern of constant angles depicted in Fig. 11a, constant RIS position and constant incident distance. As already indicated by their names, each has a specific restriction defining the positions generated by their respective algorithms. E.g., constant angles was used to generate the movement positions used during the measurement scenarios presented in a later section. It enforces a specific angle of incidence and reflection at the RIS while increasing the y-coordinate by adjusting the x-coordinates of the antenna carriages accordingly, i.e., only the total path length from transmit antenna to RIS to receive antenna increases, the angles remain constant. Another movement pattern worth mentioning is the constant incidence algorithm sketched in Fig. 11b. While it was not used during the measurement campaigns described later, similar to the pattern of constant angles, it too aims to reduce the number of variables. Its goal is to keep the distance from the transmit antenna to the RIS constant while iterating over all possible positions, this includes all possible angles of incidence and reflection.

Now that the individual positions are known, they are passed to the measurement function (*Measure RIS*), described by the flowchart in Fig. 12. The measurements will occur once the target position has been reached and movement will resume once the measurement has been completed. No measurement is performed during the repositioning of the axes. The flowchart also has forks, deciding whether a specific component should be simulated and if the movement of the system should be plotted in an external window. This feature can be used for planning a measurement campaign, or for debugging specific measurement steps or equipment. The VNA when simulated, produces random datapoints. Otherwise, it measures the reflection at the interfaces between the coaxial cables and the antennas as S_{11} for antenna 1 mounted on carriage 1 and S_{22} for antenna 2, as well as the transfer functions at the interfaces between the two antennas S_{21} and S_{12}, i.e., from antenna 1 to antenna 2 and vice versa. That means, that the antennas are included in the measured channel, and the cables will not influence the measurement result, as they have been removed during the calibration of the VNA. This calibration step is done manually and before the measurement procedure described in Fig. 10 is started.

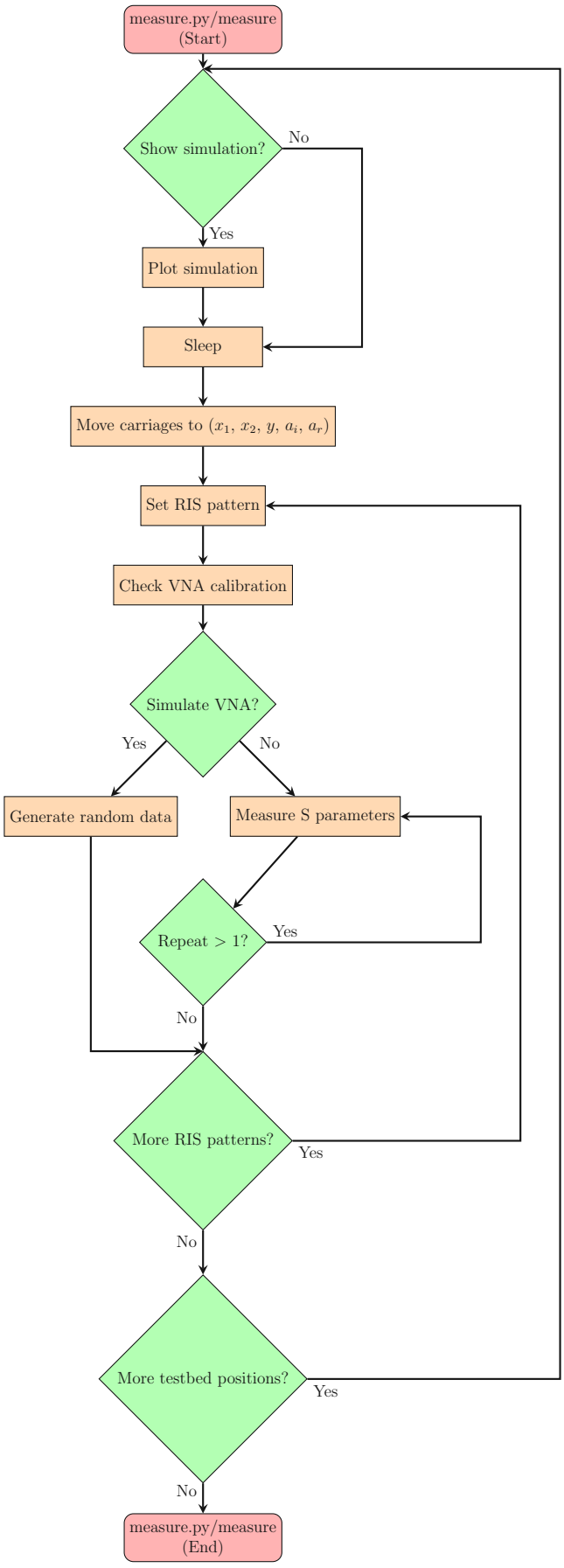

Figure 12: Flowchart of the measurement algorithm.

2.3.3 RIS Controller

The RIS design shown in Fig. 13 is based on varactor diodes. These diodes are voltage biased on a range of 0 V to 10 V and therefore only need a voltage source capable of operating in this range. It should also be controlled remotely, to enable fast switching between different RIS settings. A bachelor thesis by Markus Kerbler implemented such a device. It consists of the digital-to-analog converter (DAC) *DAC81416EVM* and the evaluation board *MSP-EXP430FR5969*, enabling a 16-bit resolution in the operating voltage range. The setup of the RIS controller is sketched in Fig. 14. The controlling interface (the computer) connects to the MSP over a universal serial bus (USB) connection. The MSP is connected to the DAC with the serial peripheral interface (SPI). This protocol supports future extensions for different and larger RIS with its daisy-chain operating mode. The controller supports the setup of a pattern of phase shifts to the RIS, by applying the corresponding voltages to the control groups.

The RIS is designed as a 6×6 unit cell array, which are collected into groups of four cells, totaling 9 independently controllable groups of RIS elements. This construction is further illuminated in Fig. 13, with a unit celled highlighted with a black square border and one of the control groups highlighted with a white square border. This figure also shows the schematic for a single unit cell, with the varactor diodes located between a triangular section of the patch and the ground line surrounding the patches. The bias voltage is applied to the triangular sections by a via connecting from the second layer. This second layer also connects to the ground lines on the top layer and is therefore a ground plane "damaged" by the voltage control lines.

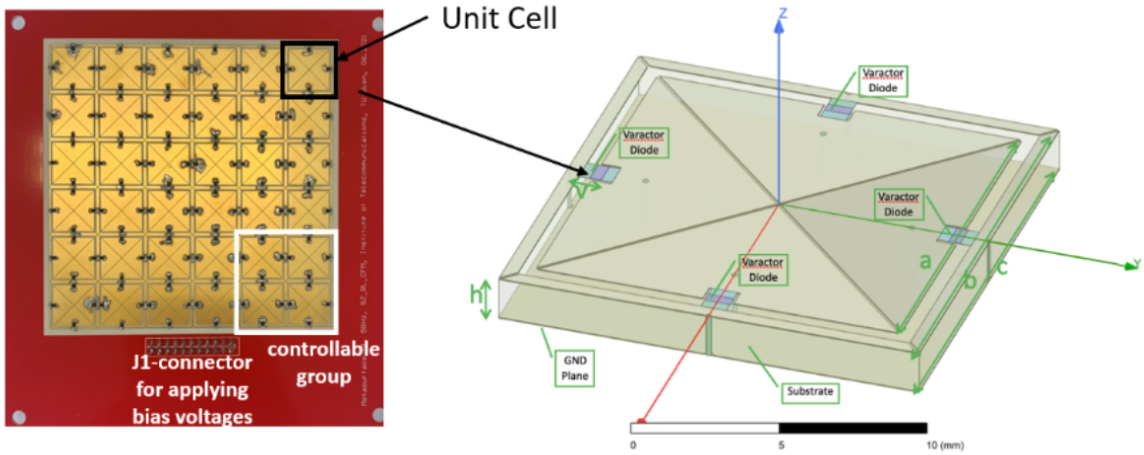

Figure 13: RIS unit cell and element grouping.

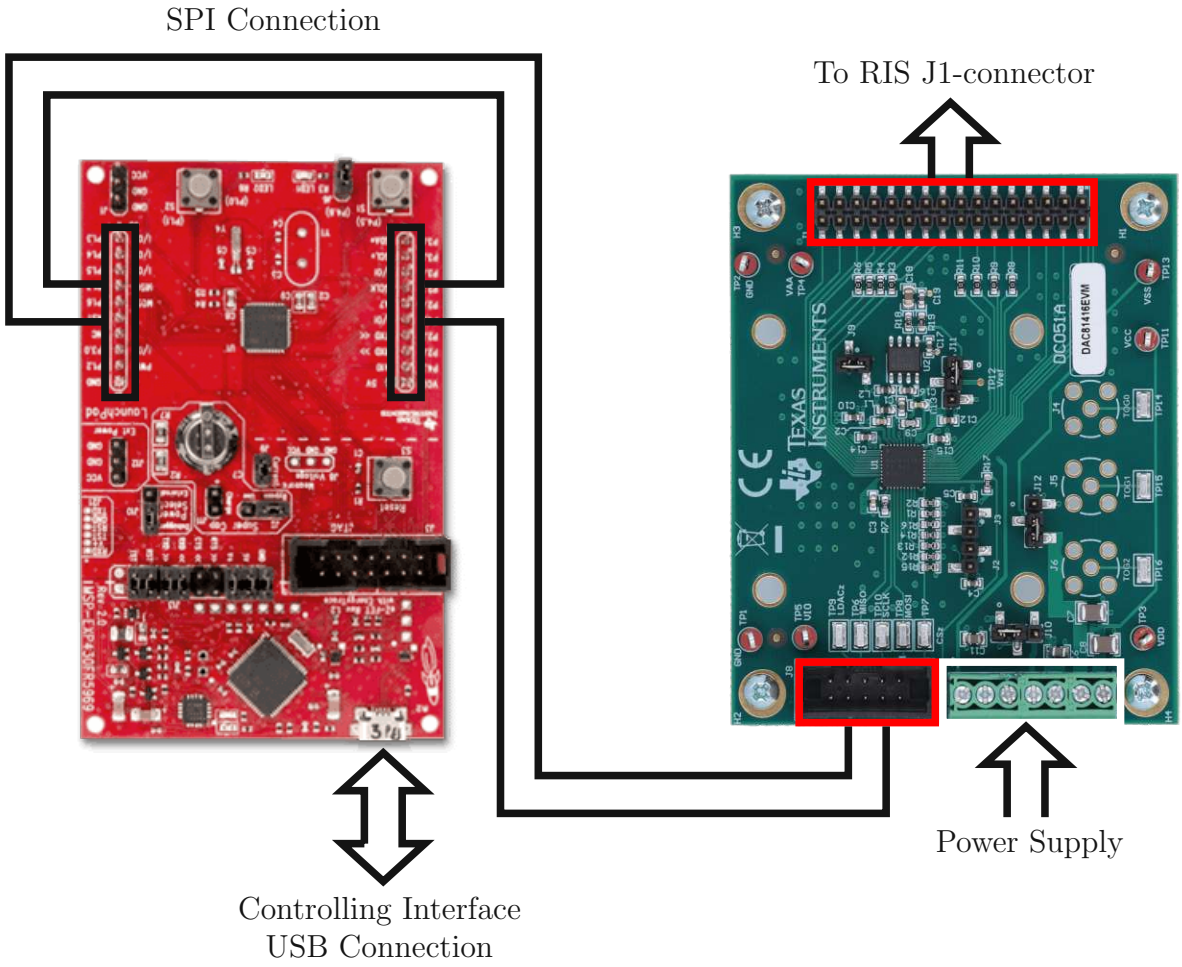

Figure 14: Sketch of the RIS Controller Setup and Connections

2.3.4 Data Storage

As there are many variables during any measurement campaign, e.g., the angles and distances of the antennas to the RIS, the current RIS setting, the frequency band; it is imperative to implement a data structure that can cover the current requirements and also adapt to potential future extensions. For this purpose, a 5-dimensional array will be used. Any specific datapoint can then be retrieved with the corresponding 5-tuple index denoted with (P, R, S, F, T), with

- P ... position index of all movable components (linear and rotational exes),
- R ... RIS parameter index, denoting the length 9 array of bias voltages applied to the control groups,
- S ... scattering parameter index with the mapping:

Python index	MatLab index	Description
0	1	S_{11}
1	2	S_{12}
2	3	S_{21}
3	4	S_{22}

Table 1: Scattering parameter index mapping.

- F ... frequency index of the measurement,
- T ... repetition number of the measurement.

Each of these individual indices connects to a secondary array, describing the specific setting. P describes the position of all movable components in translation and rotation arrays for the linear and rotational axes respectively. The values are stored in Meters and Degrees. F relates to the array of frequencies that were measured in Hertz, i.e., it informs the user of the start- and stop-frequencies, the center-frequency and bandwidth as well as the step-size between frequencies. T is not related to any other array, it denotes the repetition number of the measurement described by the parameters of the preceding indices, i.e., how often a specific measurement was taken.

The data can be stored in a compressed *numpy* [26] file format: *.npz* or in a MatLab [27] readable file format: *.mat*.

3 Phenomenological Characterization of a RIS

In this chapter, the measurement campaigns and their results are discussed. First, the parameters defining the measurements are presented and explained. Some initial channel measurements are shown as well. Next, the channel model used for processing the acquired data is discussed. The individual components are analyzed and their influence on the results will be explained. The characterization of the RIS first occurs exclusively in the farfield, but later also includes the nearfield. Afterwards, some key parameters characterizing the performance of the RIS are introduced and analyzed with an example use case. Finally, the results presented up to that point will be compared to some prominent channel models and the differences will be emphasized.

3.1 Measurement Setup

The measurement data and model that will be discussed in this section are based on three separate measurement campaigns that were executed using the measurement environment described previously. The parameters defined for each campaign are listed in Table 2. In the following subsection, the data from campaign A will be used to characterize the behavior of the RIS. Campaign B provides the data necessary to describe the noise of the environment as well as give a rough overview of the influence of the multipath environment. Campaign C aims to provide a reference measurement to compare the data acquired in campaign A against. The position pattern for a specular reflection at 15° was used, i.e., the angle of incidence (AOI) and angle of reflection (AOR) are the same at each position step. The positions then only change the path length of the system, i.e., the distance between the transmit antenna and RIS plus the distance between the RIS and receive antenna. The aim of this scheme is to keep the effect of the RIS constant, as it is assumed, that the reflection contribution from the RIS does not change when the AOI and AOR remain constant. The transfer functions resulting from the measured channel are presented in Fig. 15 and Fig. 16 at the frequencies 5.4 GHz and 5.65 GHz, respectively. The channel transfer function is denoted as $h^{(k)}_{M,l}(j\omega)$ with index l describing the position of the measurement components (the location and angles of the horn antennas, and the RIS), k representing the applied RIS setting and ω as the angular frequency. $h^{(k)}_{M,l}(j\omega)$ describes the channel between the transmit antenna mounted on carriage 1 and the receive antenna mounted on carriage 2. It is calculated as an ensemble average of the repeated measurements from measurement campaign A. An in-depth analysis of the noise and scattering in the measured data will be given in the next section.

Let us now continue with the analysis of the results shown in Fig. 15 and Fig. 16. The spirals indicated by the bold, black, continuous lines result from stepping through the homogeneous bias voltages, applied to the varactor diodes, i.e., the reconfigurable impedances. The spiral averages, i.e., the averages over k of $h^{(k)}_{M,l}(j\omega)$ at each position l are marked with red crosses. The mean value of the spiral at the first position (with smallest path length) is marked by a red diamond instead and is located in the top left corner of Fig. 15 and the bottom right corner of Fig. 16. Due to the increasing distance, with increasing path loss, a large scale spiral pattern is visible in Fig. 15. However, at some position further along, the measurement appears to deviate from this larger spiral. This is likely due to other multipath contributions becoming more prominent at the receiver at these larger distances. Also visible, is that the spirals rotate at some distance from the origin and are not centered on the origin, as the prevalent theory from [21] indicates. This

	Campaign A	Campaign B	Campaign C
Center Frequency	5.5 GHz		
Bandwidth	1 GHz		
Frequency Step Size	1 MHz		
Position Pattern	Specular Reflection with AOI 15°		
Min./Max. Path Length	3.58 m/5.134 m		
Number of Positions	31		152
RIS Setting	homogeneous: 0 V…10 V stepsize: 0.01 V	homogeneous: 0 V	
Repetitions	10	100	10
Reflecting Element	RIS		copper PCB

Table 2: Measurement campaign parameters.

same offset is also visible in Fig. 16. The large scale position pattern displays a sharp corner at some large position index l at 5.65 GHz. This could be explained by the effects due to the multipath components being even more prominent at this frequency compared to the case with 5.4 GHz.

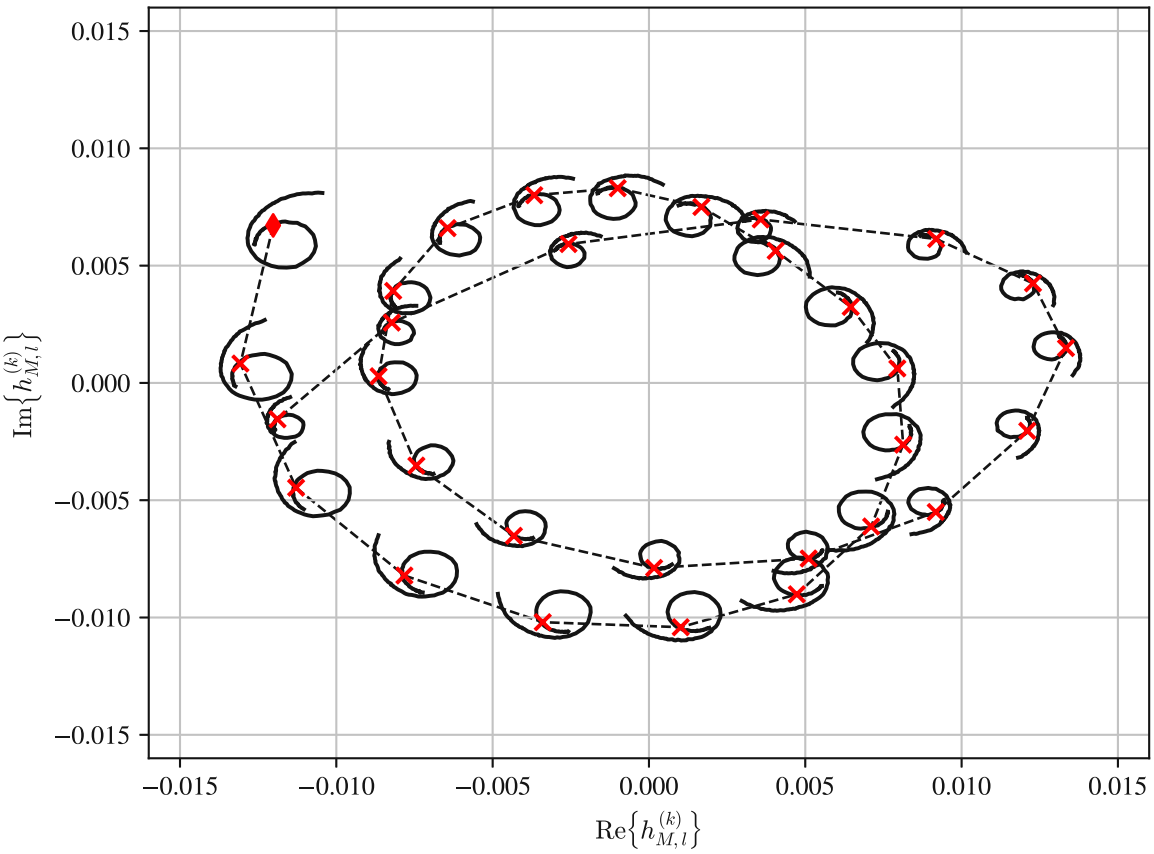

Figure 15: Results of the channel measurement at 5.4 GHz of measurement campaign A averaged over the 10 repetitions, i.e., the measurement is repeated 10 times for each position index l and RIS setting k.

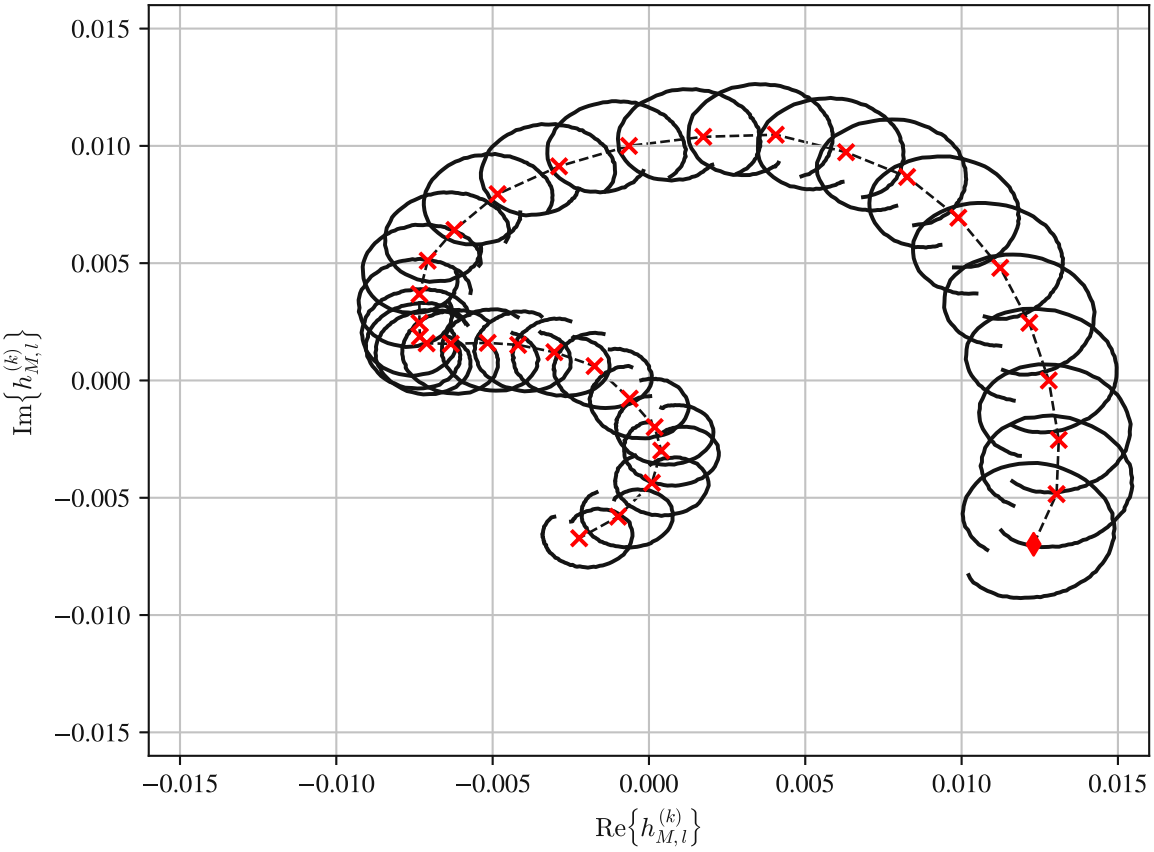

Figure 16: Results of the channel measurement at 5.65 GHz of measurement campaign A averaged over the 10 repetitions.

The position indices of the channel measurements in campaigns A, B and C are directly related to the individual, and due to the symmetry from the specular reflection movement pattern also total, path lengths between the antennas and RIS. The mapping for each position index l to its respective total path length $d_{tot,l}$ is plotted in Fig. 17. This movement pattern increases the distance of the RIS to the origin, i.e., its y-coordinate. As a consequence, since we keep the AOI and AOR constant and equal, the distances between antenna 1 and the RIS, and antenna 2 and the RIS are equal as well:

$$d_{tot,l} = 2d_{T,l} = 2d_{R,l}, \tag{2}$$

where $d_{T,l}$ and $d_{R,l}$ are the distances between the transmit antenna (mounted on carriage 1) and RIS, and receive antenna (mounted on carriage 2) and RIS. We can further rewrite (2) by replacing the distance $d_{T,l}$ or $d_{R,l}$ with its relation to the y-coordinates:

$$d_{tot,l} = 2\frac{\Delta y_l}{\cos\left(AOI\right)}, \tag{3}$$

with

$$\Delta y_l = y_l - y_1 = y_l - y_2. \tag{4}$$

Δy_l refers to the difference in the y-coordinates of the RIS y_l and the apertures of the horn antennas $y_{1|2}$ mounted on carriages 1 and 2 respectively. The reason why we cannot

simply take the y-coordinate of the RIS: y, directly, is that we want to minimize the error between the model path length $d_{tot,l}$ and the true path length, due to the distance to the phase centers of the horn antennas not being included in this model, as much as possible. $y_1 = y_2 = 0$ are the y-coordinates of the rotation axes of carriages 1 and 2. As a consequence of the definition of $d_{tot,l}$ in (3), the magnitudes of the x-coordinates of carriages 1: $|x_1|$ and 2: $|x_2|$ are the same, i.e.,

$$x_{1,l} = -x_{2,l}. \tag{5}$$

This relation between the total path length described in (3) and the position indices l is plotted in Fig. 17. The minimum path length is approximately 3.6 m and the maximum path length is around 5.1 m. Additionally, the farfield boundary is also plotted in this figure at a total path length of 4.57 m corresponding to the position index $l = 0$. This value was determined from the maximum of the farfield distances [23, Chapter 14.1] of the components involved, the RIS and the horn antenna, i.e.,

$$d_{tot,far} = 2d_{far} = \frac{4}{\lambda} \max\left\{D_{Horn}^2, D_{RIS}^2\right\} \approx 4.57\,\text{m}. \tag{6}$$

d_{far} denotes the farfield distance of one section of the path, e.g., the horn antenna 1 and the RIS. Due to the symmetry the total path length at this distance is double that value. D_{Horn} is the diagonal of the horn antenna aperture and D_{RIS} is assumed to be the diagonal of the metallic section of the RIS shown in Fig. 13. λ corresponds to the wavelength of the highest frequency to ensure that at other frequencies this boundary ensures that positions with index $l > 0$ are in the farfield.

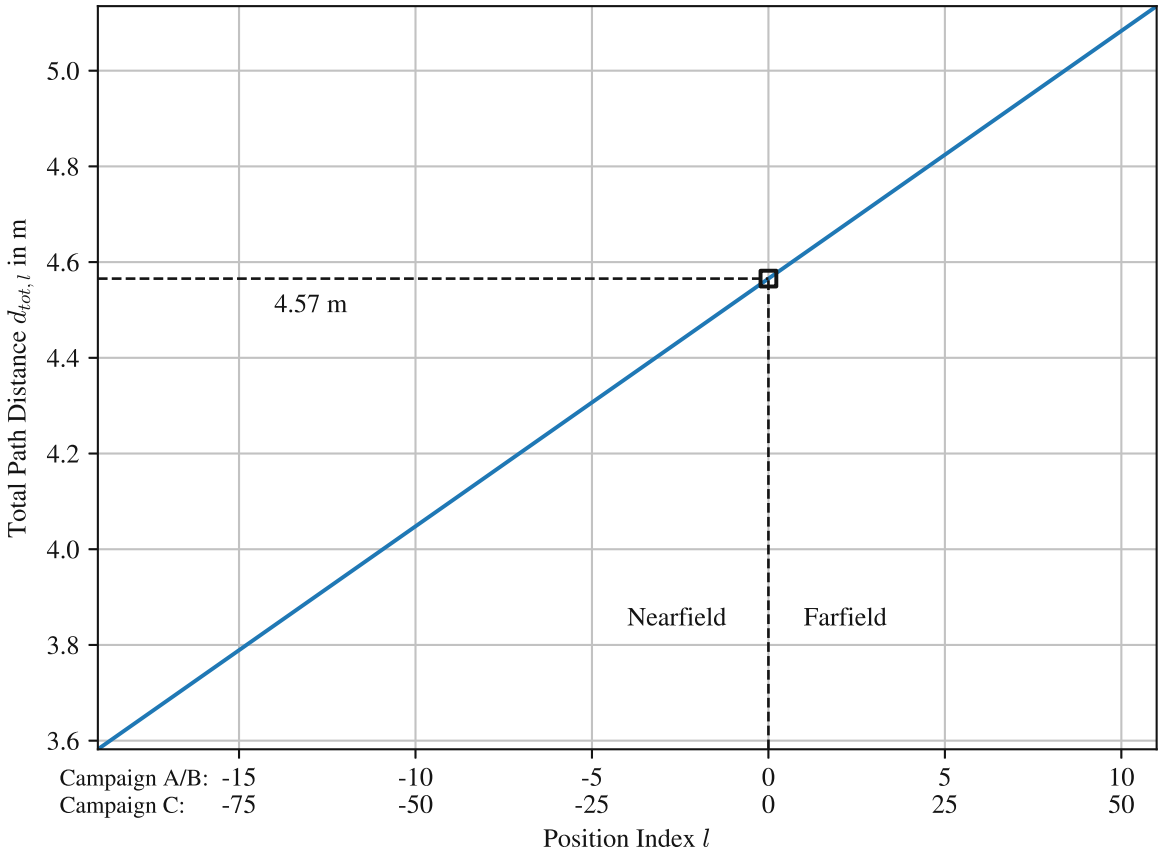

Figure 17: Mapping of position indices l of measurement campaigns A, B and C to the total path length $d_{tot,l}$.

3.2 Channel Model

In this section the channel model, that is used to process the data acquired from the measurement campaigns A,B and C, is presented. This model has been derived from the bistatic radar equation [23, Chapter 14.3] for a linear distance dependent phase shift [28, Chapter 5]. Before getting to the channel model itself, we introduce the variables that are part of this model in Table 3. Variables denoted by upper case letters are random or are related to a random variable. The index l describes the position of all components, k the RIS setting, i.e., the bias voltages applied to the RIS, and i the repetition number of the measurement.

Variable	Set	Description
$t_l(j\omega)$	$\mathbb{C}$	TX antenna transfer function
$r_l(j\omega)$	$\mathbb{C}$	RX antenna transfer function
$h_{T,l}(j\omega)$	$\mathbb{C}$	Channel transfer function for TX antenna to RIS
$h_{R,l}(j\omega)$	$\mathbb{C}$	Channel transfer function for RIS to RX antenna
$\gamma^{(k)}(j\omega)$	$\mathbb{C}$	RIS reflection coefficient
$H^{(k)}_{MPi,l}(j\omega)$	$\mathbb{C}$	Multipath contribution to the measured channel
$\tilde{N}_i(j\omega)$	$\mathbb{C}$	Additive White Gaussian Noise (AWGN) in the environment

Table 3: Description of the variables of the channel model.

The magnitudes of the antenna transfer functions are modelled by their position and frequency dependent gains $g_{T|R,l}(j\omega)$. Their position dependent phase shifts, $\phi_{T,l}$ and $\phi_{R,l}$, for the TX and RX antennas respectively, are assumed to be described by the location of their phase centers [29], [30]. We can therefore write the TX and RX antenna transfer functions as

$$t_l(j\omega) = \sqrt{g_{T,l}(j\omega)}\,\exp(j\phi_{T,l}), \tag{7}$$

and

$$r_l(j\omega) = \sqrt{g_{T,l}(j\omega)}\,\frac{\omega_c}{\omega}\,\exp(j\phi_{R,l}). \tag{8}$$

However, as the horn antenna radiation patterns do not exhibit a notable variation in frequency, the frequency dependency $\{\cdot(j\omega)\}$ is dropped from $g_{T|R,l}$. An additional consideration related to the RX antenna gain, was its relation to the effective antenna area [23, Chapter 14.1], which added the factor ω_c/ω to the RX antenna transfer function. This is necessary as the channel model is derived from the bistatic radar equation, and we need to convert the effective antenna area of the RX antenna to an equivalent gain. This relation is described by

$$g_{R,l} = \frac{\lambda^2}{4\pi}\,a_{R,l} = \frac{\pi c_0}{\omega^2}\,a_{R,l} \approx g_{T,l}\left(\frac{\omega_c}{\omega}\right)^2, \tag{9}$$

where $g_{T,l}$ is the antenna gain probe horn antenna of the TX and RX antennas. This gain can be reused in (9) as the TX and RX antennas are identical. The effective antenna area of the probe horn antenna on the receiver side is described by $a_{R,l}$, the wavelength is λ, c_0 is the speed of light and ω_c is the center frequency. As the main beam of this horn antenna always faces the RIS during the measurements, $g_{T,l}$ is approximated with

$$g_{T,l}|_{dB} = g|_{dB} = 18\,\mathrm{dBi}. \tag{10}$$

Next, we consider the phases of the antenna transfer functions (7) and (8). From considerations of the phase center of horn antennas [30], we know that the phase center can be approximated as a constant phase shift if the angle is kept constant. This removes the position dependency of the phase contributions of the antennas, and in conjunction with the approximation of (10), allows me to write $t_l(j\omega) = t(j\omega)$ and $r_l(j\omega) = r(j\omega)$. As the phase shifts from the antennas are now constant, the antenna transfer functions can be rewritten as

$$\begin{aligned} t(j\omega) &= \sqrt{g} \\ r(j\omega) &= \sqrt{g}\,\frac{\omega_c}{\omega}. \end{aligned} \tag{11}$$

This introduces a constant phase error that does not contribute to the characterization of the behavior of the RIS. Finally, we get to the transfer functions of the paths between the TX antenna and the RIS and the RX antenna and the RIS, described by

$$h_{T,l}(j\omega) = \frac{1}{\sqrt{4\pi}d_{T,l}} \exp\left(-j\omega d_{T,l}/c_0\right), \tag{12}$$

for the TX-RIS part and

$$h_{R,l}(j\omega) = \frac{1}{\sqrt{4\pi}d_{R,l}} \exp\left(-j\omega d_{R,l}/c_0\right), \tag{13}$$

for the RX-RIS part. $d_{T,l}$ is the path length between the TX antenna and the RIS and $d_{R,l}$ the path length between the RX antenna and the RIS.

To simplify the description of this measurement model in the following equations, the written representation of the frequency dependency of all components $\{\cdot(j\omega)\}$ will be omitted on the right hand side of the equation.

Next, a basic model derived from the bistatic radar equation, using the components defined above is constructed:

$$H^{(k)}_{Mi,l}(j\omega) = t\,h_{T,l}\,\gamma^{(k)}\,h_{R,l}\,r + H^{(k)}_{MPi,l} + \tilde{N}_i, \tag{14}$$

where $H^{(k)}_{Mi,l}(j\omega)$ is the measured channel transfer function at a position l with a RIS setting k and repetition number, or time instant, i. The RIS reflection coefficient $\gamma^{(k)}$, per the above definition, only depends on the bias voltages applied to the varactor diodes (the RIS setting) and the measurement frequency. Due to the derivation of the model from the bistatic radar equation, this reflection variable is related to the radar cross-section of the RIS. From Fig. 15 and Fig. 16 we see that the individual spirals rotate around the origin at an offset. From the model introduced in [21] it is expected that the spirals overlap at the origin. A lossless RIS would have its phase shifts located on the unit circle, e.g., in the case of a RIS with only one element we would have a reflection coefficient that is described as

$$\tilde{\gamma}^{(k)} = \exp\left(j\phi^{(k)}_{RIS}\right), \tag{15}$$

where $\phi^{(k)}_{RIS}$ is the RIS setting dependent phase shift of the RIS element and $\tilde{\gamma}^{(k)}$ represents the reflection from an idealized RIS. In addition to this reflection coefficient,

we can also consider the rotation resulting from the total path length. The total phase shift we then expect at the receiver is approximately

$$\phi_{tot}^{(k)} = \phi_{RIS}^{(k)} + \frac{\omega d_{tot,l}}{c_0}, \tag{16}$$

where $d_{tot,l}$ is the total path length. The different positions, with varying distances result in a rotation of the lossless RIS reflection $\exp\left(j\phi_{RIS}^{(k)}\right)$, i.e., a rotation of all points on the unit circle around the origin. However, what was measured and is presented in Fig. 15 and Fig. 16 does not match these expectations. Therefore, a more generalized model for the RIS is needed. The reflection coefficient $\gamma^{(k)}$ will now be defined as

$$\gamma^{(k)} = \gamma_S + \gamma_D^{(k)}, \tag{17}$$

where γ_S describes the static offset of the reflection coefficient from the origin, independent of the applied RIS setting k. $\gamma_D^{(k)}$ then defines the dynamic component of the reflection coefficient, dependent on the applied RIS setting k. To be able to process the measured data, the origin of the spiral is defined as

$$\gamma^{(0)} = \gamma_S, \tag{18}$$

with

$$\gamma_D^{(0)} = 0. \tag{19}$$

Next, we consider a simplification of the model proposed in (14). Firstly, it is assumed that the interference from the environment described by $H_{MPi,l}^{(k)}(j\omega)$ consists of a superposition of a deterministic part, which only depends on the positions of all interacting objects and the applied RIS setting, and a random random part dependent on the time instant i. This random part is assumed to be zero mean. Secondly, the noise $\tilde{N}_i$ is assumed to be AWGN.

To confirm this assumption, the ensemble average of $H_{Mi,l}^{(k)}(j\omega)$ over the time instant i,

$$h_{M,l}^{(k)}(j\omega) = \mathop{\mathbb{E}}_{i}\left\{H_{Mi,l}^{(k)}(j\omega)\right\} = t \cdot h_{T,l} \cdot \gamma^{(k)} \cdot h_{R,l} \cdot r + h_{MP,l}^{(k)}, \tag{20}$$

with $\mathbb{E}\{\cdot\}$ as the expectation operator, is subtracted from the measured data with

$$N(j\omega) = H_{Mi,l}^{(k)} - h_{M,l}^{(k)} = H_{MPi,l}^{(k)} - h_{MP,l}^{(k)} + \tilde{N}_i, \tag{21}$$

where the difference $H_{MPi,l}^{(k)} - h_{MP,l}^{(k)}$ represents the random interference intruding into the measurement environment. The data that will be presented in the following figures was obtained from measurement campaign B described in Table 2. Compared to campaigns A and C, each measurement of campaign B, described by RIS setting k and position l together, was repeated 100 times. The histogram of the real- and imaginary part of $N(j\omega)$ is plotted in Fig. 18. The frequencies of the Gaussian distribution (dashed lines) were scaled to support the comparison with the histograms. Both parts appear to follow a zero-mean gaussian distribution implied by the black dashed line, with the same variance $\sigma_N^2 \approx 10^{-9}$. To confirm this theory, the Kolmogorov-Smirnov test [31], comparing the 100 samples at each measurement position to the distribution of a gaussian distribution, is performed. An implementation of this test provided in the Python package *scipy* [32]

and named *kstest* was used. The variance and mean of the gaussian distribution at each position are determined as the variance and mean of the 100 samples. The mean can be attributed to the deterministic part of the channel described in (20), implying that the mean of the gaussian distribution itself is zero. The variance σ_N^2 is approximately the same value at each position. The threshold of this test was a 95 % confidence level. The distributions of the real and imaginary parts at all positions have passed this test, confirming that they indeed follow the gaussian distribution. This result shows that, considering the zero mean and same variance at all positions, the distribution is identical and gaussian for all positions. Additionally, we can assume that $H_{MPi,l}^{(k)} - h_{MP,l}^{(k)}$ also follows a zero mean gaussian distribution. By taking the ensemble average of the measurements, the noise contribution is therefore removed. For the results presented later in this chapter, the Signal to Noise Ratio (SNR) at the measurement positions is of interest.

It is computed as

$$\mathrm{SNR} = \frac{\left|\mathbb{E}_i\left\{H_{Mi,l}^{(k)}\right\}\right|^2}{\mathrm{Var}_i\left\{H_{Mi,l}^{(k)}\right\}} \tag{22}$$

with i indicating the repetition index of a measurement at position l with RIS setting k. $\mathrm{Var}\{\cdot\}$ is the variance operator. In Fig. 19 the SNR is displayed for the nearfield positions (position indices lower than zero) close to the farfield boundary and the farfield

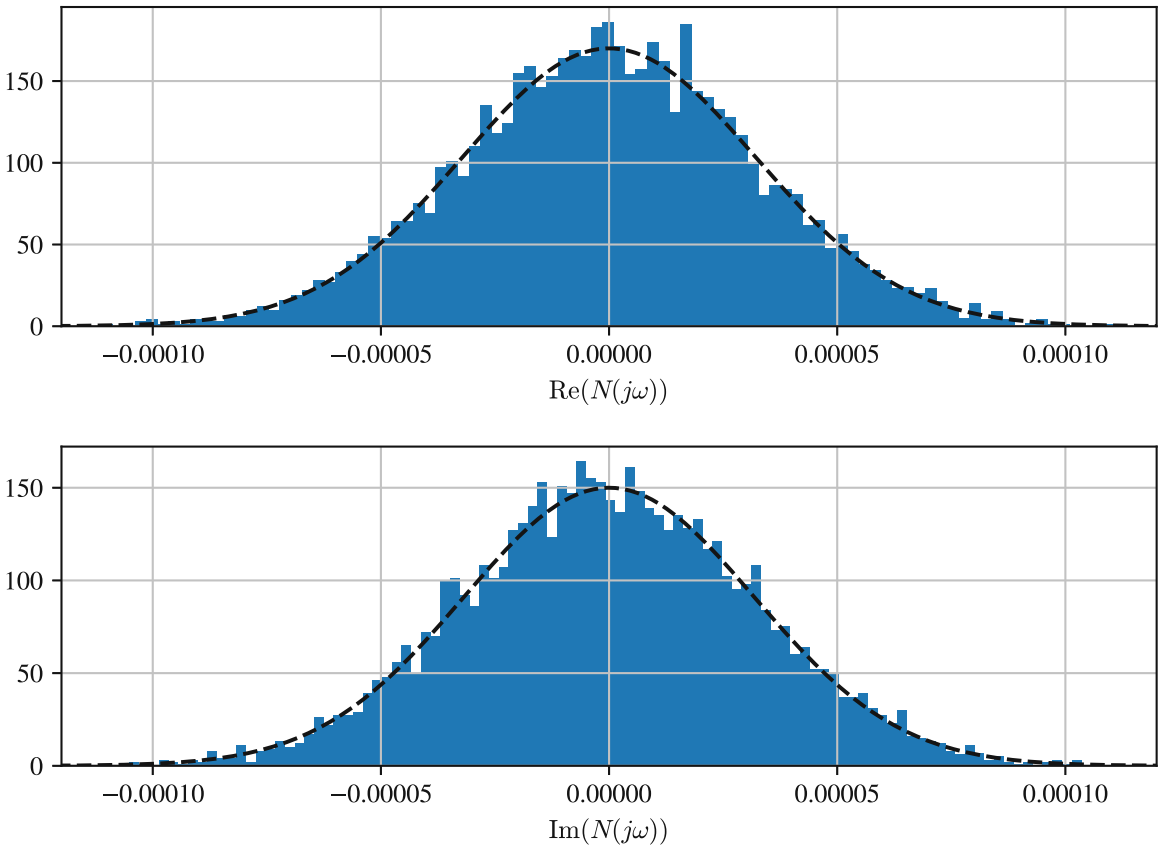

Figure 18: Noise distribution of all farfield positions $l \geq 0$ and RIS setting $k = 0$.

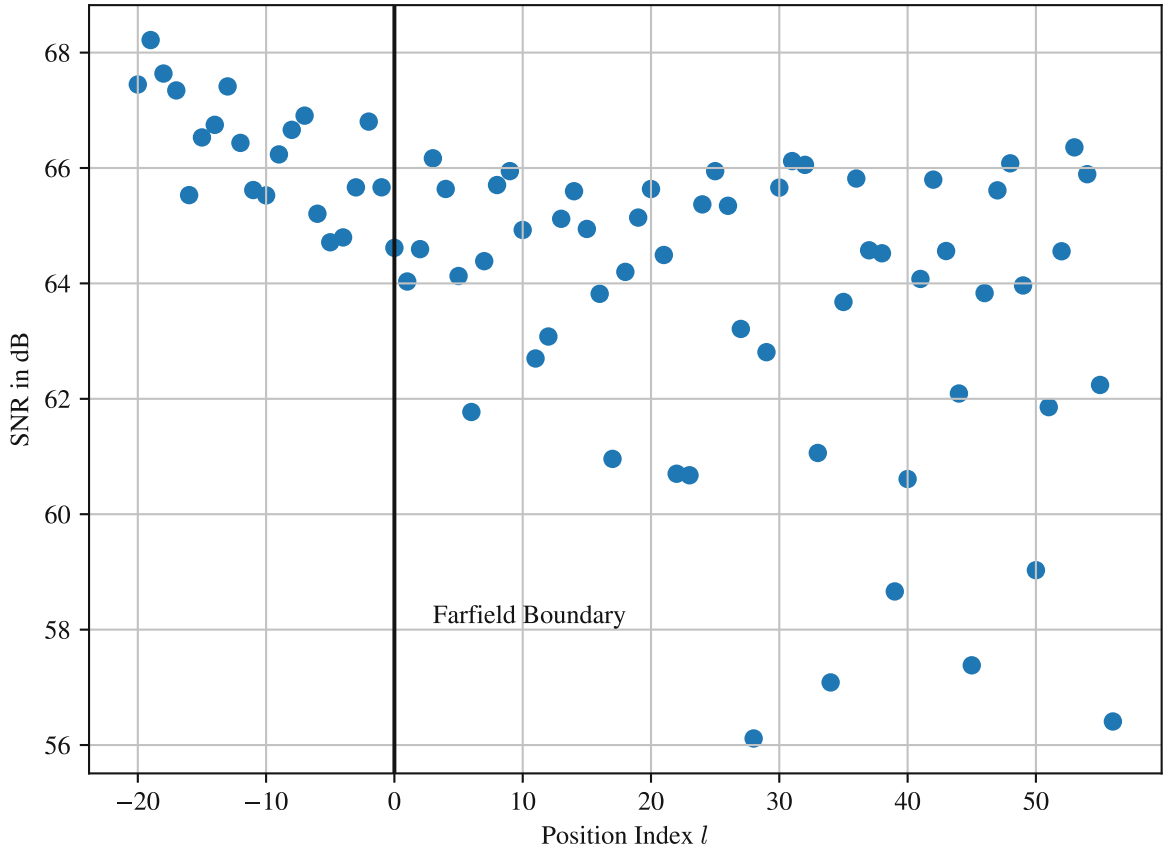

Figure 19: SNR over all positions at RIS setting $k = 0$.

positions (position indices larger than zero). The values have been calculated using the data from measurement campaign C defined in Table 2, with a large number of positions in a specular reflection position pattern with an angle of incidence of 15° at 5.4 GHz, i.e., the angle remains constant while the total path length

$$d_{tot,l} = d_{T,l} + d_{R,l} \tag{23}$$

increases. The farfield boundary at position $l = 0$ is at a distance of approximately 2.285 m between the RIS and one antenna. This is the distance, at which all frequencies are in the farfield, i.e., the farfield distance calculated for the highest frequency 6 GHz. This does introduce a tolerance to the farfield distance at the lower frequencies. It is 1.9 m at the lowest frequency 5 GHz. The minimum distance at position $l = -95$ is 1.79 m and the maximum distance at position $l = 56$ is 2.567 m. In the farfield, the points are scattered over a larger value range due to multiple paths over various scattering objects affecting the received signal power. With an SNR well above 50 dB it is clear that noise is not a concern for this system. Rather, the large variation in SNR in the farfield indicates that the scattering will likely have a major undesirable effect on the measurements.

3.2.1 Evaluation of the Processed Measurements at 5.4 GHz

In this section, we aim to characterize the reflection coefficient of the RIS $\gamma^{(k)}$ at a single frequency, at 5.4 GHz. We first investigate the dynamic reflection coefficient $\gamma_D^{(k)}$. Based

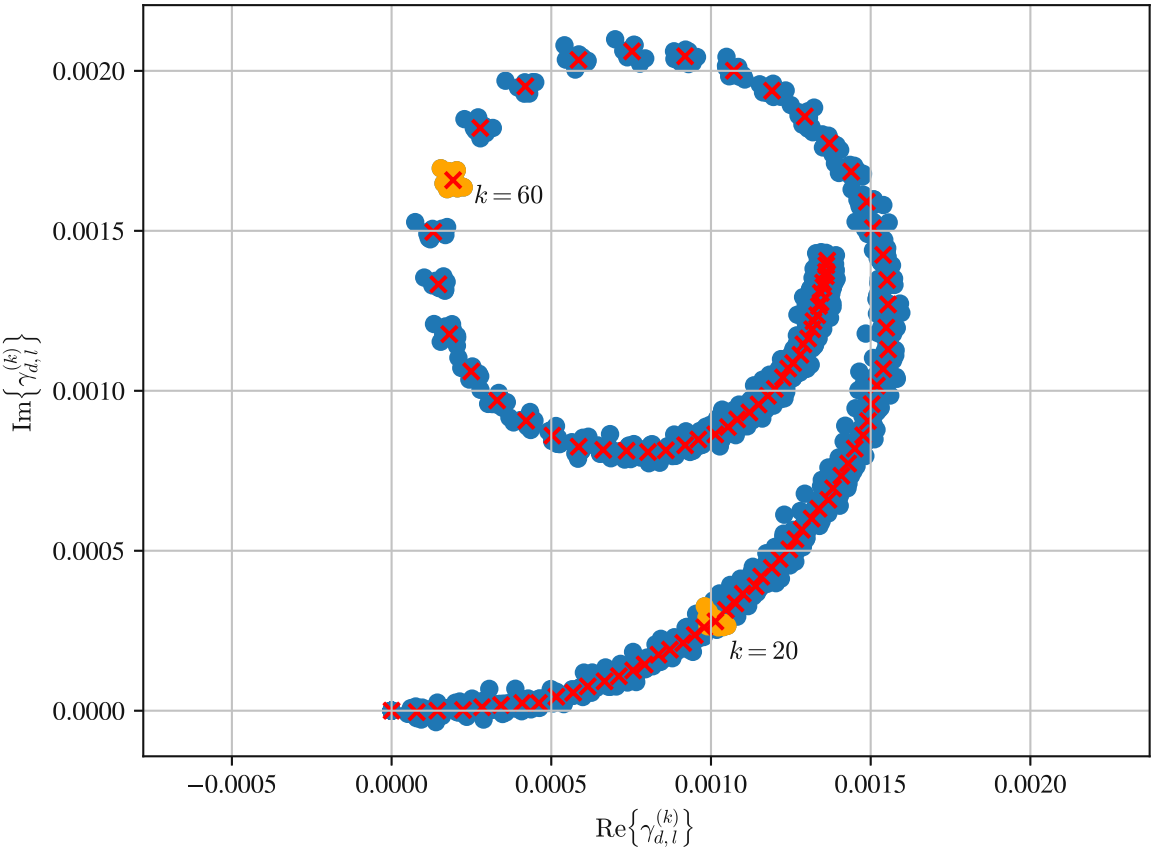

Figure 20: Differential RIS reflection coefficient $\gamma_{d,l}^{(k)}$.

on the model assumptions thus far, some information on $\gamma_D^{(k)}$ can already be extracted. For this purpose, the measurement with RIS setting $k = 0$ at all positions l, $h_{M,l}^{(0)}$, is subtracted from the measured channel transfer function $h_{M,l}^{(k)}$. The resulting differential channel is written as

$$h_{d,l}^{(k)} = h_{M,l}^{(k)} - h_{M,l}^{(0)} = t\, h_{T,l}\, \gamma_D^{(k)}\, h_{R,l}\, r + h_{dMP,l}^{(k)}, \tag{24}$$

with the differential scattering term $h_{dMP,l}^{(k)} = h_{MP,l}^{(k)} - h_{MP,l}^{(0)}$ and the position independent, dynamic reflection coefficient $\gamma_D^{(k)} = \gamma^{(k)} - \gamma^{(0)}$. To extract the dynamic reflection coefficient, we first need to reformulate (24) by dividing by the known components: t, r, $h_{T,l}$ and $h_{R,l}$, into

$$\gamma_{d,l}^{(k)} = \frac{h_{d,l}^{(k)}}{t\, h_{T,l}\, h_{R,l}\, r} = \gamma_D^{(k)} + \frac{h_{dMP,l}^{(k)}}{t\, h_{T,i}\, h_{R,l}\, r} = \gamma_D^{(k)} + \gamma_{dMP,l}^{(k)}, \tag{25}$$

with the position dependent, differential scattering term $\gamma_{dMP,l}^{(k)}$, where $\gamma_{d,l}^{(k)}$ represents the differential reflection component. While we have isolated $\gamma_D^{(k)}$ in (25), a multipath term, $\gamma_{dMP,l}^{(k)}$, remains. Due to this term, the *differential* reflection coefficient $\gamma_{d,l}^{(k)}$ is not the same as the *dynamic* reflection coefficient $\gamma_D^{(k)}$. It would only be equivalent if $\gamma_{dMP,l}^{(k)}$ were zero. This differential RIS reflection coefficient $\gamma_{d,l}^{(k)}$, computed according to (25) at

5.4 GHz, is shown in Fig. 20. It was calculated from the data acquired during measurement campaign A, with 12 farfield positions and specular reflection with a 15° angle of incidence. Fig. 20 displays a set of spirals (one for every farfield position) overlaid over each other. Due to this, we can now see only one spiral composed of a large number of clusters, with each cluster having a common RIS setting k. This composite spiral starts at the origin with $\gamma_{d,l}^{(0)} = 0$ and proceeds in a counter clockwise manner with increasing k. The blue points represent $\gamma_{d,l}^{(k)}$ and the red crosses are the average over all positions l, i.e., the mean of a single cluster,

$$\overline{\gamma}_d^{(k)} = \mathop{\mathbb{E}}_{l} \left\{ \gamma_{d,l}^{(k)} \right\}. \tag{26}$$

In Fig. 20 the blue points corresponding to any RIS setting k appear to cluster around some center point. Two clusters have been highlighted in orange in Fig. 20. The cluster at RIS setting $k = 20$ is partially obscured by the overlapping neighboring clusters. We see that its shape is similar to the cluster at $k = 60$, which is displayed without overlap. In Fig. 21 we now focus on the $k = 50$ cluster, located in the top right part of Fig. 20. It shows that the points are not fully random but are arranged in an approximate circle, starting at position $l = 0$ with the diamond marker and progressing in a clockwise manner. This pattern can be attributed to a small error in the path lengths between the RIS and antennas $d_{T,l}$ and $d_{R,l}$ as well as a remaining random scattering from the environment.

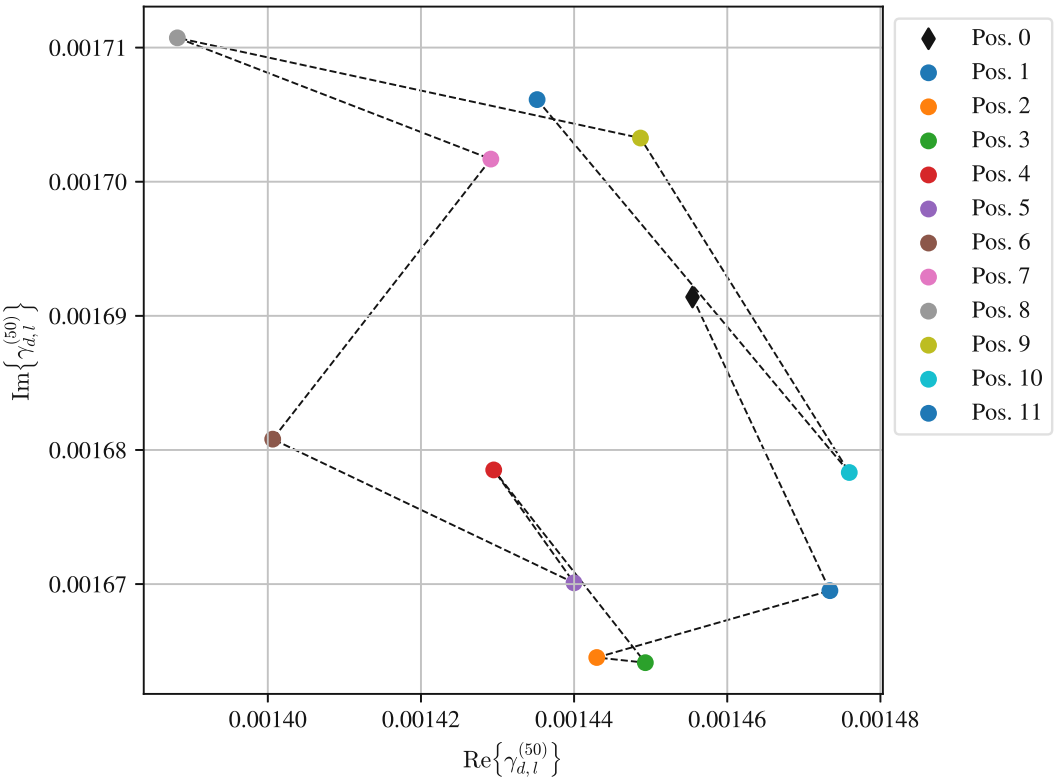

Figure 21: Differential RIS reflection coefficient $\gamma_{d,l}^{(k)}$ at RIS setting $k = 50$.

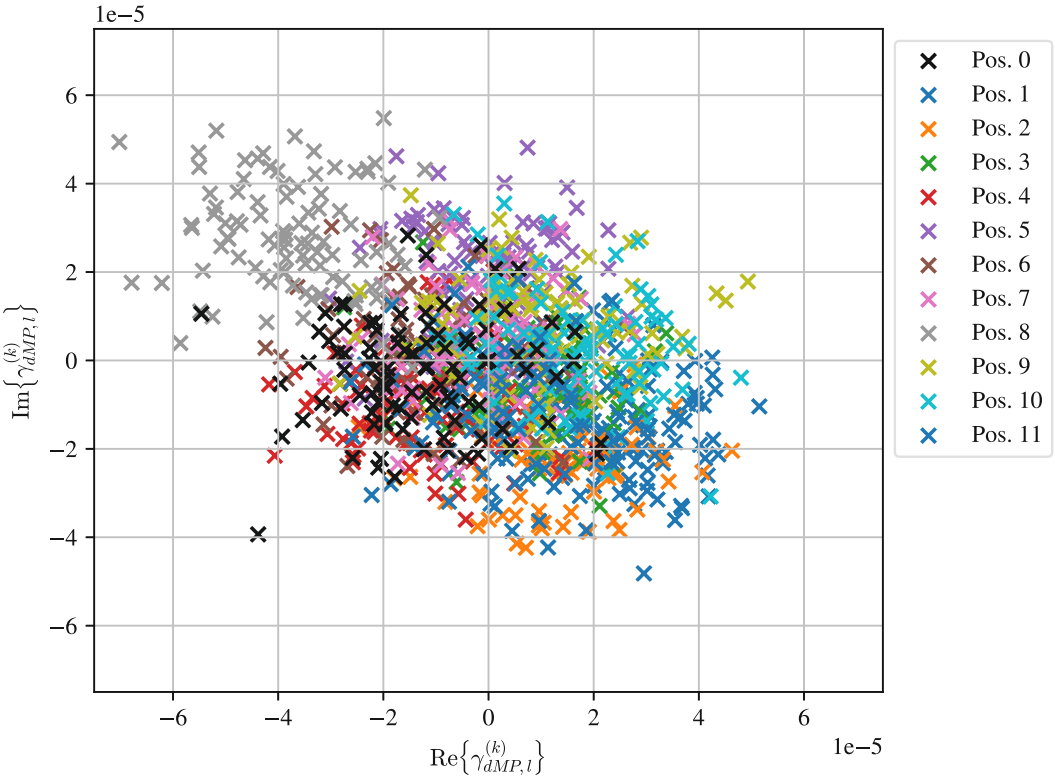

Figure 22: Differential multipath components $\gamma^{(k)}_{dMP,l}$ separated by position.

As the positional average $\overline{\gamma}^{(k)}_d$ in Fig. 20 is clearly marked by red crosses, each cross corresponding to a RIS setting cluster, it becomes apparent that the cluster center likely coincides with this mean value. The dynamic reflection component will therefore be defined as the positional mean of the overlaid spirals:

$$\gamma^{(k)}_D = \overline{\gamma}^{(k)}_d. \tag{27}$$

Using the above definition of $\gamma^{(k)}_D$, a closer look at the differential multipath term $\gamma^{(k)}_{dMP,l}$ is now possible. In Fig. 22 this multipath term is plotted for each farfield position, denoted as "Pos. l", with l being the position index. Each position is marked in a unique color, besides positions 1 and 11, as the position 1 crosses are hidden underneath the other clusters. Fig. 22 shows that some position clusters of $\gamma^{(k)}_{dMP,l}$ exhibit a position dependency, with the cluster centers not being centered on the origin. The differential scattering $\gamma^{(k)}_{dMP,l}$ within one cluster l, appears to be randomly distributed in relation to the RIS settings k. The distribution of clusters seem to display a correlation between the real part and imaginary part. This is likely a coincidence due to the strong deviation from the origin by the points of position 8.

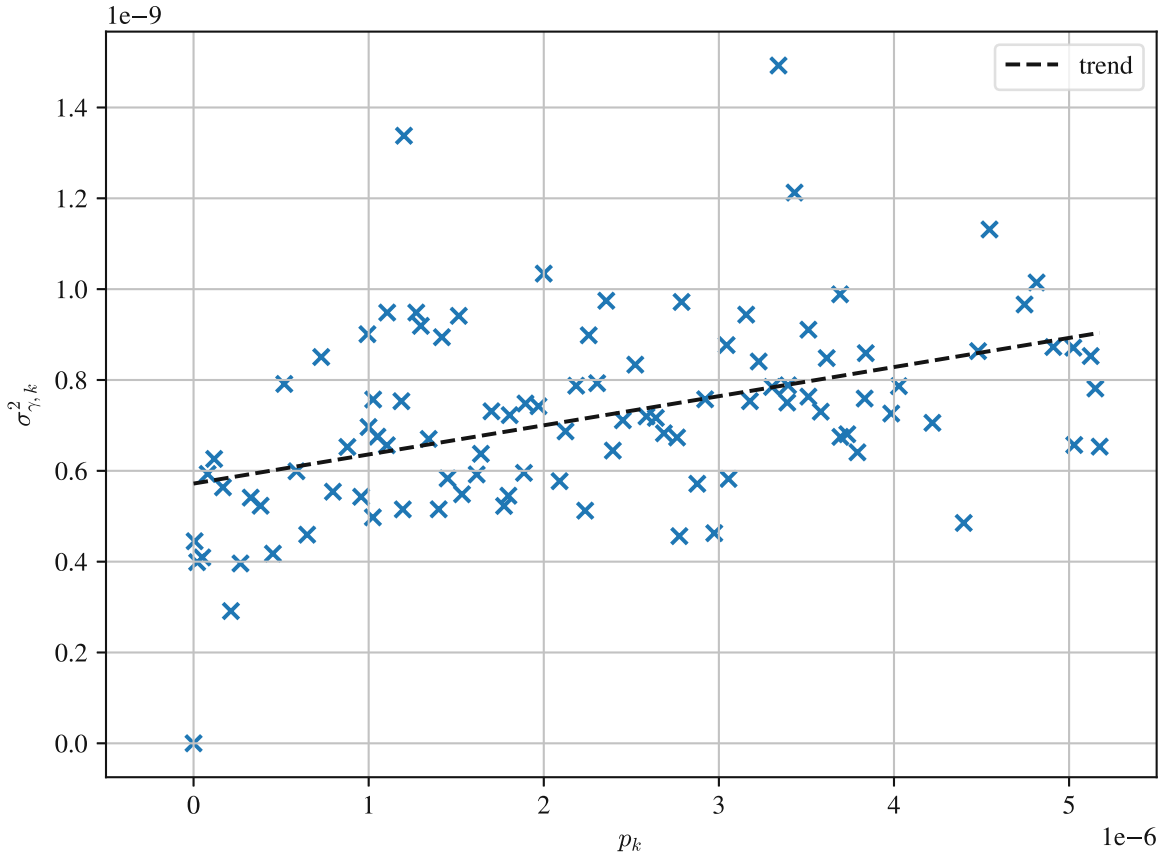

Figure 23: Variance of the scattering over all positions l, $\sigma^2_{\gamma,k} = \mathrm{Var}_l\left\{\gamma^{(k)}_{d,l}\right\} = \mathrm{Var}_l\left\{\gamma^{(k)}_{dMP,l}\right\}$, around the dynamic reflection component $\gamma^{(k)}_D$ in relation to the power of $\gamma^{(k)}_D$ for the same RIS setting k.

An additional point of interest is the relation between the variance of individual clusters of $\gamma^{(k)}_{d,l}$:

$$\sigma^2_{\gamma,k} = \mathrm{Var}_l\left\{\gamma^{(k)}_{d,l}\right\} \tag{28}$$

and the power of the dynamic reflection coefficient

$$p_k = \left|\gamma^{(k)}_D\right|^2, \tag{29}$$

i.e., the magnitude of the center of the cluster. Fig. 23 then shows that there exists a correlation between these two variables. This correlation can be calculated with

$$R_{\sigma^2_\gamma,p} = \frac{\mathrm{Cov}_k\left\{\sigma^2_{\gamma,k}\, p_k\right\}}{\sqrt{\mathrm{Var}_k\left\{\sigma^2_{\gamma,k}\right\}\mathrm{Var}_k\left\{p_k\right\}}} = 0.44, \tag{30}$$

with the covariance of p_k and $\sigma^2_{\gamma,k}$:

$$\mathrm{Cov}_k\left\{\sigma^2_{\gamma,k}\, p_k\right\} = \mathop{\mathbb{E}}_k\left\{\left(\sigma^2_{\gamma,k} - \mathop{\mathbb{E}}_k\left\{\sigma^2_{\gamma,k}\right\}\right)\left(p_k - \mathop{\mathbb{E}}_k\left\{p_k\right\}\right)\right\}. \tag{31}$$

This result shows that, while there is a relation between these variables, it is not very strong. This correspondence could result from the scattering from multiple objects. The larger amplitudes of the reflection coefficient may increase the power of the signals received from the longer paths, containing the scattering objects in the environment and the RIS.

3.2.2 RIS Reflection $\gamma^{(k)}$

Now returning to the model description in (14), we see that the RIS reflection component $\gamma^{(k)}$ remains to be discussed. The dynamic component introduced with the differential model in (24), describes the changes in the reflection coefficient due to the change in the bias voltages applied to the varactor diodes on the RIS. In (17) we defined the RIS reflection coefficient as a superposition of a static and a dynamic reflection component due the initial channel measurements shown in Fig. 15 and Fig. 16 not matching the expectations set by [21]. For reference, the total reflection coefficient of the RIS, defined in (17), is described as

$$\gamma^{(k)} = \gamma_S + \gamma_D^{(k)}.$$

To reiterate, the static component γ_S was defined as the value of the RIS reflection coefficient at $k = 0$, with $\gamma_D^{(0)} = 0$ in (18) and is independent of both the position and RIS setting. To determine this static part, the channel model in (20) is reformulated into

$$\gamma_l^{(k)} = \frac{h_{M,l}^{(k)}}{t\, h_{T,l}\, h_{R,l}\, r} = \gamma^{(k)} + \frac{h_{MP,l}^{(k)}}{t\, h_{T,l}\, h_{R,l}\, r} = \gamma^{(k)} + \gamma_{MP,l}^{(k)}, \tag{32}$$

with $\gamma_l^{(k)}$, the total, position dependent, reflection coefficient and $\gamma_{MP,l}$ as the position and RIS setting dependent, multipath term.

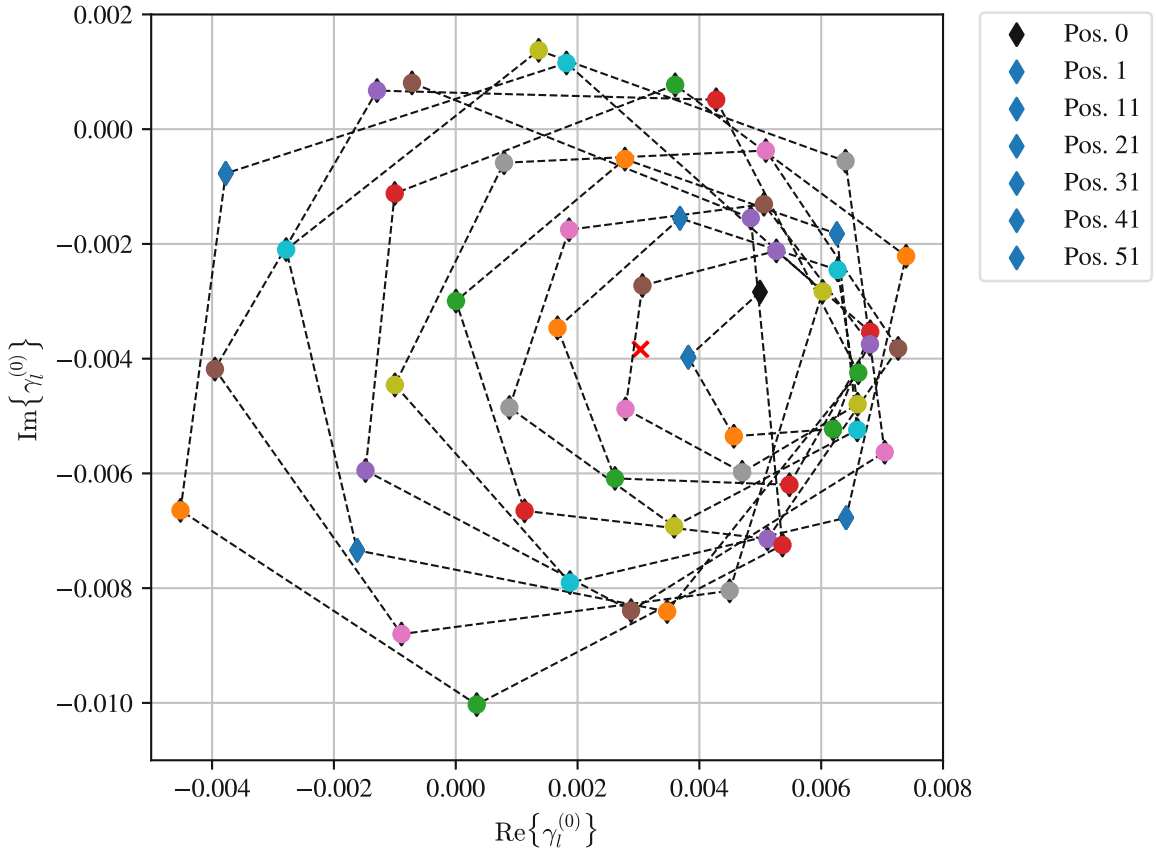

Figure 24: Reflection measurement with RIS setting $k = 0$ and 52 farfield positions from measurement campaign C.

However, before the static component γ_S can be pinned down, the multipath environment affecting the total reflection coefficient $\gamma_l^{(k)}$ must be understood. In Fig. 24, $\gamma_l^{(k)}$ has therefore been limited to $k = 0$. In this figure, we observe a large spiral pattern whose "radius" increases with rising position index l. A subset of these positions are marked with a blue diamond and listed in the graph's legend. With this listing, we see that the spiral begins at the black diamond marker and progresses in a counter-clockwise fashion. We also see, that many markers appear to cluster together at the center right of the figure. The remaining markers are spread out, some are located close to the origin, exhibiting only a low magnitude and some markers are placed at a greater distance from the origin of the figure. This behavior matches expectations, when considering multipath scattering. Depending on the position, we may have constructive or destructive interference between the scattered paths and the path of the RIS reflection. A large number of markers exhibit a similar, large distance from the origin, indicating constructive interference between the paths. The positions close to the origin display destructive interference, where the individual multipath components of the channel and the RIS reflection, cancel each other out.

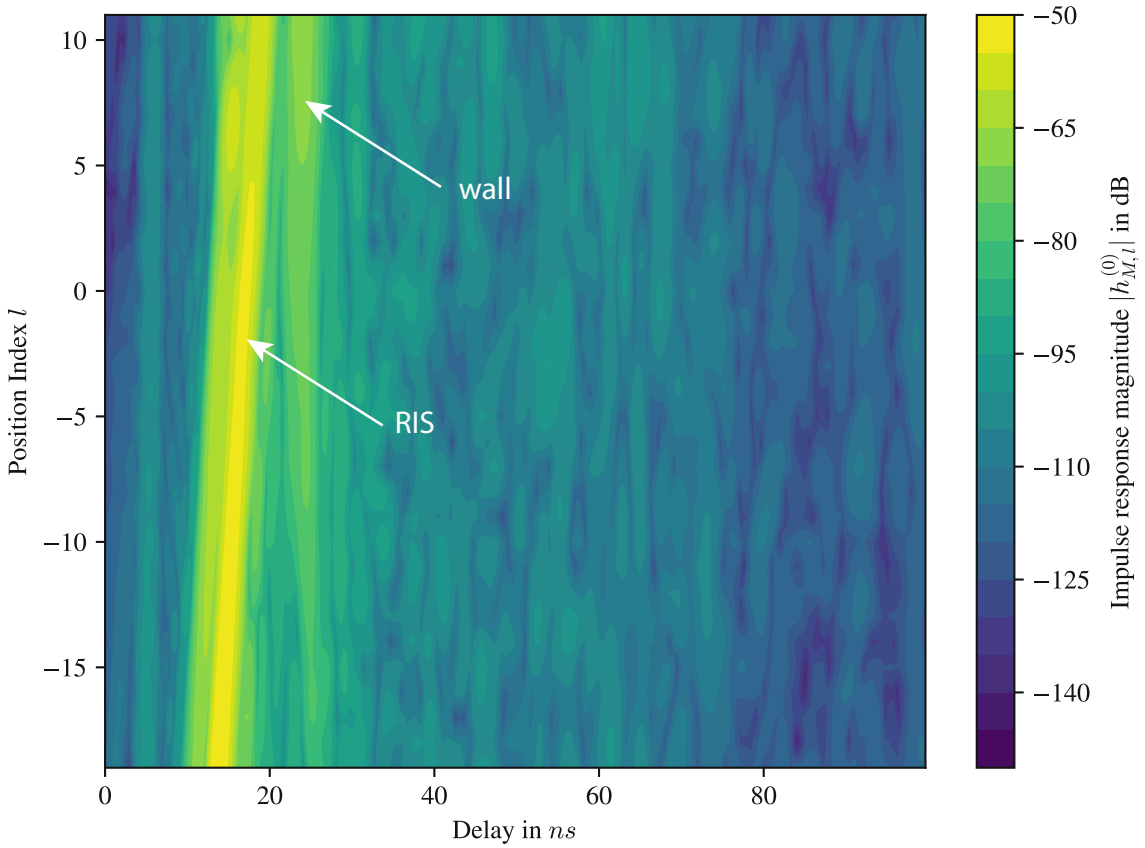

Figure 25: Impulse response of the channel over position indices l.

Next we will analyze the magnitude of the impulse response of the measured channel with RIS setting $k = 0$, depicted in Fig. 25, and identify the multipath components present in the measurement environment. It shows that the main contribution comes from the reflection of the RIS, as a diagonal line at approximately 20 ns with a magnitude above −60 dB. A second, strong contribution peaks around position $l = -8$, with a magnitude between −45 dB and −60 dB. It occurs immediately before the RIS reflection, to the left of the diagonal line of the strongest reflection. Additionally, it appears to be present at all positions, but at a lower magnitude within the range of −60 dB and −75 dB. Since this line is parallel to the RIS reflection diagonal line, it is likely located on or near the RIS. Due to the insufficient spatial resolution of about 30 cm, with the measurement bandwidth of 1 GHz, it is impossible to identify, whether this line is a reflection from the mounting structure of the RIS or part of the RIS reflection itself.

A second multipath contribution occurs at a delay of approximately 25 ns and displays a wedge-like shape of its peak along the position axis. It appears to be only slightly affected by the change in position, due to it being almost vertical. The phenomenon gains in width on the delay axis with increasing position indices. Due to its position on the delay axis, we can identify this contribution to most likely be a result from the scattering from the wall behind the RIS mounting structure. It is always in view of the main beam of the probe antennas and while it is partially covered by the RIS and the absorbing elements surrounding it, its large surface area is likely to scatter much of the transmitted power back to the receive antenna. The RIS mount moving closer to the

wall with increasing l also explains the increasing width of this component in Fig. 25. Moving closer to the wall, means that from the perspective of the antennas, less of the wall is covered by the absorbers surrounding the RIS. This increases the effective area contributing to the scattering at this delay, compensating for the increased attenuation due to a small increase in distance and enabling a larger spread in time.

An anomaly is visible at a delay of about 5 ns; a vertical line parallel to the position axis. This implies an interacting object at a total path length of about 1.5 m. However, there is no obvious object with this path length in front of the antennas. An argument could be made that this may be scattering from the floor being picked up by a sidelobe of the radiation pattern of the probe antenna. However, as the antennas move and increase the distance between each other, there should be a change in delay and channel magnitude, i.e., the anomalous line would have to be diagonal. This phenomenon is therefore probably an effect of the calibration of the measurement device.

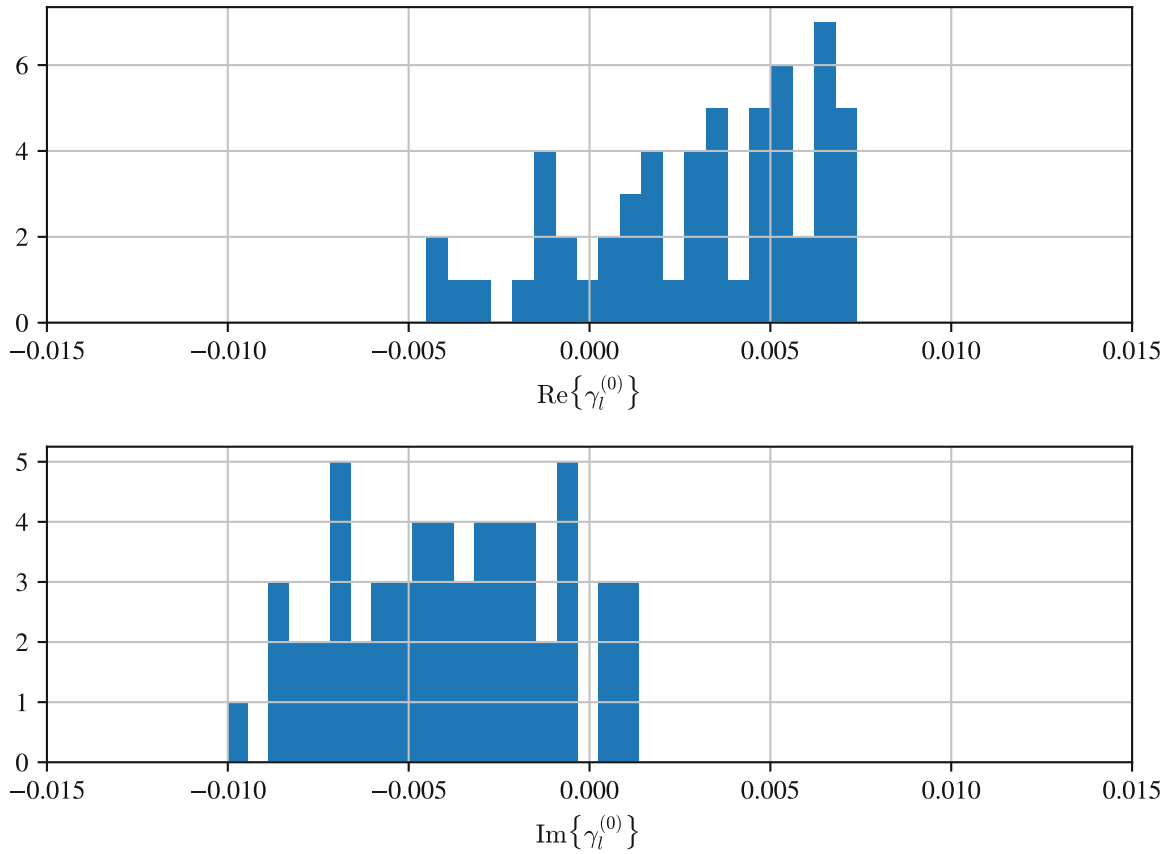

Figure 26: Distributions of the real and imaginary parts of the reflection coefficient $\gamma_l^{(k)}$ for RIS setting $k = 0$ shown in Fig. 24.

After evaluating the components in Fig. 25 as well as the pattern of Fig. 24 the assumption is made, that the static reflection coefficient can be approximately attained by taking the average of $\gamma_l^{(0)}$ over all positions l, with

$$\gamma_S = \mathop{\mathbb{E}}_{l}\{\gamma_l^{(0)}\}. \tag{33}$$

Now that γ_S has been defined in (33), we need to analyze the divergence of this assumption to the "true" value of γ_S. Obviously, as the true γ_S is unknown, we can only investigate the distribution of $\gamma_l^{(0)}$ over which the mean was calculated. Fig. 26 depicts the histograms of the real and imaginary parts of $\gamma_l^{(0)}$. We see immediately, that the measured values are not zero mean, resulting in an offset to the static component γ_S. While it will influence the result for γ_S, i.e., introducing an unknown shift from the true value, it is unlikely to have a direct impact on the evaluation of the performance of the RIS. To perform some measure of beam-focusing, the RIS would ideally be able to provide phase shifts up to 180°. And though the actual "center" point of the recorded spiral shown in Fig. 20 is unknown, an equally important operating point could be chosen as a virtual "center" of phase shifts. The components that sum up to this chosen point do not need to be known to make use of the beam-focusing capability of the RIS with the chosen bias voltages (and therefore phase shifts).

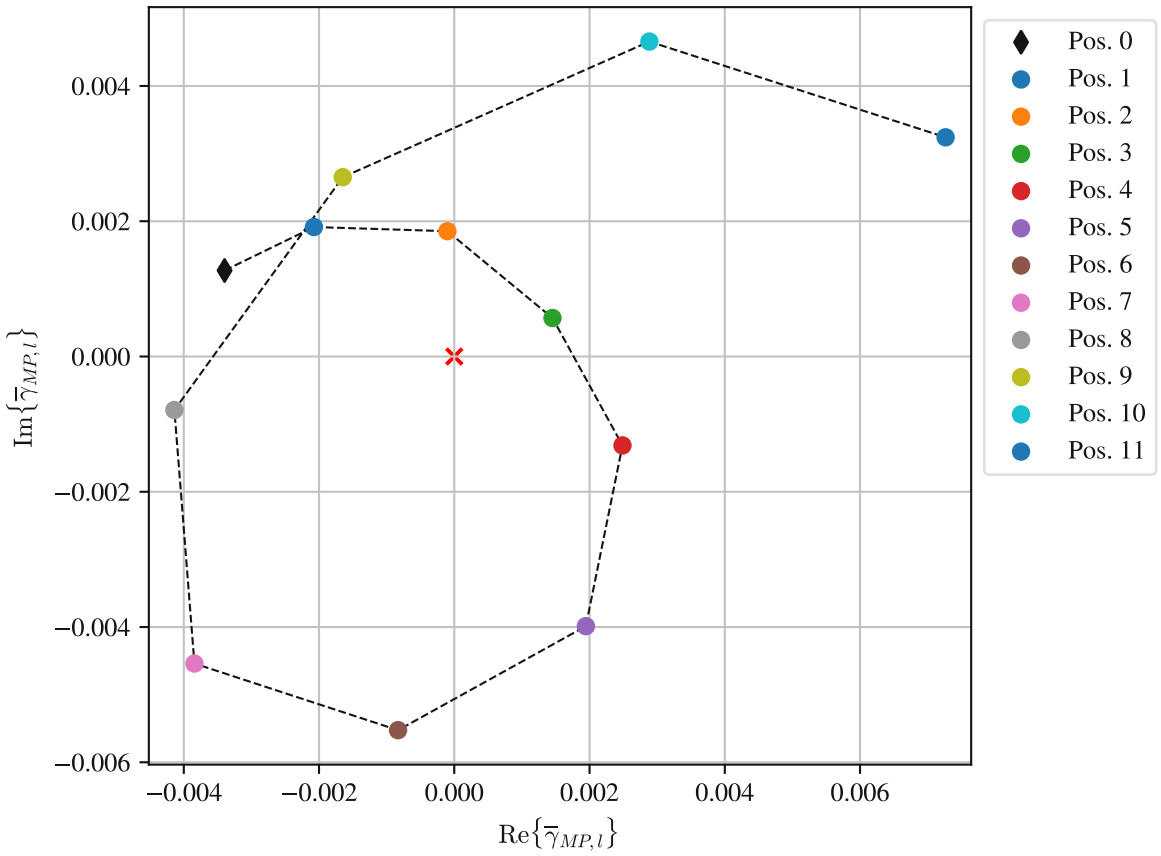

Figure 27: Mean values of the clusters of the position dependent multipath contribution, $\overline{\gamma}_{MP,l} = \mathbb{E}_k \left\{ \gamma_{MP,l}^{(k)} \right\}$, to the measured reflection of the RIS.

Let us next focus on the multipath contribution $\gamma_{MP,l}^{(k)}$ to the reflection coefficient $\gamma_l^{(k)}$, introduced in (32). In Fig. 27 the position dependent part is visible. The points represent the scattering factors $\gamma_{MP,l}^{(k)}$ at their respective positions l beginning with the black diamond on the left and progressing clockwise with varying magnitude. Each individual position marker is the average of $\gamma_{MP,l}^{(k)}$ over the RIS settings k with

$$\overline{\gamma}_{MP,l} = \mathop{\mathbb{E}}_{k} \left\{ \gamma_{MP,l}^{(k)} \right\}. \tag{34}$$

The red cross marks the positional mean of $\gamma_{MP,l}^{(0)}$, $\mathbb{E}_l \left\{ \gamma_{MP,l}^{(0)} \right\}$, which is zero due to the definition of γ_S. Positions 0 to 4 and position 9, display only a small magnitude compared to the other positions. This is behavior likely results from the same constructive and destructive interference that was previously discussed with Fig. 24. We will now zoom in on position 7 in Fig. 28, located at the bottom left in Fig. 27, to investigate the placement of values in relation to RIS setting k. The distribution shown in Fig. 28 follows no obvious pattern and appears to be clustered around a center point. This is likely to be the cluster mean, marked by a red cross. The only fact that we can identify, is that the density of points is higher close to the cluster mean, compared to points with a larger distance.

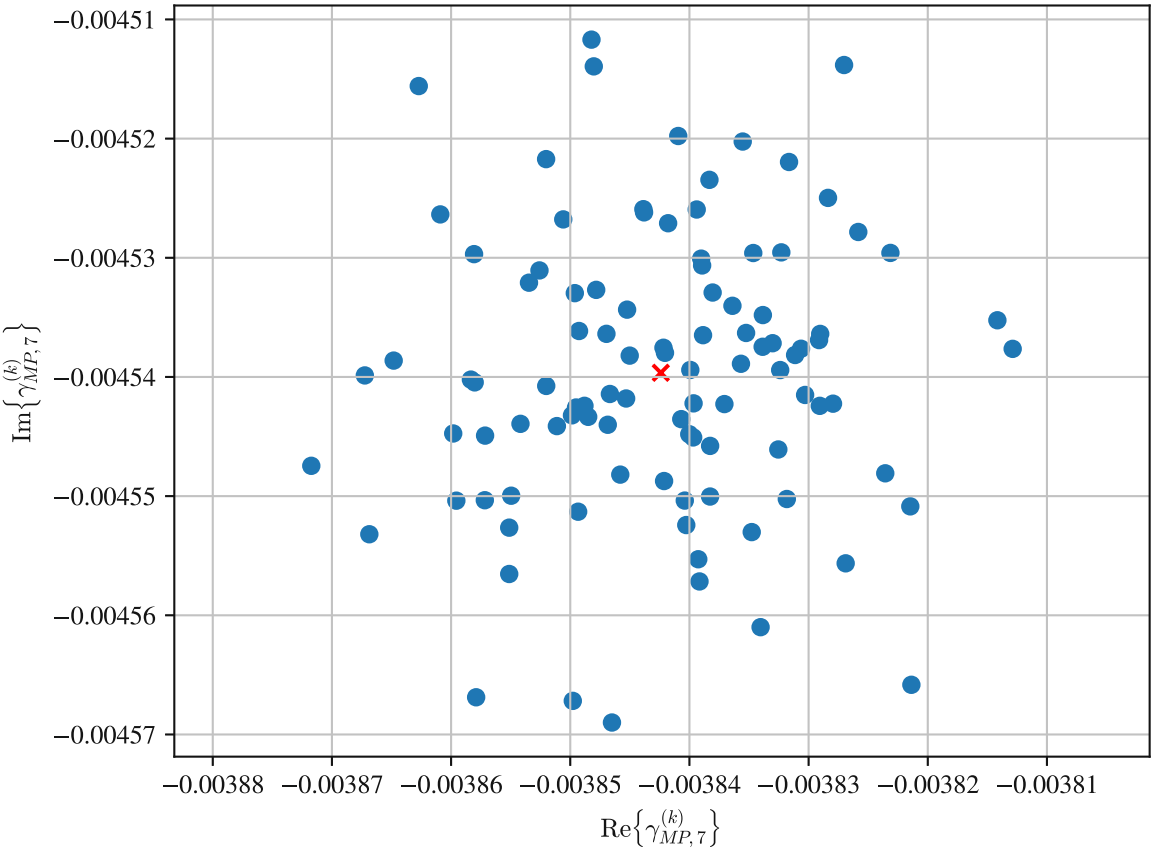

Figure 28: Multipath contribution to the measured RIS reflection at position $l = 7$: $\gamma^{(k)}_{MP,7}$. A zoomed in view of the bottom left point in Fig. 27.

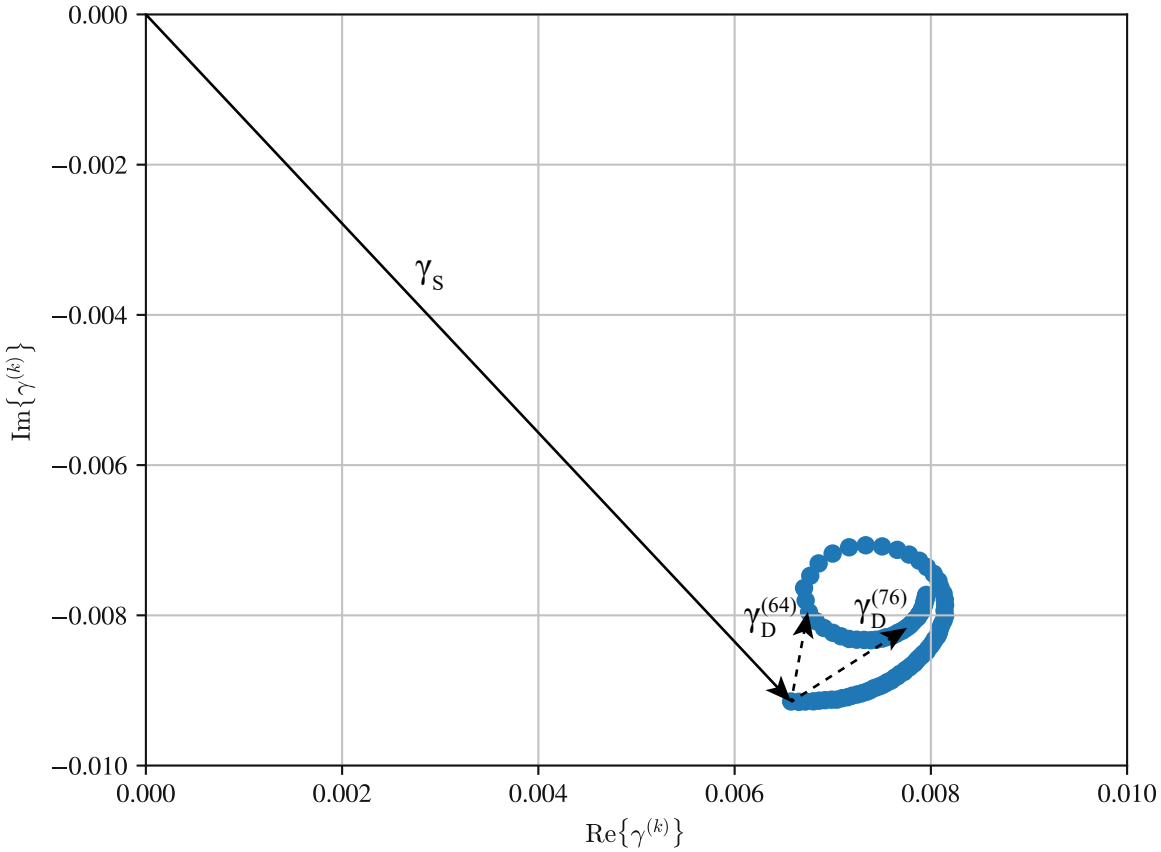

Figure 29: Reflection coefficient of the RIS $\gamma^{(k)}$.

This leads me finally to the description of the RIS by its reflection coefficient $\gamma^{(k)}$ displayed in Fig. 29. This figure combines the static and dynamic reflection coefficients computed in (33) and (27) respectively, into the total reflection of the RIS according to (17). Fig. 29 shows that the spiral responding to the changes in the RIS setting is placed in the fourth quadrant. Its location is likely the result of the remaining phase shifts from the probe antennas that were discarded in (11) and possibly some phase shift from the RIS itself.

This figure also shows that the RIS reflects little of the power of the incident signal towards the receiver. Much of the energy is lost to the environment, likely scattered and absorbed by the pyramid shaped absorbing elements surrounding the RIS. The power reflected due to the contribution of the dynamic component $\gamma_D(k)$ is almost a magnitude lower than the approximate mean of the spiral, visible from its distance from the offset.

3.2.3 Evaluation of the RIS Reflection Components over the Frequency

So far, the measurements have only been evaluated at a single frequency point. The channel model that has been proposed in Section 3.2 can also be used to evaluate the performance of the RIS over a frequency range. Therefore, in Fig. 31 we first analyze the magnitudes and in Fig. 31 the phases of reflection coefficients that were introduced in the previous sections. We consider the static reflection coefficient, γ_S, the dynamic reflection coefficients, $\gamma_D^{(k)}$ for a select number of RIS settings, the mean of the total reflection coefficient,

$$\overline{\gamma} = \mathop{\mathbb{E}}_{k} \left\{ \gamma^{(k)} \right\}, \tag{35}$$

as well as the reflection coefficient of a reference reflector, γ_{ref}^{A}, at frequencies between 5.3 GHz and 5.7 GHz. The reference reflector is a raw printed circuit board with a copper surface. It is approximately 155 mm × 155 mm large. As the metallic area of RIS is only 90 mm × 90 mm large, more power is received from the reference plate. To allow the comparison, I propose a scaling factor to account for the differing surface sizes and reduce the magnitude of γ_{ref}^{A} accordingly, with

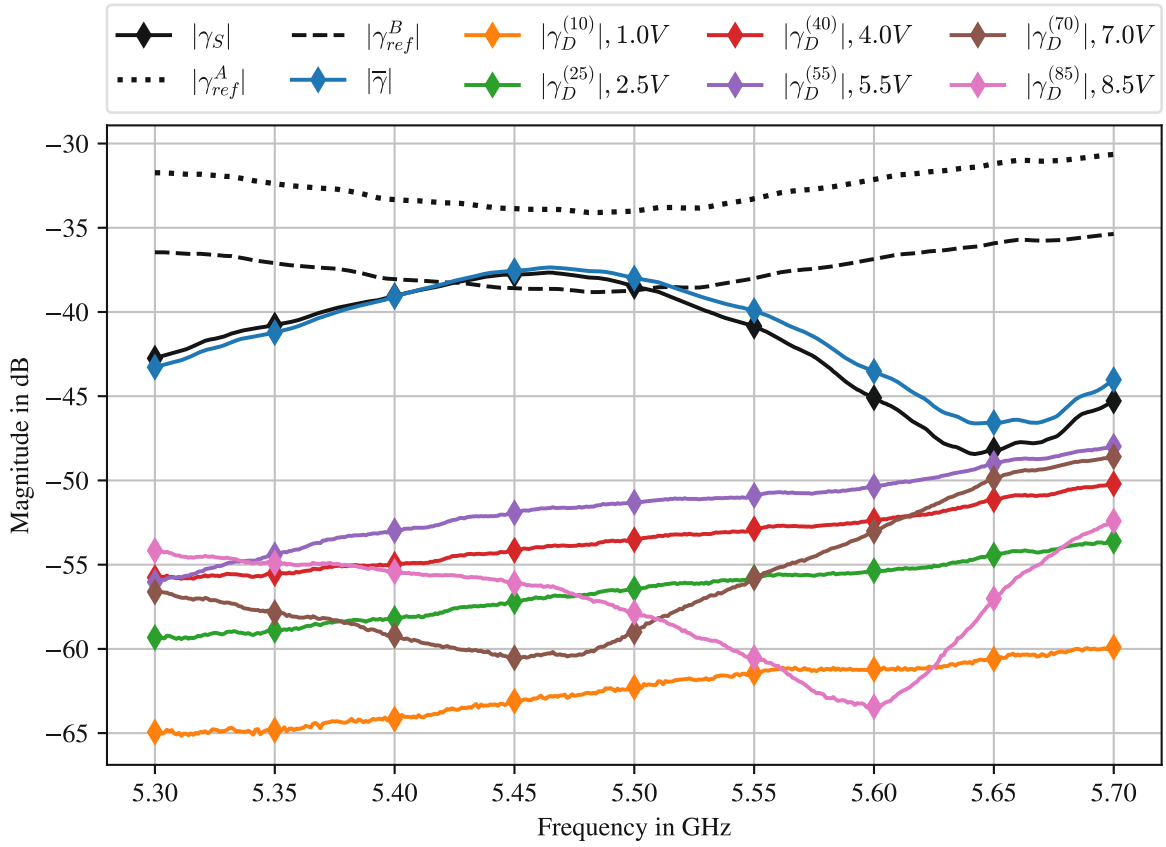

Figure 30: Magnitudes of the reflection coefficient components of the RIS: γ_S, $\gamma_D^{(k)}$, the average of the total reflection $\gamma^{(k)}$ denoted with $\overline{\gamma}$ and a reference reflector γ_{ref}^{A}, and the scaled version γ_{ref}^{B}, adjusted for the size difference to the RIS.

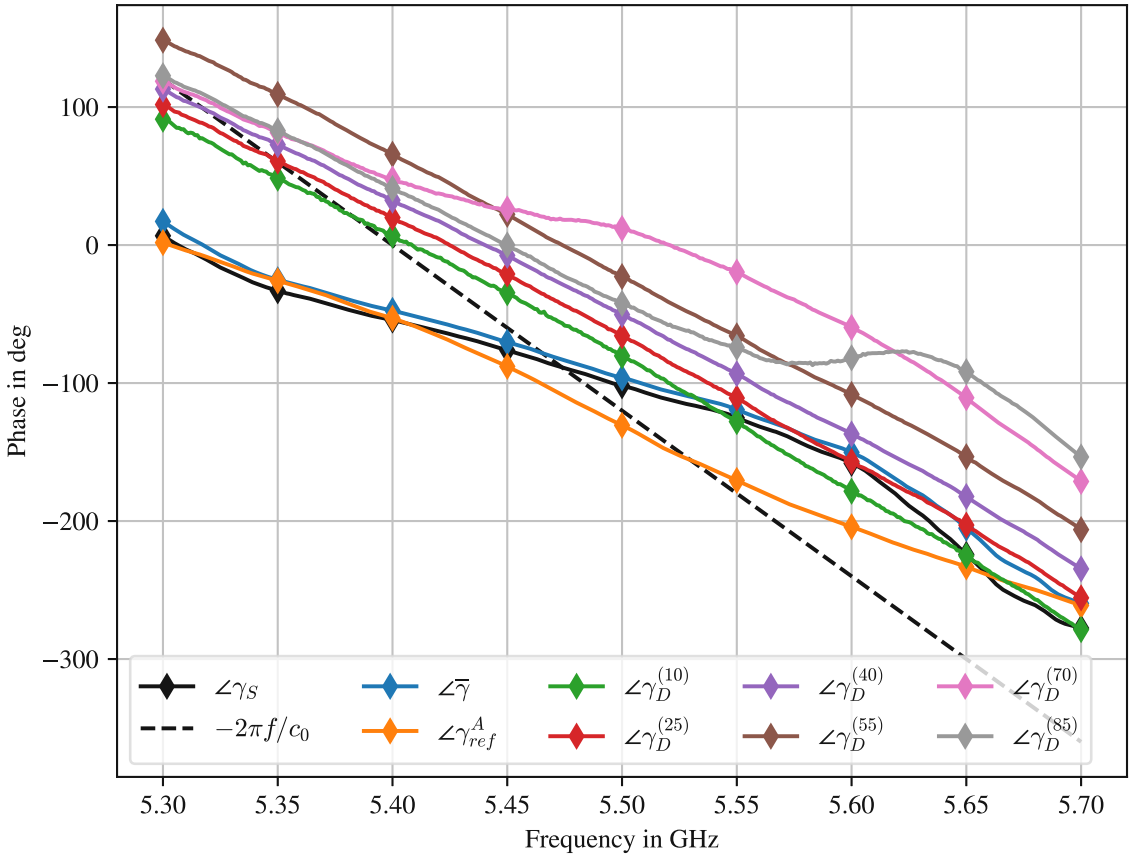

Figure 31: Phases of the reflection coefficient components of the RIS: γ_S, $\gamma_D^{(k)}$, the average of the total reflection $\gamma^{(k)}$ denoted with $\overline{\gamma}$ and a reference reflector γ^A_{ref}.

$$\left|\gamma^B_{ref}\right|_{dB} = \left|\gamma^A_{ref}\right|_{dB} - 10\log_{10}\left(155^2/90^2\right) \tag{36}$$

and plotted as $|\gamma^B_{ref}|$.

The static component displays a significantly higher gain compared to the dynamic components. Its magnitude appears similar to the adjusted reference reflector, if a few dB lower, but comparing the curve of the static reflection coefficient to the reference reflection, it becomes apparent that the RIS and the reference plate exhibit different behaviors over the plotted frequencies. One possible explanation is, that the differing sizes result in distinctive environments, with changed magnitudes for individual paths. But taking a closer look at some of the dynamic reflection components plotted in this figure, specifically $|\gamma_D^{(70)}|$ and $|\gamma_D^{(85)}|$, corresponding to the bias voltages 7 V and 8.5 V, respectively, could give a hint as to another factor influencing the magnitude of the RIS. We observe a dip at a specific frequency for each of these curves. For $|\gamma_D^{(70)}|$ it occurs at approximately 5.45 GHz and for $|\gamma_D^{(85)}|$ at 5.6 GHz. This indicates that there is likely some resonant structure in the RIS, which changes its resonant frequency in relation to the change in capacitance of the varactor diodes for different bias voltages. While the static component is defined as constant in relation to the bias voltages, its behavior may also be explained by some resonance occurring at 5.65 GHz. The actual, physical cause for this behavior is potentially related to the lengths of the control lines connecting to the

individual patches of the RIS, introducing an inductance into the design. The spacing between the patches then produce the capacitance required for this resonant circuit.

Next, we analyze the phase of the static and dynamic reflection components of the RIS as well as the phase of the reference plate shown in Fig. 31. Immediately, we can identify that the static and dynamic components exhibit different slopes within the plotted frequency range. Additionally, when comparing them to the $-2\pi f/c_0$ linear reference, neither of the two components displays this same slope. However, when comparing the phase of the static reflection component to that of the reference plate, we see that, while the two curves diverge between 5.4 GHz and 5.7 GHz, they exhibit approximately the same slope before this interval and seem to converge on the same phase at 5.7 GHz. We can also see that the largest difference in phase between the static component and the reference reflection occurs close to the frequency, where I previously theorized, regarding the magnitudes in Fig. 30, that the static component becomes resonant. A similar behavior can also be observed with the phases of the dynamic components $\gamma_D^{(70)}$ and $\gamma_D^{(85)}$ at their respective theorized resonant frequencies, reinforcing this interpretation.

3.3 Measurements with Nearfield and Farfield Positions

This chapter aims to investigate the effects of measuring in the nearfield and how the characterization of the RIS is subsequently affected. For this purpose I will begin with the differential reflection coefficient $\gamma_{d,l}^{(k)}$ introduced in (25). In Fig. 32, $\gamma_{d,l}^{(k)}$ is plotted for positions in the nearfield and farfield. Fig. 32 displays a spiral pattern consisting of a number of clusters. Each cluster consists of points with the same RIS setting k, but different position indices l. Compared to the farfield only case presented earlier in Fig. 20, the clusters in Fig. 32 exhibit a larger spread. Furthermore, the spread displays an elliptic or almost linear pattern. The clusters with RIS settings $k = 20$ and $k = 60$ are highlighted in orange in Fig. 32. We see that the cluster at $k = 20$ is partially obscured by the neighboring clusters, but is of approximately the same shape as the cluster at $k = 60$. We also see, when comparing $k = 20$ to $k = 60$, that the angles of the ellipses have changed. Due to the change of the spread of the clusters in Fig. 32 compared to the clusters of Fig. 20, the cluster centers have also shifted. These centers, marked by red crosses, are defined by the cluster mean over the position indices l, $\mathbb{E}_l\left\{\gamma_{d,l}^{(k)}\right\}$.

When considering the plotted clusters as a set of overlapping spirals, i.e., changing the position l alters the spiral's shape, it appears that there are three points, where the overlapping spirals appear to converge. The origin, a point in the top right of the figure and one further counter-clockwise along the spiral, at the bottom left. The points converge in the origin due to the definition of the differential reflection coefficient in (25).

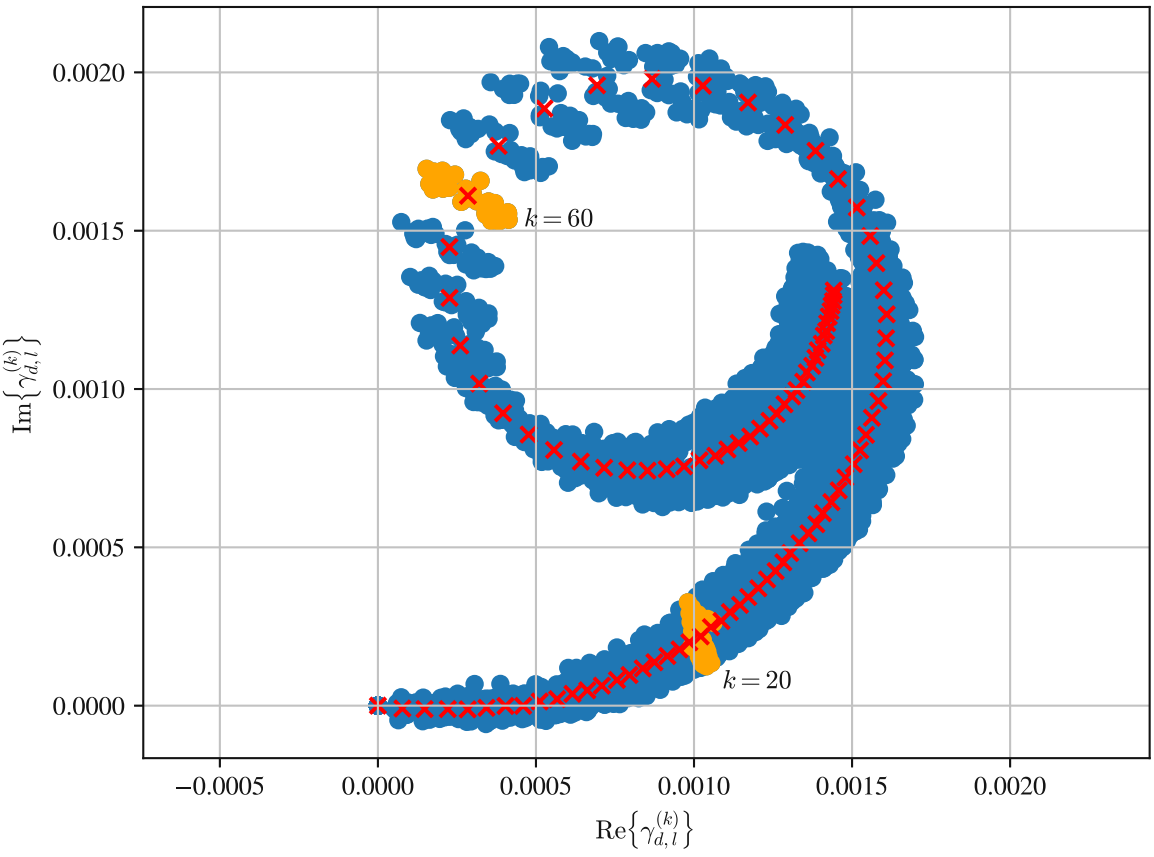

Figure 32: Differential RIS reflection coefficient $\gamma_{d,l}^{(k)}$ in the nearfield and farfield.

The origin is the reference point for the spiral. The other two convergence points exist, because the elliptically shaped collection of points aligns with the tangent of the spiral at these points, and disappears into the neighboring point clusters. Essentially appearing to contract significantly. This is confirmed, when the variance of the point clusters is compared with the power of the reflection coefficient in Fig. 33. This figure shows that there is a strong correlation between the spread of $\gamma_{d,l}^{(k)}$, described by its variance

$$\sigma_{\gamma,k}^2 = \underset{l}{\mathrm{Var}} \left\{ \gamma_{d,l}^{(k)} \right\}$$

initially defined in (28) and the power of the dynamic reflection coefficient $\gamma_D^{(k)}$ from (29),

$$p_k = \left| \gamma_D^{(k)} \right|^2 .$$

In fact, the definition of the correlation coefficient in (30), of the power of the dynamic component (29) and its variance over the positions l, (28), can be recalculated for this extended range of positions with

$$R_{\sigma_\gamma^2, p} = \frac{\mathrm{Cov}_k \left\{ \sigma_{\gamma,k}^2 \, p_k \right\}}{\sqrt{\mathrm{Var}_k \left\{ \sigma_{\gamma,k}^2 \right\} \mathrm{Var}_k \left\{ p_k \right\}}} = 0.97. \tag{37}$$

This result confirms the strong correlation visible in Fig. 33. Additionally, when comparing the values of the vertical axis of Fig. 33 with the one of the farfield only case in Fig. 23, we see that they are a factor 10 greater in the nearfield case compared to the farfield only one.

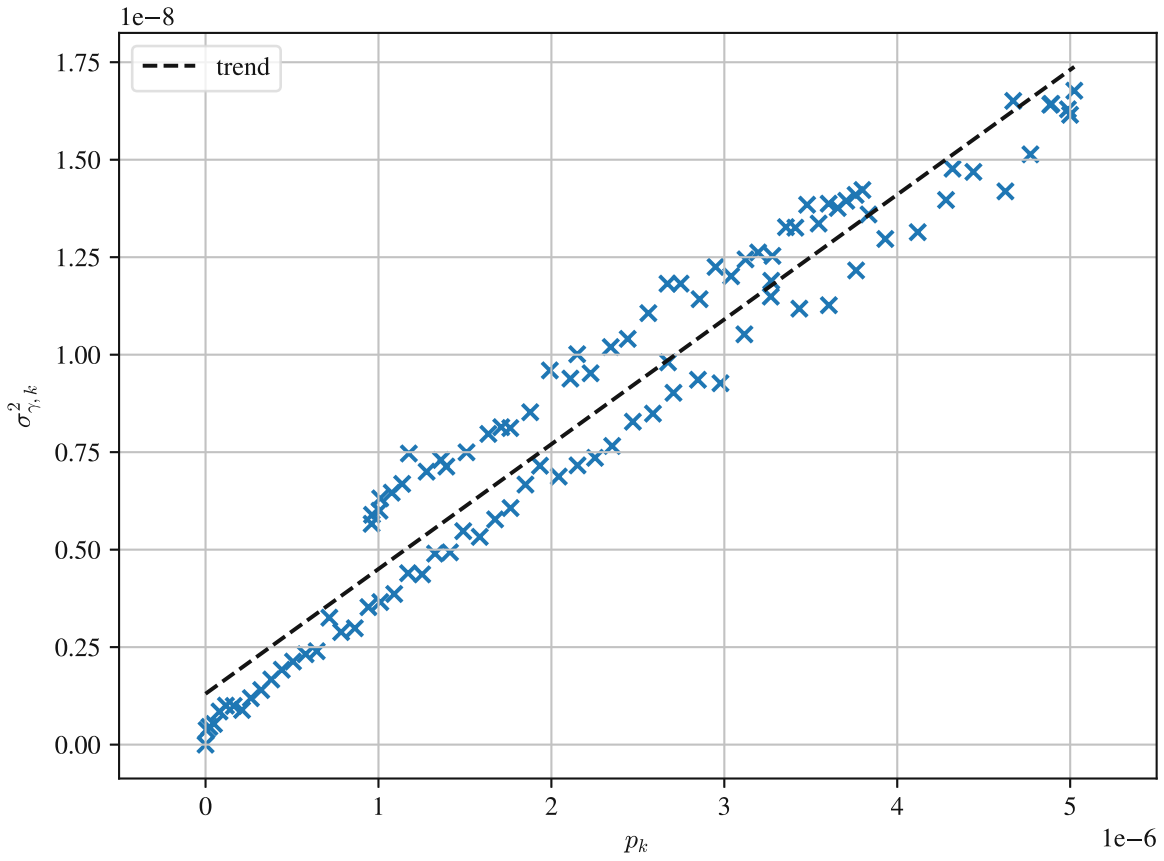

Figure 33: Variance of the scattering over all positions l, $\sigma^2_{\gamma,k} = \mathrm{Var}_l\left\{\gamma^{(k)}_{d,l}\right\} = \mathrm{Var}_l\left\{\gamma^{(k)}_{dMP,l}\right\}$, around the dynamic reflection component $\gamma^{(k)}_D$ in relation to the power of $\gamma^{(k)}_D$, p_k, for the same RIS setting k. This figure includes both farfield and nearfield positions.

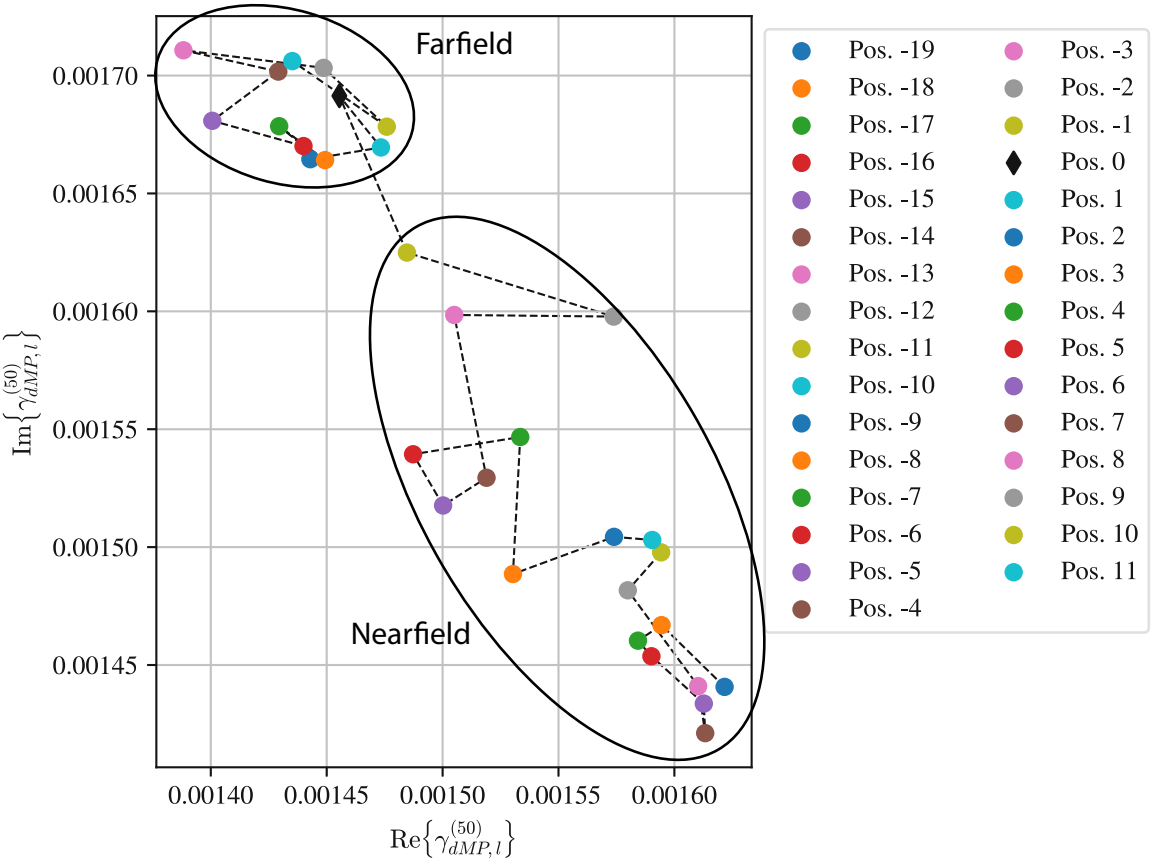

Figure 34: Multipath term of the differential RIS reflection, $\gamma^{(k)}_{dMP,l}$ at RIS setting k = 50, with the nearfield positions $l < 0$ included.

Fig. 34 zooms in on the point cluster around $k = 50$ of the differential spiral in Fig. 32. This cluster is located in the top right of the figure of the differential spiral. In the top left of Fig. 34, the positions that were previously shown in Fig. 21 are visible. The included nearfield positions extend the point cluster to the bottom right. An almost linear progression with increasing position index k is visible from the bottom right to the top left of the figure. Only for positions $l > -1$ do the points in Fig. 34 collapse into a more tightly packed cluster. This is the section of values corresponding to the farfield positions that was previously shown in Fig. 21. An additional cluster of points is visible in the bottom right of the figure, containing the first seven nearfield positions, i.e., the positions $l = -19 \ldots -12$. These values also appear to group together and seem to be more tightly packed than the farfield cluster in the upper left.

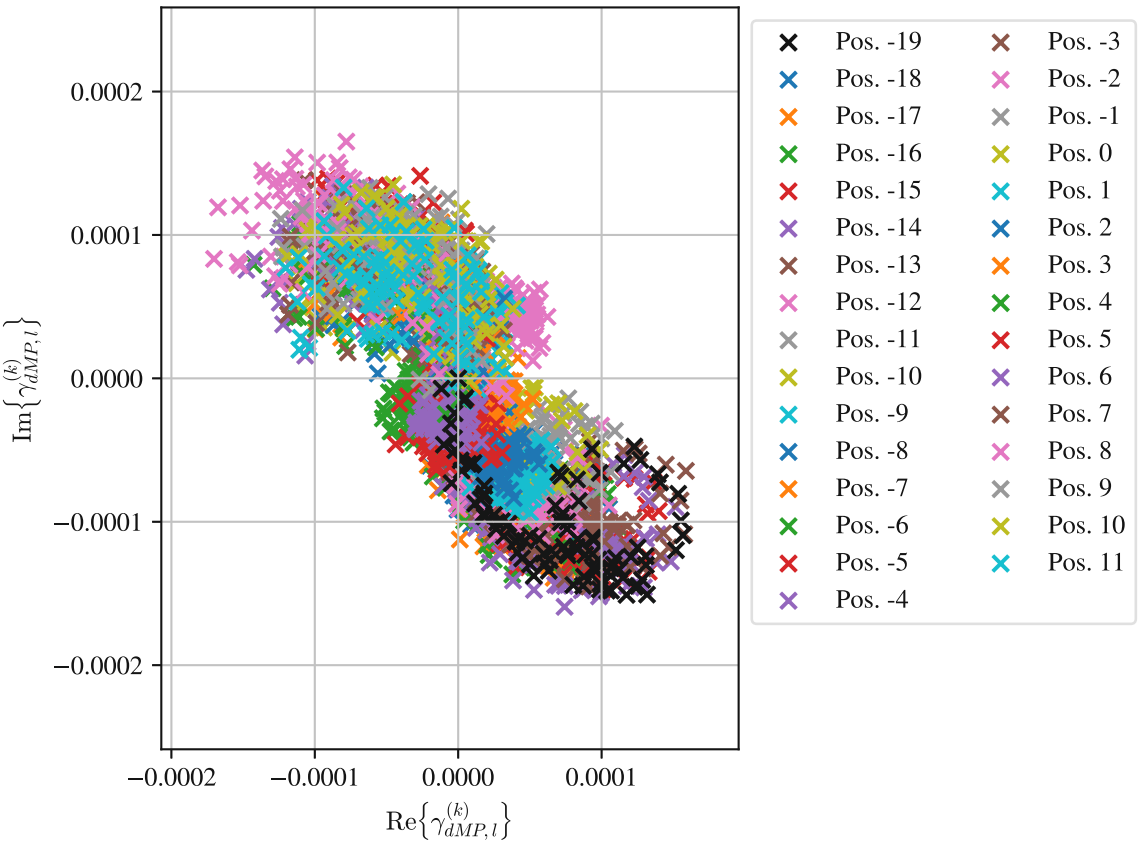

Figure 35: Differential multipath components $\gamma^{(k)}_{dMP,l}$ separated by position. Including nearfield positions $l < 0$.

Now, I once again make use of the definition of the dynamic component in (27), and the differential reflection coefficient from (25), to display only the differential scattering contribution $\gamma^{(k)}_{dMP,l}$ in Fig. 35. It appears that the points are displaying a correlation between the imaginary and real parts. The point clouds not fully overlapping indicates that there is some position dependency as well. However, this fact was also visible in Fig. 22, although not as clearly as in Fig. 35. Additionally, a RIS setting dependency is also implied by the shape of the distribution, similar to a noisy spiral. This is especially visible for the position $l = -19$, printed in black above the other points. The individual position cluster appear to be located either in the second or the fourth quadrant of the figure. Some more tightly packed cluster located close to the origin (the pink and green colored clusters) also appear in the first and third quadrants, but have little influence on the overall shape of the graph. This information, in conjunction with what is shown in Fig. 34, indicates that there must be some coupling effect between the RIS and the probe antennas. In the farfield, such a phenomenon could only result from secondary and later reflections involving the RIS. However, in the farfield, the added path length greatly diminishes the magnitude of the contributions of such scattering effects, making them quite unlikely.

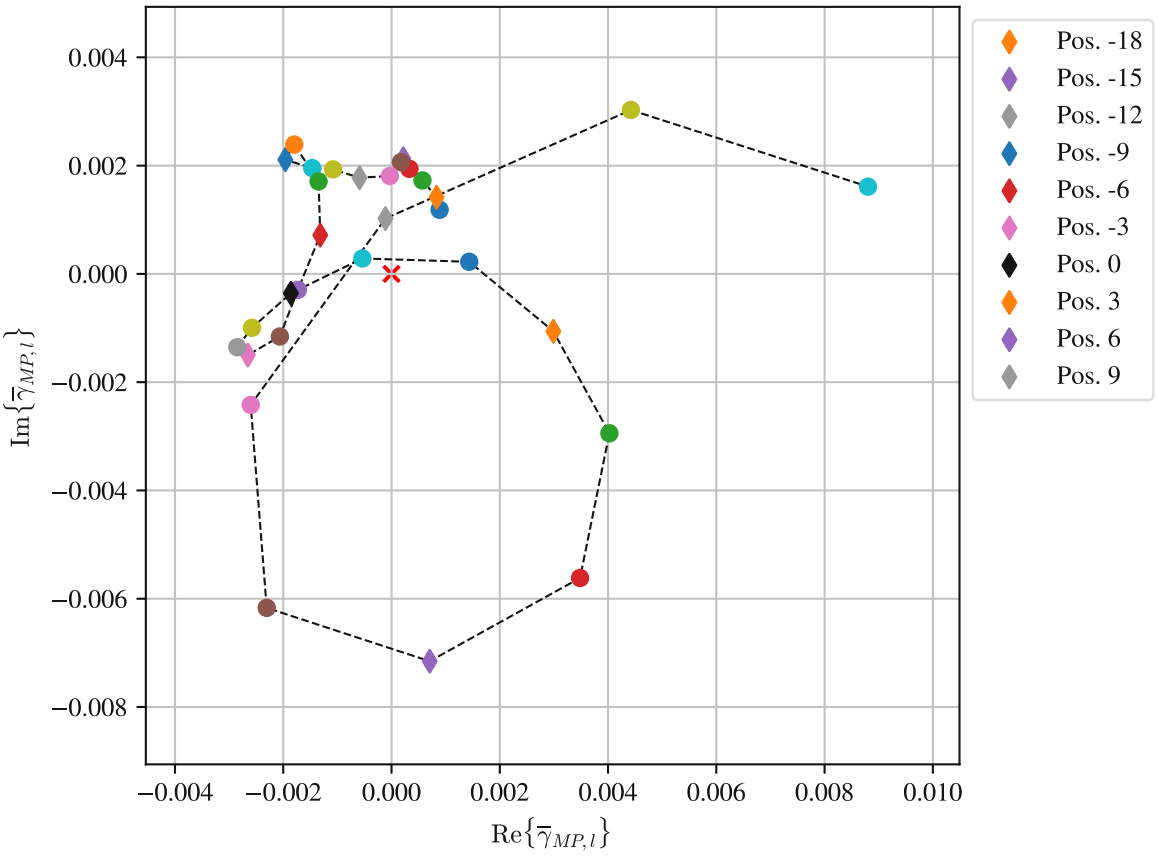

Figure 36: Mean values of the clusters of the position dependent multipath contribution, $\overline{\gamma}_{MP,l} = \mathbb{E}_k \left\{ \gamma_{MP,l}^{(k)} \right\}$, to the measured reflection of the RIS, including positions in the nearfield, i.e., $l < 0$.

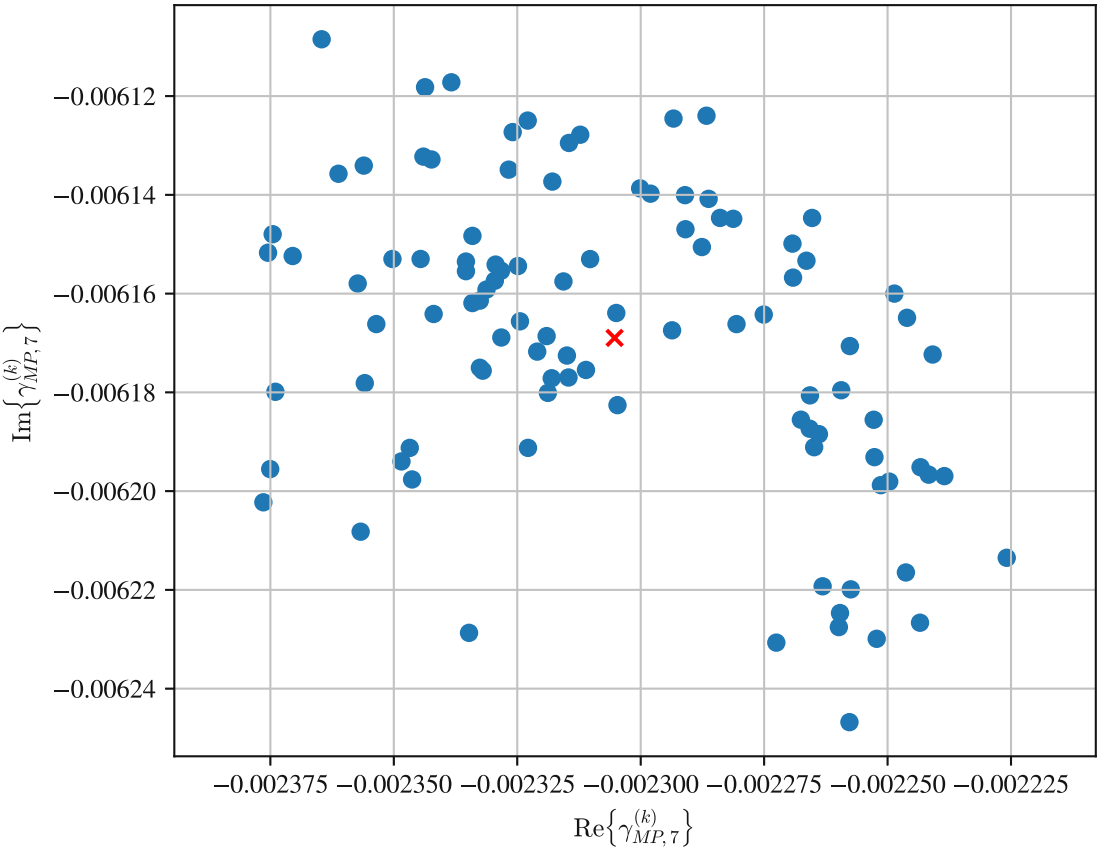

Figure 37: Multipath contribution $\gamma^{(k)}_{MP,l}$ at $l = 7$ calculated from a dataset including nearfield and farfield positions. This figure shows $\gamma^{(k)}_{MP,l}$ in relation to the RIS settings k. A zoomed in view of the bottom left point in Fig. 36.

Continuing with the multipath term $\gamma^{(k)}_{MP,l}$ in Fig. 36, extracted from (32). The new pattern differs greatly from the one in the farfield only case shown previously in Fig. 27, probably due to more effects contributing to this variable. Fig. 37 takes a closer look at position 7 ($l = 7$) in Fig. 36. The same position when only considering the farfield in Fig. 28 displays a seemingly random distribution of points. Fig. 37 appears to follow a half circle, with the left side displaying much greater spread than the right. The overall shape once again resembles a spiral. This change in shape likely results from an additional coupling effect, connecting positions and RIS settings, in the nearfield. However, as position 7 is not a nearfield position, one may think that the shape should be similar to the farfield only case in Fig. 28. This is not the case, as the calculation of this variable from (32) depends on the RIS reflection coefficient $\gamma^{(k)}$. This dependency changes the shape of $\gamma^{(k)}_{MP,l}$ due to the effects of the nearfield positions influencing $\gamma^{(k)}$. Finally, the cluster average is marked by the red cross. Compared to Fig. 27, the mean of the displayed points does not allow us to make the assumption that the points are centered on it.

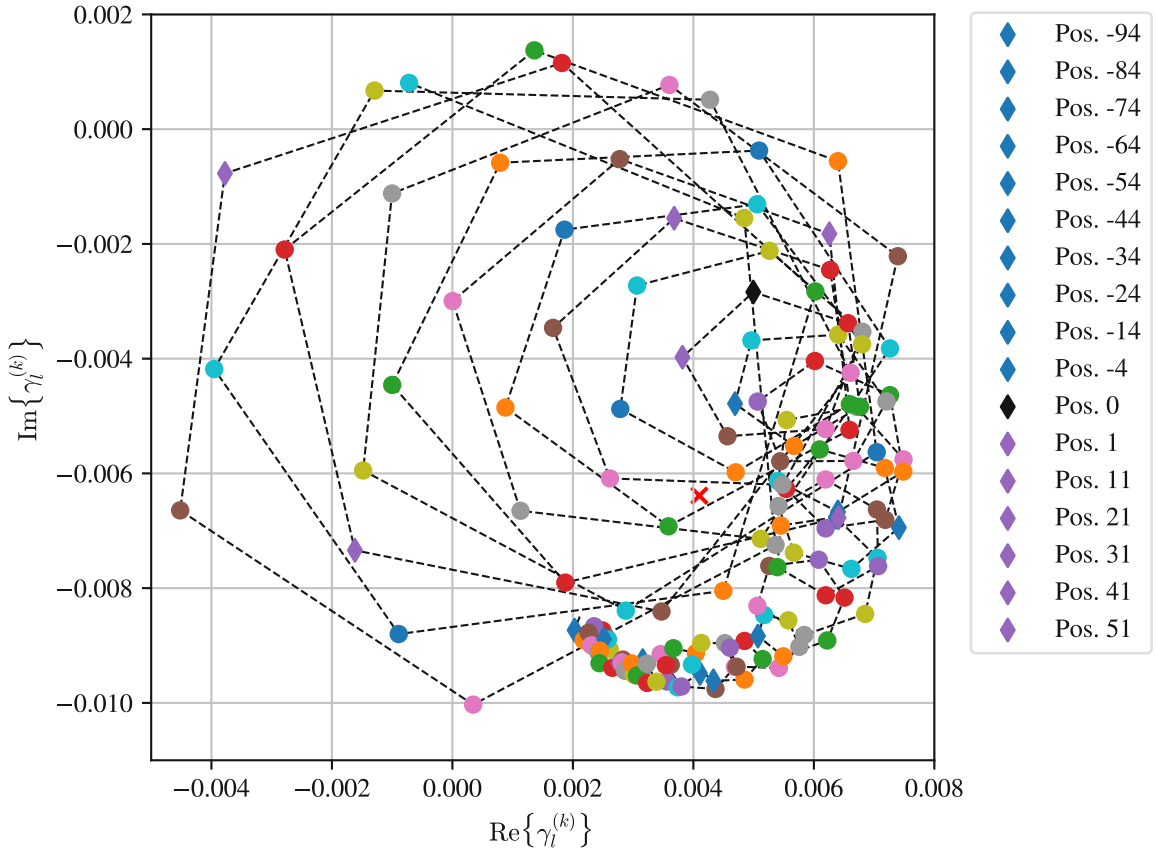

Figure 38: $\gamma_l^{(k)}$ for $k = 0$ including positions in the nearfield, determined according to (32).

Let us now analyze the behavior of the position dependent reflection coefficient $\gamma_l^{(k)}$, defined in (32) for a single RIS setting $k = 0$ at the nearfield and farfield positions. Fig. 38 displays the position dependent reflection coefficient $\gamma_l^{(k)}$, determined using the data from measurement campaign C. The nearfield positions are denoted by the position index $l < 0$. The farfield positions ($l \geq 0$) in Fig. 38 and in the farfield only case in Fig. 24 appear identical. However, the nearfield positions have added a semi-circle like shape at the bottom right of the figure. These additional nearfield points do not follow the same pattern as the farfield positions. This results in a shifted mean, demarcated with a red cross in Fig. 38, compared to the mean in Fig. 24, which is also marked by a red cross. In the farfield only case of Fig. 24, the mean was located at approximately $(3 - j4) \cdot 10^{-3}$, with j being the imaginary number $j = \sqrt{-1}$. In Fig. 38, the average is now approximately located at $(4 - j6) \cdot 10^{-3}$.

We also see, that the circles indicated by the black dashed lines become smaller as the position index decreases. This behavior continues the trend we have seen for the farfield positions in both figures, Fig. 24 and Fig. 38.

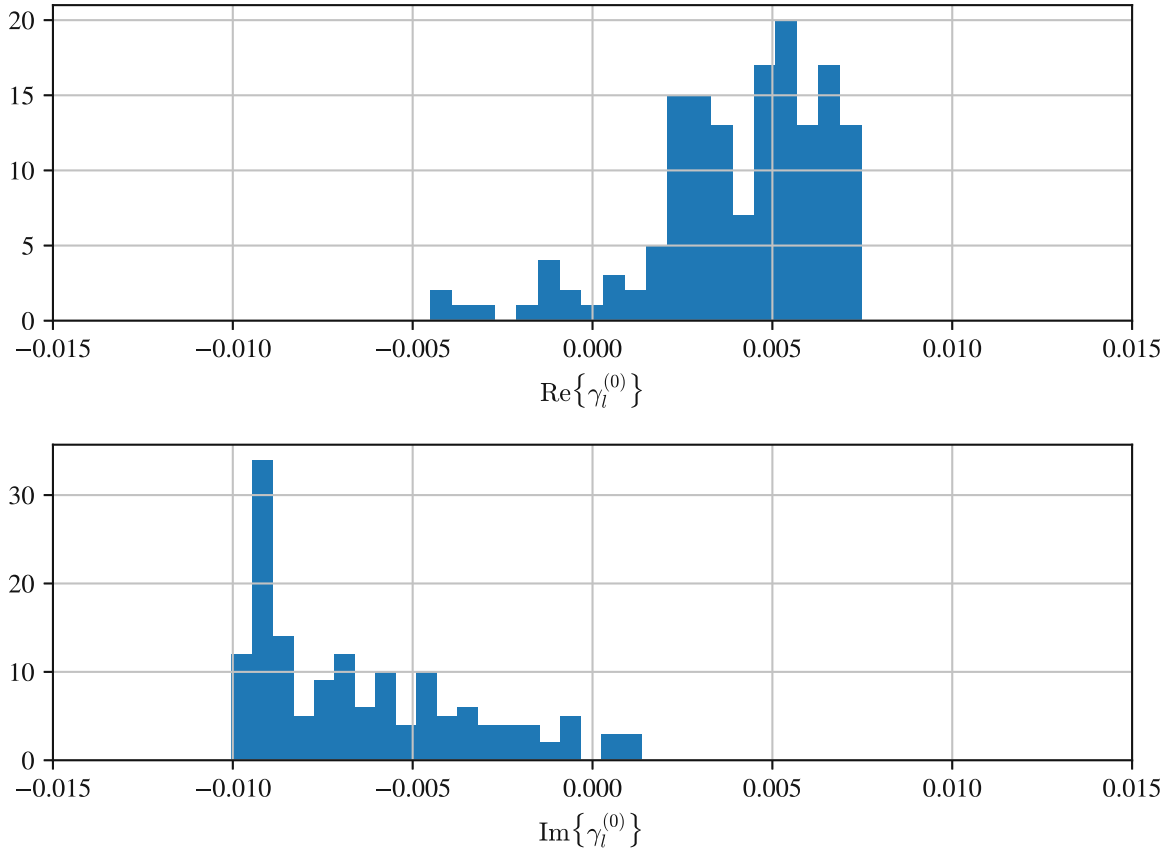

Figure 39: Distribution of the real and imaginary part of $\gamma_l^{(k)}$ for $k = 0$ including positions in the nearfield.

Next, we will investigate the distribution of values of the real and imaginary parts of $\gamma_l^{(k)}$ and compare the nearfield and farfield case in Fig. 39 to the farfield only case in Fig. 26. Fig. 39 shows an increased number of values with a higher deviation from the origin compared to Fig. 26. This is visible in the value range of approximately $2.5 \cdot 10^{-3}$ to $7.5 \cdot 10^{-3}$ of the histogram of the real part, $\mathrm{Re}\left\{\gamma_l^{(k)}\right\}$ in both figures. In contrast, the values of the imaginary part appear to concentrate around $-9 \cdot 10^{-3}$ in Fig. 39. In Fig. 26 the imaginary part, $\mathrm{Im}\left\{\gamma_l^{(k)}\right\}$ displayed a greater spread in its value distribution and a lower density of the respective values. The difference to Fig. 39 is mainly due to the larger number of positions in the nearfield affecting the results of the combined case with nearfield and farfield positions in Fig. 39, compared to the fewer farfield positions.

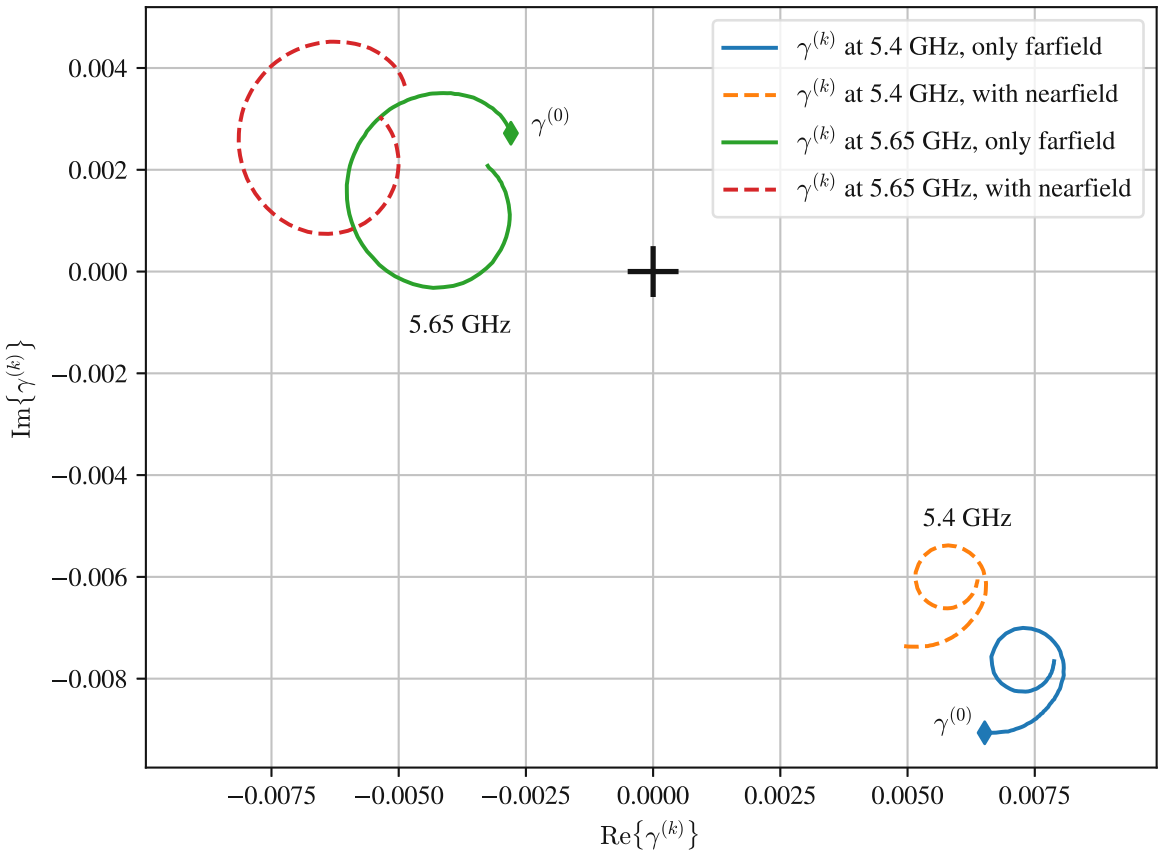

Figure 40: Reflection coefficient $\gamma^{(k)}$ at 5.4 GHz and 5.65 GHz, calculated from (i) farfield positions, and (ii) farfield and nearfield positions.

Finally, in Fig. 40 the resulting RIS reflection coefficient $\gamma^{(k)}$ is displayed at the frequencies 5.4 GHz and 5.65 GHz. The solid lines in blue and green in Fig. 40 correspond to the farfield only positions and the dotted lines include the nearfield positions as well. The 5.4 GHz spirals are located in the bottom right of the figure and the 5.65 GHz ones are positioned in the top left of the figure. When directly comparing the spirals of the two frequencies, we see that they differ in shape, location and magnitude. The spread or diameter of the 5.65 GHz spirals is almost twice as large as the spread of the 5.4 GHz spirals. By spread I refer to the maximum distance between any two points of the spiral. When considering a circle, i.e., the ideal case for the RIS for its phase distribution, the maximum distance between points is the diameter of the circle. The location of the 5.65 GHz spirals is much closer to the origin compared to the 5.4 GHz spirals, indicating a small static component of the reflection coefficient $\gamma^{(k)}$ of the RIS. We also see that, while the 5.4 GHz and 5.65 GHz lines have a spiral shape, the 5.4 GHz seems to exhibit a rotation larger than 360°, while the 5.65 GHz spiral appears almost as an ellipse. When considering the varactor diode based design of the RIS, a shape as shown at 5.4 GHz seems implausible as that phase shift is not possible to achieve with only a capacitance. This phenomenon is explained by resonances occurring due to the structure of the RIS. The bias voltage lines and vias introduce an inductance and the spacing between the patches and ground lines and ground plane, in addition to the varactor diodes, the capacitance.

If we now take a look at the locations of the spirals that include only the farfield

positions compared to the ones including the nearfield positions, we observe that they are offset from each other. The 5.65 GHz nearfield spiral is located further away from the origin than the farfield only case. This behavior is flipped for the spirals at 5.4 GHz. Both, however, share a relation between the nearfield and farfield spirals. They appear to be positioned on a straight line spanned from the origin to the respective outermost spiral. This is due to the difference in the static reflection components γ_S. We have seen from Fig. 32, that the dynamic component is of a slightly different shape, when including the nearfield positions, compared to Fig. 20 with only farfield positions. But Fig. 38 has shown that there is a large scale difference, when the nearfield positions are considered as well. The influence of the nearfield positions therefore contributes mainly to the shift in the static component, explaining the differences shown in Fig. 40.

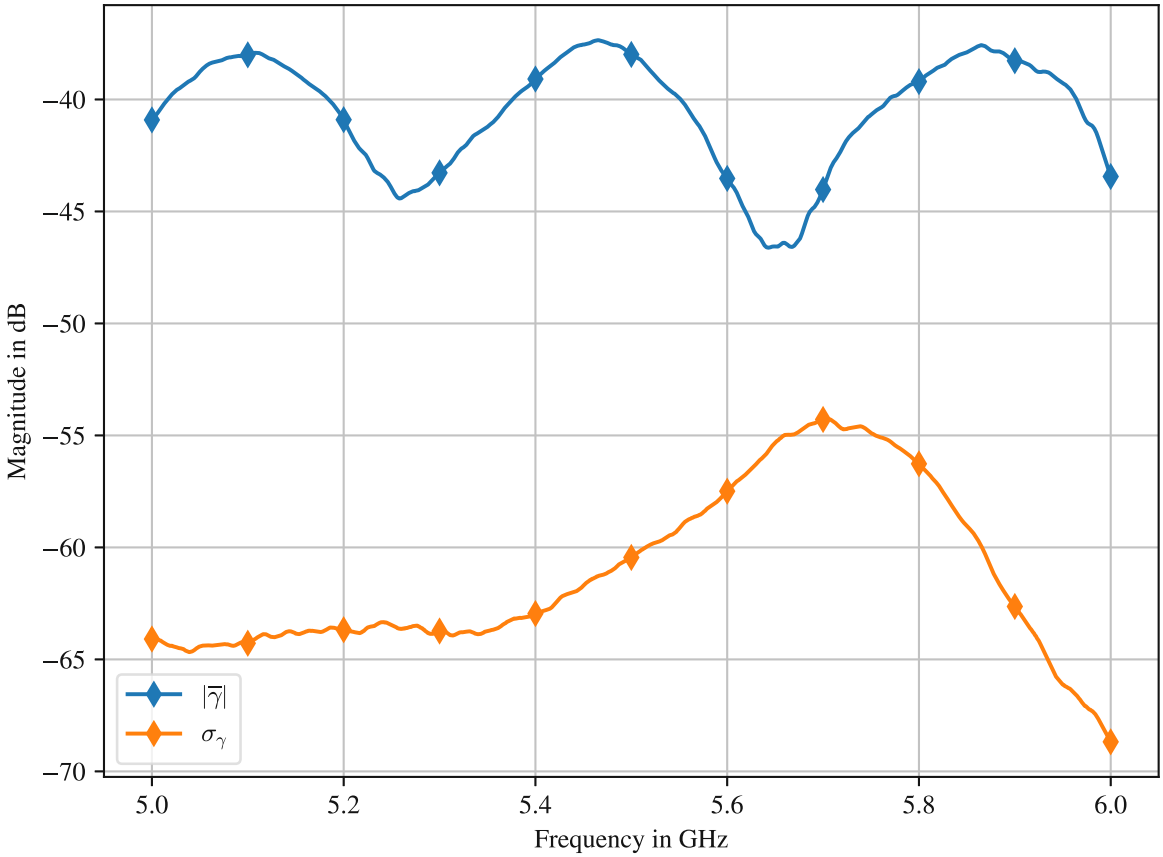

Figure 41: Magnitude of the spiral mean and standard deviation σ_γ of the spiral between 5 GHz and 6 GHz.

3.4 RIS Performance Indicators

After the measurements have been explored we investigate some basic parameters that allow us to describe the performance of the RIS. For this purpose we will analyze the behavior of the RIS over frequency and over its RIS settings, indicated by the index k introduced above. 5.65 GHz in particular is of interest. According to the results analyzed in Fig. 30, the magnitude of its static reflection coefficient γ_S of the RIS is lowest. A second frequency that will be used for comparison is 5.4 GHz. It has been used in the evaluation of the RIS performance in previous sections but does not display any special characteristics in Fig. 30. The result shown in Fig. 40 further supports this choice of frequencies. It was shown that the reflection coefficient $\gamma^{(k)}$ of the RIS has a greater magnitude spread (or radius) at 5.65 GHz compared to the spiral at 5.4 GHz and appears approximately as a circle.

For the purpose of processing the measured data the offset of the reflection coefficient of the RIS was defined in (18) and (19) as the static reflection component γ_S by choosing $\gamma_D^{(0)} = 0$. While this is useful for the separation of the channel contributions, i.e., the RIS reflection and environmental scattering, the mean of $\gamma^{(k)}$ over k,

$$\overline{\gamma} = \mathop{\mathbb{E}}_{k} \left\{ \gamma^{(k)} \right\},$$

is more convenient for the description of the performance of the RIS. The centralized offset of the RIS reflection coefficient, described by the mean, can be used to estimate the magnitude of the specular reflection of the RIS. The effective radius of the reflection coefficient is defined as the standard deviation,

$$\sigma_\gamma = \underset{k}{\mathrm{Std}}\left\{\gamma^{(k)}\right\} = \sqrt{\underset{k}{\mathrm{Var}}\left\{\gamma^{(k)}\right\}}. \tag{38}$$

It estimates the magnitude of the dynamic reflection components relative to the mean. These parameters are shown in Fig. 41. The figure displays a maximum of σ_γ at approximately 5.7 GHz and two minima of $|\overline{\gamma}|$ at approximately 5.25 GHz and 5.65 GHz. The minima of $|\overline{\gamma}|$ and the maximum of σ_γ are of interest. The minima indicate a lower magnitude of the specular reflection and the maximum of σ_γ describes the frequency at which we can expect a higher magnitude of the anomalous reflection, i.e., the reflection towards a target direction with an angle differing from the incident angle. We can expect the best performance, when a maximum of σ_γ and a minimum of $|\overline{\gamma}|$ occur at the same frequency.

At the chosen frequency, 5.65 GHz, σ_γ is approximately 1 dB below the maximum at 5.7 GHz. 5.65 GHz was selected for this investigation rather than 5.7 GHz, to minimize $|\overline{\gamma}|$ before maximizing σ_γ. The difference in magnitude between σ_γ and $|\overline{\gamma}|$ at 5.65 GHz is about 8 dB. At 5.7 dB this difference is close to 10 dB. Over the entire frequency range we find the maximum difference at 5.1 GHz with approximately 26 dB and the minimum difference at the chosen frequency 5.65 GHz.

By comparison, should 5.4 GHz be chosen instead, with $|\overline{\gamma}|$ close to a maximum and σ_γ about 8 dB lower than the maximum at 5.7 GHz, we can expect that most of the power at this frequency will be reflected in the direction of the specular reflection.

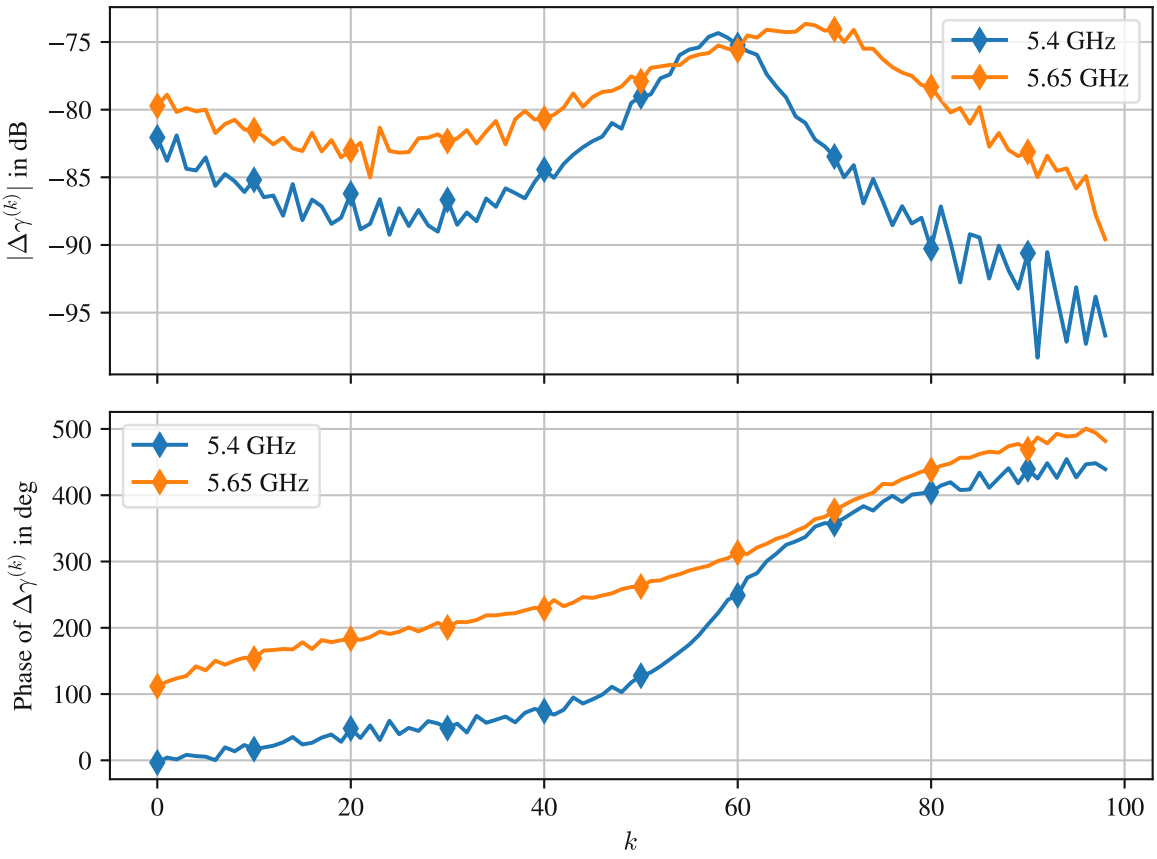

Figure 42: Difference description of the magnitude and phase of the RIS reflection coefficient over the RIS setting k.

Next, we take a closer look at the differences between the RIS settings k with

$$\Delta\gamma^{(k)} = \gamma^{(k+1)} - \gamma^{(k)} = \gamma_D^{(k+1)} - \gamma_D^{(k)} \tag{39}$$

where k is the RIS setting index. The magnitude and phase of $\Delta\gamma^{(k)}$, indicate at which settings k, and therefore at which bias voltages resonances occur for the investigated frequencies. They are plotted in Fig. 42 over k for 5.4 GHz and 5.65 GHz. At around $k = 60$ we can see two peaks in the magnitude plot, the peak at 5.4 GHz occurs slightly before $k = 60$ and the peak at 5.65 GHz a few steps after. Both peaks have approximately the same magnitude. However, the values of the magnitude at 5.65 GHz are higher on average than at 5.4 GHz. This is explained by the spiral at 5.65 GHz having a larger diameter than the spiral at 5.4 GHz and therefore the differences between neighboring settings k being larger. In the phase plot we see that both frequencies have generally the same slope, but at the k where a peak occurs in the magnitude plot, we see a steeper incline in the phase plot at 5.4 GHz compared to 5.65 GHz. this indicates not only a large magnitude difference between neighboring k but also a larger phase change. This behavior is directly related to the shapes of the spirals depicted in Fig. 40, with the spiral at 5.65 GHz being closer to a circle and therefore displaying only a small change in the slope of the phase in Fig. 42 compared to the spiral shape visible at 5.4 GHz.

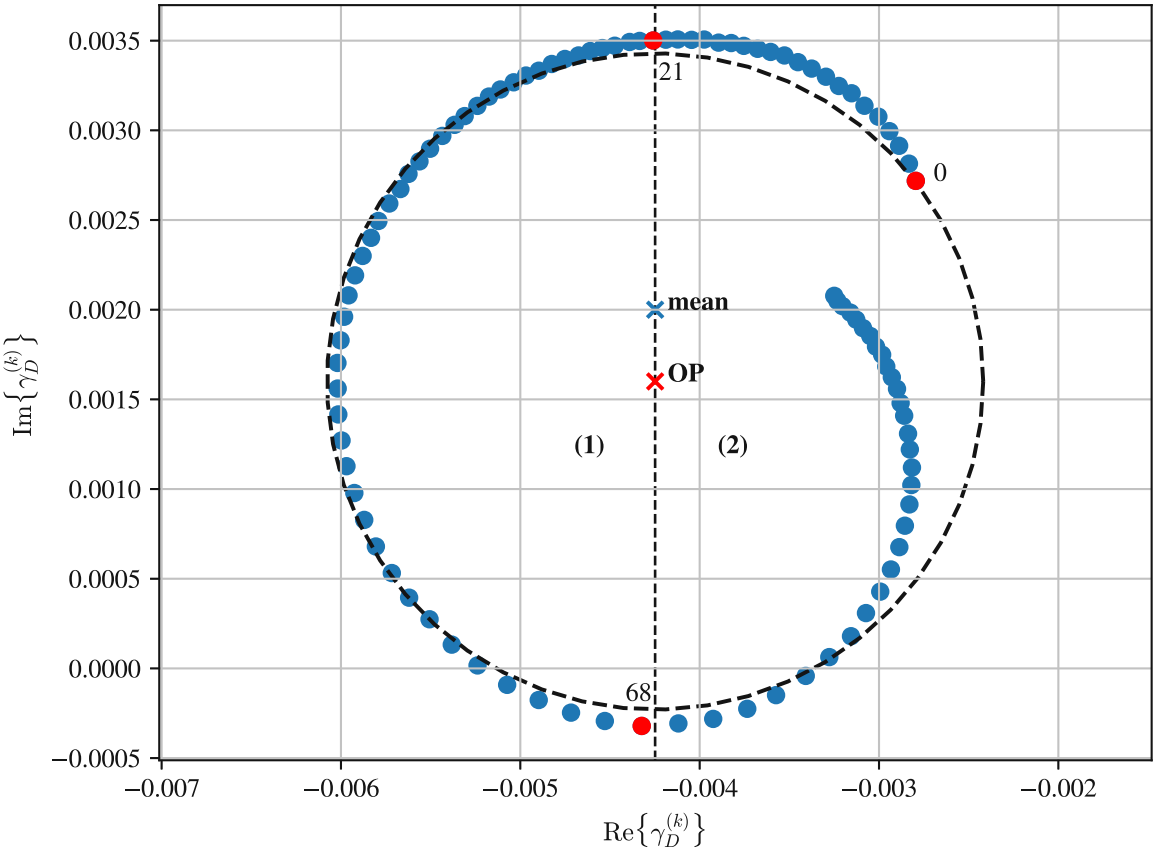

Figure 43: Example of available regions, denoted as (1) and (2) for a phase difference of approximately 180° between the reflection coefficients with RIS setting $k = 21$ and $k = 68$, derived from a manually chosen operating point (OP).

To be able to use beamforming algorithms [18], [19] with the acquired parameters, we need to choose an operating point. In Fig. 43 the dynamic component $\gamma_D^{(k)}$ at 5.65 GHz is shown, where each blue point corresponds to a RIS setting k and the blue cross is the mean $\overline{\gamma}$ at this frequency. We can immediately see that the mean is not ideal for this purpose, as it is not centered and results in significant differences in magnitude between RIS settings, i.e., $\left|\overline{\gamma} - \gamma^{(k)}\right|$ would have a large variance. Instead we need to choose an operating point (OP) so that we can redefine the total reflection coefficient from (32) as

$$\gamma^{(k)} = \gamma_{OP} + \tilde{\gamma}_D^{(k)}, \tag{40}$$

where γ_{OP} represents the chosen operating point and $\tilde{\gamma}_D$ is the shifted version of γ_D with

$$\tilde{\gamma}_D^{(k)} = \gamma_D^{(k)} + \gamma_S - \gamma_{OP}. \tag{41}$$

In this example, γ_{OP} was chosen with the same real part as the mean, $\overline{\gamma}$, but with the imaginary part

$$\mathrm{Im}\{\gamma_{OP}\} = \mathrm{Im}\left\{\frac{\gamma^{(21)} + \gamma^{(68)}}{2}\right\}, \tag{42}$$

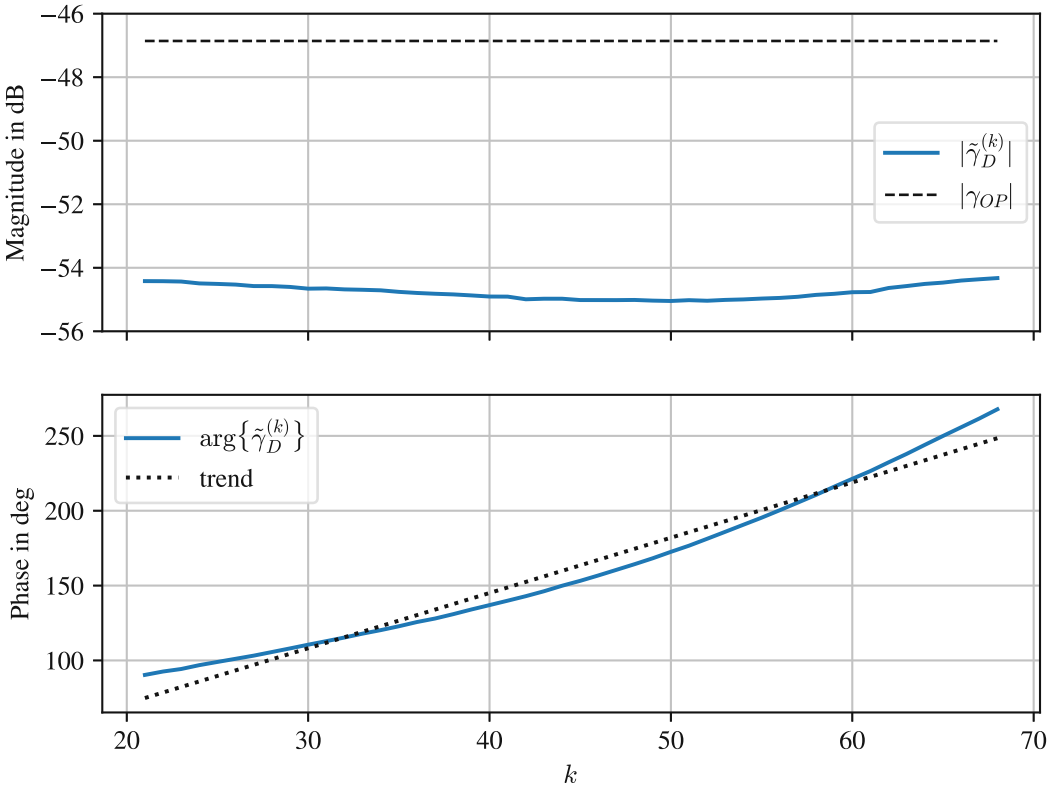

Figure 44: Parameter set derived from Fig. 43 of region (1) in magnitude and phase. The dashed line represents the magnitude of the operating point.

s.t., the operating point is geometrically centered for this spiral. Following this choice of the operating point, we can now select the left side of the plot, denoted with (1), as our set of available reflection coefficients. This side has been chosen as its pattern is close to a circle (shown as a dashed line). Additionally, with this set of points, between $k = 21$ and $k = 68$, we have a maximum possible phase difference of 177.45°. The operating point has therefore replaced the static component γ_S as the fixed reference for the dynamic contribution to the total reflection coefficient $\gamma^{(k)}$. The static reflection coefficient can still be reobtained from (40) with RIS setting $k = 0$.

Following this definition, we can now determine the performance of the reflection coefficient with respect to the operating point. The resulting magnitude and phase over the selected range of k is shown in Fig. 44. The upper plot shows that, as a result of the chosen operating point, there is only little variation in magnitude with values between −54 dB and approximately −55 dB. For comparison, the dashed black line in this plot represents the magnitude at the operating point, $|\gamma_{OP}|$, which is about 7 dB to 8 dB larger than the magnitude of the dynamic component, $|\tilde{\gamma}_D^{(k)}|$ depicted as the solid blue line. The bottom figure shows the phase of $|\tilde{\gamma}_D^{(k)}|$ in relation to the RIS setting k. It appears approximately linear with a stronger change in slope around $k = 50$, where we also observe a minimum in the magnitude plot.

3.4.1 Comparison of Models

The question now arises, how these results compare to channel models of RISs. We will illuminate the similarities and differences to two such models [21], [22]. In this section the notation of [21], [22] will be used, instead of the notation that was introduced with Section 3.2, i.e., upper case letters no longer denote random variables. Both authors describe the channel with

$$\mathbf{H} = \mathbf{S}_{RT} + \mathbf{S}_{RI}\boldsymbol{\Theta}\mathbf{S}_{IT}, \tag{43}$$

where $\mathbf{H}$ represents the channel matrix of size $N_R \times N_T$ with N_R receive and N_T transmit antennas. $\mathbf{S}_{RT}$ is the $N_R \times N_T$ scattering parameter matrix describing the mutual coupling between the transmit and receive antenna. The $N_R \times N_I$ paths from the RIS, denoted with subscript I, and the receive antennas, are described by the scattering matrix $\mathbf{S}_{RI}$. The $N_I \times N_T$ paths from the transmit antenna to the RIS are defined in the scattering matrix $\mathbf{S}_{IT}$. The $N_I \times N_I$ matrix $\boldsymbol{\Theta}$ describes the reflection coefficient from the N_I RIS elements.

In [21] the scattering matrices are related to the impedance matrices using a linear transformation with

$$\mathbf{S}_{RT} = \frac{\mathbf{Z}_{RT}}{2Z_0}, \quad \mathbf{S}_{RI} = \frac{\mathbf{Z}_{RI}}{2Z_0}, \quad \mathbf{S}_{IT} = \frac{\mathbf{Z}_{IT}}{2Z_0}. \tag{44}$$

Where $\mathbf{Z}_{RT}$ is the equivalent impedance matrix of the direct path between the receive and transmit antennas, $\mathbf{Z}_{RI}$ the equivalent impedance matrix between the receive antennas and the RIS elements and $\mathbf{Z}_{IT}$ is the equivalent impedance matrix between the transmit antennas and the RIS elements. Z_0 is the reference impedance, which is assumed to be equal at all ports. In [22], however, the scattering matrix of the direct path is described as

$$\mathbf{S}_{RT} = \frac{1}{2Z_0}\left(\mathbf{Z}_{RT} - \frac{1}{2Z_0}\mathbf{Z}_{RI}\mathbf{Z}_{IT}\right), \tag{45}$$

where $\mathbf{Z}_{RT}$ denotes the impedance matrix of the direct path between receive and transmit antennas and $\mathbf{Z}_{RI}$, the impedance matrix between RIS and receive antenna and $\mathbf{Z}_{IT}$ the impedance matrix between RIS and transmit antenna. The relations between the other scattering and impedance matrices, $\mathbf{S}_{RI}$ and $\mathbf{Z}_{RI}$, $\mathbf{S}_{IT}$ and $\mathbf{Z}_{IT}$, remain the same. Without mutual coupling, i.e., $\mathbf{Z}_{RT} = \mathbf{0}\,\Omega$ between the transmit and receive antennas, the model in (43) differs for the two cases, with

$$\begin{aligned} &\text{Nossek:} && \mathbf{S}_{RI}\left(\boldsymbol{\Theta} - \mathbf{I}_{N_I}\right)\mathbf{S}_{IT}, \\ &\text{Shen:} && \mathbf{S}_{RI}\boldsymbol{\Theta}\mathbf{S}_{IT}, \end{aligned}$$

where $\mathbf{I}_{N_I}$ is the identity matrix of size $N_I \times N_I$. In the following paragraph we consider the results attained from the measurements and attempt to compare them to the two channel models. For the measurements we used one receive antenna and one transmit antenna resulting in the simple case of $N_R = N_T = 1$. Due to the chosen RIS settings, as there are 144 varactor diodes in total, with 72 placed vertically and 72 horizontally, with the antennas being vertically polarized, we have effectively $N_I = 72$.

From the measurement results shown in Fig. 20 and Fig. 43, we observe that, first, the spirals are offset from the origin and second, the spirals display only a small magnitude.

With Nossek's model, the offset can approximately be described by the identity matrix $\mathbf{I}_{N_I}$. The reflection coefficients resulting from the individual RIS settings k are then contained within the matrix $\mathbf{\Theta}$.

On the other hand, when using Shen's model, the offset would either have to be contained within $\mathbf{\Theta}$ or the direct path matrix $\mathbf{S}_{RT}$ and the reflection coefficients would also be described by $\mathbf{\Theta}$. However, the measurement results do not display any mutual coupling between the transmit and receive antennas, as can be seen from Fig. 25. Therefore, $\mathbf{S}_{RT}$ must be approximately zero, according to Shen's model.

As Shen's model does not directly account for the measured offset, Nossek's model is more convincing. However, neither of the two models considers a practical scenario. In both, the assumption is made that the antennas are isotropic and that the antennas and the RIS are minimum scattering antennas. The assumption of isotropic antennas can be approximately compensated by the inclusion of the antenna gains and radiation patterns to the scattering matrices. With the minimum scattering assumption, we theorize that an antenna or antenna array exhibits the same characteristics as a canonical minimum scattering antenna [33], [34], i.e., the antenna becomes invisible, it does not scatter electromagnetic fields, when its port is open-circuited. However, as many RISs are realized as planar antenna arrays, the minimum scattering assumption does not apply. Incident electromagnetic waves would induce surface currents, which in turn would cause the antenna to radiate and therefore scatter the electromagnetic field. In conclusion, while Nossek's model describes the measured offset and should probably be used over Shen's model, the restriction to minimum scattering antennas of both models is problematic, as RIS are commonly implemented as planar designs.

4 Conclusion

To summarize, in this thesis a RIS was measured in two campaigns, and an additional measurement run was performed with a reference reflector. The parameters defining these measurements are listed in Table 2. The data that was acquired from these campaigns has subsequently been processed and analyzed according to the channel model described in Section 3.2. Initially, the focus was exclusively on measurement positions in the farfield in Section 3.2.1, Section 3.2.2 and Section 3.2.3, but later, in Section 3.3, the effects of the nearfield positions in addition to the farfield positions were also investigated. Finally, some indicating parameters were proposed to describe the behavior of the RIS according to the results that had been presented thus far.

In Section 3.2 it was shown that the RIS measurement could be separated into the static and dynamic reflection components γ_S and $\gamma_D^{(k)}$, where only $\gamma_D^{(k)}$ was dependent on the RIS setting k (the bias voltage pattern applied to the RIS elements). It was shown that the dynamic component could be extracted from the measurements, displaying the behavior of the RIS, i.e., the complex reflection coefficients in relation to the bias voltages applied to the varactor diodes. However, we also saw that there were some interesting remaining components that were not defined by the channel model. In the case of the dynamic component, the influence from the scattering was small, pictured in Fig. 20, Fig. 21 and Fig. 22. The specific value of the static component, on the other hand, remains to be determined. Using the processing scheme of Section 3.2, we could reduce the influence of other effects, allowing us to obtain an estimate of the static reflection coefficient. The results analyzing this γ_S, nonetheless, have shown that there still exist some parasitic effects from the RIS that were not included in this channel model. They are assumed to result from the mutual coupling between the RIS elements, and potentially also of a weak coupling between the RIS itself and the absorbers and mounting structure behind it.

After this exploration of the measured channel at farfield positions, the data from nearfield positions was included with those from farfield positions in Section 3.3 to investigate the effects of a mixed campaign. From the analysis in that section, we saw that there was an increased position dependency. Additionally, in relation to the scattering environment for the farfield, we saw that in the nearfield there were dependencies between extracted parameters. Fig. 33 in particular highlighted a strong relation between the variance of clusters and their mean powers. These results showed, that while measuring in the nearfield is unlikely to provide data supporting the characterization of a RIS, these measurements can give a rough estimate of the phase shifts and magnitudes the RIS reflection coefficient may exhibit.

Finally, some performance indicators were presented in Section 3.4. The focus for this performance description was mainly on the magnitudes and the spread of the individual phase shifts. Additionally, the offset of the phase shifts from the origin was characterized by its mean, $\overline{\gamma}$, as opposed to the static reflection component γ_S introduced in Section 3.2. However, while the mean was useful in the determining frequency points of the reflection coefficients with small offsets from the origin, for a more practical example presented with Fig. 43, a different operating point had to be chosen. This shows that each of these indicators has their purpose, but one must remain aware of their limitations as well. The behavior of the RIS was then compared to some prominent channel models in Section 3.4.1. Here we saw that the assumptions made for these models (isotropic radiation, minimum scattering antennas) lead to useful models, but may lack factors to compensate

for the difference to realizations of RIS designs. Mainly the variation in magnitude of the reflection coefficients and the difference between phase shifts and their relations to the static offset should be considered. Examining the channel model proposed in [22], we can recognize another avenue for further research, namely, the potential relation between the static component γ_S and the specular reflection from the RIS. This indicates that for planar RIS designs, the minimum scattering assumption may need to be reconsidered.

Ultimately, in this work it was shown that it is possible to separate individual contributions of the measured channel and subsequently find a representation for the reflection coefficient of the RIS. The magnitudes of the reflection coefficients of the investigated RIS design are very small, showing that this RIS may not have been properly optimized. Simultaneously, this result opens up the question as to where the power that is not reflected or consumed by material losses has gone. It was also shown that measurements in the nearfield may be used to obtain a rough estimate of the behavior of the RIS, but coupling effects prevent the characterization of the performance of the RIS at such positions. Finally, the data acquired in this manner can be used to determine a set of parameters to support beam-focusing algorithms, and compare the performance of a realized RIS design with channel models.

5 References

[1] A. Gupta and R. K. Jha, "A Survey of 5G Network: Architecture and Emerging Technologies," *IEEE Access*, vol. 3, pp. 1206–1232, 2015. DOI: 10.1109/ACCESS.2015.2461602.

[2] X. Lin, J. Li, R. Baldemair, *et al.*, "5G New Radio: Unveiling the Essentials of the Next Generation Wireless Access Technology," *IEEE Communications Standards Magazine*, vol. 3, no. 3, pp. 30–37, 2019. DOI: 10.1109/MCOMSTD.001.1800036.

[3] C.-L. I, S. Han, and S. Bian, "Energy-efficient 5G for a greener future," en, *Nature Electronics*, vol. 3, no. 4, pp. 182–184, Apr. 2020, ISSN: 2520-1131. DOI: 10.1038/s41928-020-0404-1. [Online]. Available: https://www.nature.com/articles/s41928-020-0404-1 (visited on 04/11/2024).

[4] L. Williams, B. K. Sovacool, and T. J. Foxon, "The energy use implications of 5G: Reviewing whole network operational energy, embodied energy, and indirect effects," *Renewable and Sustainable Energy Reviews*, vol. 157, p. 112 033, 2022, ISSN: 1364-0321. DOI: https://doi.org/10.1016/j.rser.2021.112033. [Online]. Available: https://www.sciencedirect.com/science/article/pii/S1364032121012958.

[5] R. Kumar, S. K. Gupta, H.-C. Wang, C. S. Kumari, and S. S. V. P. Korlam, "From Efficiency to Sustainability: Exploring the Potential of 6G for a Greener Future," *Sustainability*, vol. 15, no. 23, 2023, ISSN: 2071-1050. DOI: 10.3390/su152316387. [Online]. Available: https://www.mdpi.com/2071-1050/15/23/16387.

[6] T. Huang, W. Yang, J. Wu, J. Ma, X. Zhang, and D. Zhang, "A Survey on Green 6G Network: Architecture and Technologies," *IEEE Access*, vol. 7, pp. 175 758–175 768, 2019. DOI: 10.1109/ACCESS.2019.2957648.

[7] P. Kaur and R. Garg, "Improving Energy Efficiency of 5G Base Stations: A Comprehensive AI-Based Optimization Approach," in *Proceedings of the NIELIT's International Conference on Communication, Electronics and Digital Technology*, S. N. Singh, S. Mahanta, and Y. J. Singh, Eds., Singapore: Springer Nature Singapore, 2023, pp. 463–478, ISBN: 978-981-99-1699-3.

[8] H. Q. Ngo, A. Ashikhmin, H. Yang, E. G. Larsson, and T. L. Marzetta, "Cell-Free Massive MIMO Versus Small Cells," *IEEE Transactions on Wireless Communications*, vol. 16, no. 3, pp. 1834–1850, 2017. DOI: 10.1109/TWC.2017.2655515.

[9] Ö. T. Demir, M. Masoudi, E. Björnson, and C. Cavdar, "Cell-Free Massive MIMO in O-RAN: Energy-Aware Joint Orchestration of Cloud, Fronthaul, and Radio Resources," *IEEE Journal on Selected Areas in Communications*, vol. 42, no. 2, pp. 356–372, 2024. DOI: 10.1109/JSAC.2023.3336187.

[10] A. L. Imoize, H. I. Obakhena, F. I. Anyasi, and S. N. Sur, "A Review of Energy Efficiency and Power Control Schemes in Ultra-Dense Cell-Free Massive MIMO Systems for Sustainable 6G Wireless Communication," *Sustainability*, vol. 14, no. 17, 2022, ISSN: 2071-1050. DOI: 10.3390/su141711100. [Online]. Available: https://www.mdpi.com/2071-1050/14/17/11100.

[11] C. Pan, H. Ren, K. Wang, *et al.*, "Reconfigurable Intelligent Surfaces for 6G Systems: Principles, Applications, and Research Directions," *IEEE Communications Magazine*, vol. 59, no. 6, pp. 14–20, 2021. DOI: 10.1109/MCOM.001.2001076.

[12] H. Radpour, M. Hofer, L. W. Mayer, A. Hofmann, M. Schiefer, and T. Zemen, "Active Reconfigurable Intelligent Surface for the Millimeter-Wave Frequency Band: Design and Measurement Results," 2023. DOI: 10.48550/ARXIV.2306.04515. [Online]. Available: https://arxiv.org/abs/2306.04515 (visited on 04/11/2024).

[13] G. C. Trichopoulos, P. Theofanopoulos, B. Kashyap, *et al.*, "Design and Evaluation of Reconfigurable Intelligent Surfaces in Real-World Environment," *IEEE Open Journal of the Communications Society*, vol. 3, pp. 462–474, 2022. DOI: 10.1109/OJCOMS.2022.3158310.

[14] S. Zhao, R. Langwieser, and C. F. Mecklenbraeuker, "Reconfigurable digital metasurface for 3-bit phase encoding," in *WSA 2021; 25th International ITG Workshop on Smart Antennas*, 2021, pp. 1–6.

[15] X. Pei, H. Yin, L. Tan, *et al.*, "RIS-Aided Wireless Communications: Prototyping, Adaptive Beamforming, and Indoor/Outdoor Field Trials," *IEEE Transactions on Communications*, vol. 69, no. 12, pp. 8627–8640, 2021. DOI: 10.1109/TCOMM.2021.3116151.

[16] J. Li, "From Liquid Crystal on Silicon and Liquid Crystal Reflectarray to Reconfigurable Intelligent Surfaces for Post-5G Networks," *Applied Sciences*, vol. 13, no. 13, 2023, ISSN: 2076-3417. DOI: 10.3390/app13137407. [Online]. Available: https://www.mdpi.com/2076-3417/13/13/7407.

[17] S. Zeng, H. Zhang, B. Di, *et al.*, "Reconfigurable Intelligent Surfaces in 6G: Reflective, Transmissive, or Both?" *IEEE Communications Letters*, vol. 25, no. 6, pp. 2063–2067, 2021. DOI: 10.1109/LCOMM.2021.3062615.

[18] H. Ma, H. Zhang, W. Zhang, and V. C. M. Leung, "Beamforming Optimization for Reconfigurable Intelligent Surface With Power Splitting Aided Broadcasting Networks," *IEEE Transactions on Vehicular Technology*, vol. 72, no. 2, pp. 2712–2717, 2023. DOI: 10.1109/TVT.2022.3214529.

[19] Y. Zou, Y. Long, S. Gong, *et al.*, "Robust Beamforming Optimization for Self-Sustainable Intelligent Reflecting Surface Assisted Wireless Networks," *IEEE Transactions on Cognitive Communications and Networking*, vol. 8, no. 2, pp. 856–870, 2022. DOI: 10.1109/TCCN.2021.3133839.

[20] Q. Li, M. Wen, E. Basar, G. C. Alexandropoulos, K. J. Kim, and H. V. Poor, "Channel Estimation and Multipath Diversity Reception for RIS-Empowered Broadband Wireless Systems Based on Cyclic-Prefixed Single-Carrier Transmission," *IEEE Transactions on Wireless Communications*, vol. 22, no. 8, pp. 5145–5156, 2023. DOI: 10.1109/TWC.2022.3232072.

[21] S. Shen, B. Clerckx, and R. Murch, "Modeling and Architecture Design of Reconfigurable Intelligent Surfaces Using Scattering Parameter Network Analysis," *IEEE Transactions on Wireless Communications*, vol. 21, no. 2, pp. 1229–1243, 2022. DOI: 10.1109/TWC.2021.3103256.

[22] J. A. Nossek, D. Semmler, M. Joham, and W. Utschick, *Physically Consistent Modelling of Wireless Links with Reconfigurable Intelligent Surfaces Using Multiport Network Analysis*, 2023. arXiv: 2308.12223 [eess.SP].

[23] D. M. Pozar, *Microwave Engineering: Theory and Techniques*. John wiley & sons, 2021.

[24] B. R. GmbH. "Aluminiumprofile – Lösungen & Komponenten." (2023), [Online]. Available: https://web.archive.org/web/20231205180800/https://www.boschrexroth.com/de/at/produkte/produktgruppen/montagetechnik/themen/aluminiumprofile-loesungen-komponenten/ (visited on 04/11/2024).

[25] F. Kiss, R. Langwieser, R. Prüller, H. Groll, S. Zhao, and M. Rupp, "Measurement Environment for RIS Enhanced Wireless Channels," in *2023 IEEE 24th International Workshop on Signal Processing Advances in Wireless Communications (SPAWC)*, 2023, pp. 381–385. DOI: 10.1109/SPAWC53906.2023.10304485.

[26] C. R. Harris, K. J. Millman, S. J. van der Walt, *et al.*, "Array programming with NumPy," *Nature*, vol. 585, no. 7825, pp. 357–362, Sep. 2020. DOI: 10.1038/s41586-020-2649-2. [Online]. Available: https://doi.org/10.1038/s41586-020-2649-2.

[27] T. M. Inc., *MATLAB Version: 24.1.0.2537033 (R2024a)*, Natick, Massachusetts, United States, 2024. [Online]. Available: https://www.mathworks.com.

[28] A. F. Molisch, *Wireless Communications*. John Wiley & Sons, 2012, vol. 34.

[29] Y. Hu, "A method of determining phase centers and its application to electromagnetic horns," *Journal of the Franklin Institute*, vol. 271, no. 1, pp. 31–39, 1961, ISSN: 0016-0032. DOI: https://doi.org/10.1016/S0016-0032(61)91013-4.

[30] E. Muehldorf, "The phase center of horn antennas," *IEEE Transactions on Antennas and Propagation*, vol. 18, no. 6, pp. 753–760, 1970. DOI: 10.1109/TAP.1970.1139799.

[31] F. J. Massey, "The Kolmogorov-Smirnov Test for Goodness of Fit," *Journal of the American Statistical Association*, vol. 46, no. 253, pp. 68–78, 1951, ISSN: 01621459. [Online]. Available: http://www.jstor.org/stable/2280095 (visited on 04/11/2024).

[32] P. Virtanen, R. Gommers, T. E. Oliphant, *et al.*, "SciPy 1.0: Fundamental Algorithms for Scientific Computing in Python," *Nature Methods*, vol. 17, pp. 261–272, 2020. DOI: 10.1038/s41592-019-0686-2.

[33] W. Kahn and H. Kurss, "Minimum-scattering antennas," *IEEE Transactions on Antennas and Propagation*, vol. 13, no. 5, pp. 671–675, 1965. DOI: 10.1109/TAP.1965.1138529.

[34] P. Rogers, "Application of the minimum scattering antenna theory to mismatched antennas," *IEEE Transactions on Antennas and Propagation*, vol. 34, no. 10, pp. 1223–1228, 1986. DOI: 10.1109/TAP.1986.1143747.